COSMOLOGICAL N-BODY SIMULATIONS OF COLD DARK MATTER HALOS

Dissertation

zur

Erlangung der naturwissenschaftlichen Doktorwürde
(Dr. sc. nat.)

vorgelegt der

Mathematisch-naturwissenschaftlichen Fakultät

der

Universität Zürich

von

Jürg Diemand

von

Uster ZH

Promotionskomitee

Prof. Dr. Ben Moore (Vorsitz)
Prof. Dr. Daniel Wyler
Dr. Joachim Stadel

Zürich, 2004

Für Zintia und meine Eltern

Contents

List of Figures

List of Tables

Zusammenfassung

Diese Arbeit untersucht die Verteilung der kalten dunklen Materie (CDM) im Universum mit kosmologischen Simulationen.

Nicht-baryonische dunkle Materie ist die dominante Komponente in der Entstehung von Strukturen in Kosmos, weil sie viel häufiger ist als gewöhnliche (baryonische) Materie, und weil mehr Zeit vorhanden ist, um in ihr Strukturen zu formen, da dunkle Materie früher vom heissen kosmischen Plasma entkoppelt. Kosmologische N-Körper Simulationen können die nicht lineare Evolution der Verteilung der dunklen Materie in einem gegebenen kosmologischen Modell verfolgen. Das Standardmodell der Kosmologie und seine wichtigsten Bestätigungen durch Beobachtungen werden im Kapitel 1 zusammengefasst.

In kosmologischen N-Körper Simulationen verwendet man eine grosse Zahl ("N") von super-massiven Teilchen, welche Elemente des Fluids aus dunkler Materie repräsentieren. Typische Simulationen verwenden heute (2004) zwischen etwa zehn Millionen und ein paar Milliarden Teilchen. Aber diese Superteilchen sind immernoch viele Grössenordnungen schwerer als die CDM Teilchen, für welche eine Masse von ungefähr 100 GeV erwartet wird. Die Superteilchen erleiden Zusammenstöesse während einer Simulation, was ihre Bahnen und Energien abändert. Auf kleinen Skalen (d. h. unter einer "softening length") benutzt man eine schwächere Kraft als diejenige, welche Newtons Gravitationsgesetz ergibt, um diese Effekte zu minimieren (und auch um Rechenzeit zu sparen). Aber dieses Softening kann die Effekte nicht ganz eliminieren, weil sie zum grossen Teil durch weniger starke, aber viel häufigere Begegnungen mit relativ grossen Abständen verursacht werden. N-Körper Simulationen der hierarchischen Strukturbildung leiden immer unter dem Problem, dass die ersten aufgelösten Halos nur wenige Teilchen enthalten. Obwohl Kollisionen in virialisierten Objekten mit mehreren Millionen Teilchen kein Problem mehr sind, dominieren sie immer in den ersten Strukturen. Im Kapitel 2 bestimmen wir ihren Einfluss in kosmologischen Simulationen. Wir zeigen, dass mit besserer Auflösung (grösseres N) der Einfluss von Kollisionen nur langsam zurückgeht, nur mit $N^{-0.25}$. Wir zeigen auch, dass diese Kollisionen die Dichteprofile der Halos im inneren Teil abflachen.

In den Kapiteln 3 und 4 bestimmen wir die Dichteprofile der dunklen Materie in Galaxienhaufen und Galaxien mit kosmologischen Simulationen, welche die momentan höchsten Auflösungen erreichen. Indem dasselbe System mit verschiedener Auflösung simuliert wird, können wir bestimmen, in welchen Regionen die Resultate robust sind und welche Regionen vom numerischen Verflachen der Profile betroffen sind. Wir zeigen, dass der kleinste noch gut aufgelöste nur Radius langsam kleiner wird, wenn die Anzahl Teilchen erhöht wird, wie erwartet aus Kapitel 2. Dieser Radius ist proportional zu $r \propto N^{-1/3}$. Im ganzen, gut aufgelösten Bereich kann man die Profile mit einem verallgemeinerten NFW Profil beschreiben, welches in gegen der Mitte gegen $\rho \propto r^{-\gamma}$ geht, d. h. einen so genannten "Cusp" hat. Wir finden aus den Profilen der sechs simulierten Galaxienhaufen, dass $\gamma = 1.16 \pm 0.14$ (siehe Kapitel 3). Aber in diesen Profilen und in Resultaten von anderen Forschungsgruppen sieht man keine klare, innere Region, wo die logarithmische

Steigung den konstanten Wert $-\gamma$ tatsächlich annimmt. Die Steigungen gehen zur Mitte hin scheinbar kontinuierlich gegen Null. Deswegen haben Stoehr et. al (2002) und Navarro et al. (2004) neue Profile mit einem Kern konstanter Dichte, anstelle eines Cusps, vorgeschlagen. Das würde die Vorhersagen der CDM Theorie für viele Messungen radikal verändern: Zum Beispiel die vorhergesagten Rotationskurven von LSB Galaxien wären viel flacher nahe des Zentrums (und damit näher an den beobachteten Werten (Stoehr, 2004)). Auch die Gamma-Strahlung aus der Annihilation von SUSY-CDM Teilchen in Zentrum der Milchstrasse wäre einige Grössenordnungen schwächer und unterhalb der Empfindlichkeit von heutigen Experimenten wie AMANDA, AMS, GLAST oder MAGIC (Eidelman et al., 2004).

Durch Simulationen mit viel grösserer Auflösung kann man zwischen inneren Dichteprofilen mit Cusp und solchen mit einem Kern konstanter Dichte unterscheiden. Deswegen simulieren wir im Kapitel 4 einen durchschnittlichen Galaxienhaufen aus unserem Sample nochmals. Diesesmal erreichen wir eine zehn mal bessere Auflösung, indem wir eine neue Methode zur Verfeinerung der Anfangsbedingungen anwenden. Jetzt lösen wir zum ersten Mal eine Region sehr nahe des Zentrums auf, und dort ist die logarithmische Steigung ungefähr konstant. Das heisst wir haben einen deutlichen Hinweis gefunden, dass Halos aus dunkler Materie einen Cusp haben und keinen Kern konstanter Dichte. Das erhöht die Chancen von heutigen und zukünftigen Experimenten, welche nach der Gamma-Strahlung aus der Annihilation von SUSY-CDM Teilchen suchen. Die Halos in früheren CDM Simulationen hatten keine inneren Strukturen. Aber mit der Zunahme der numerischen Auflösung entdeckte man, dass CDM Halos eine grosse Anzahl gebundener Subhalos enthalten, welche sich innerhalb des Halos um dessen Zentrum bewegen und etwa zehn bis zwanzig Prozent der totalen Masse der Halos ausmachen. Im Kapitel 5 analysieren wir die heutige Verteilung der Substrukturen in den selbe sechs hochauflösenden Simulationen von Galaxienhaufen aus Kapitel 3 und auch in vier Galaxienhalos. Mit mehr als tausend Subhalos pro Halo können wir ihre räumliche Verteilung und ihre Geschwindigkeitsverteilung genau messen und mit Beobachtungsdaten vergleichen. Die Eigenschaften der Substruktur in Halos von Galaxien und Halos von Galaxienhaufen sind sehr ähnlich. Die Geschwindigkeitsverteilung weicht von der Maxwell-Verteilung ab, sie hat eine negative Kurtosis von etwa -0.7, das heisst langsame Subhalos sind relativ selten. Innerhalb des Virialradius gibt einen klaren Unterschied zwischen den durchschnittlichen Geschwindigkeiten von Subhalos und von den übrigen Teilchen: $b = \sigma_{\mathrm{sub}}/\sigma_{\mathrm{DM}} \sim 1.12 \pm 0.04$, und der Unterschied wächst auf $b > 1.3$ im Inneren der Halos. Langsame Subhalos sind seltener, weil sie schon früh in der Entstehungsphase des Galaxienhaufens von Gezeitenkräften zerrissen werden. Das führt auch zu einer unterschiedlichen räumlichen Verteilung, das radiale Profil der Subhalos ist deutlich flacher als dasjenige der gesamten Halomasse. Beobachtungen von Galaxienhaufen zeigen keine solchen Unterschiede, wir interpretieren sie als eine Beschränkung von Simulationen die nur die dunkle Materie einbeziehen. Wir schätzen, dass etwa die Hälfte der Subhalos in solchen Simulationen fehlt, weil sie durch physikalisches “overmerging” zerstört wurden. Hochauflösende, hyrdodynamische Simulationen sind nötig, um diese Frage weiter zu untersuchen. Wenn das CDM Modell korrekt ist, dann müssen Galaxien in Clusters die Gezeitenkräfte überleben, vielleicht wegen der Ansammlung von Gas in Zentrum während der Entstehung von elliptischen Galaxien. Spiralgalaxien können nicht in der Nähe der Zentrums existieren, und die elliptischen Galaxien in diesem Bereich werden wenig verbleibende dunkle Materie besitzen. Das bedeutet auch, dass der Zusammenhang zwischen Morphologie und Dichte der Umgebung *vor* der Entstehung des Clusters gesetzt wird, und nicht erst später als Folge von Transformationen von Spiralgalaxien in S0-Galaxien durch Wechselwirkungen mit der Umgebung im Cluster.

Im Kapitel 6 analysieren wir den Bahnverlauf von Subhalos. Die Hälfte der Halos, welche heute einen Abstand von ein bis zwei Virialradien vom Cluster haben, waren früher einmal innerhalb des Clusters. Die meisten von ihnen gingen sogar durch die innere Hälfte der Clusters. Sogar einige Halos, welche heute einen Abstand von bis zu drei Virialradien vom Cluster haben, flogen früher durch das Cluster. Das könnte erklären, wieso ein Teil der Spiralgalaxien in der Umgebung des Virgo Clusters sehr wenig neutralen Wasserstoff enthalten (Sanchis, Lokas & Mamon, 2004) und wieso das "intracluster" (d. h. nicht von den Cluster Galaxien stammende) Licht von Virgo bis zu vergleichbaren Distanzen gleichmässig verteilt ist (Feldmeier et al., 2004). Wir finden keine signifikante Korrelation zwischen der Zeit, welche ein Subhalo im Cluster verbracht hat, und dem heutigen Abstand vom Zentrum. Dieser Zusammenhang könnte signifikant sein, wenn wir auch die zentralen Galaxies auflösen könnten, welche wir durch das physikalische "overmerging" verloren haben. Unser Resultat gilt nur für Subhalos und schliesst einen solchen Zusammenhang für *Galaxien in Clusters* nicht aus.

Die Teilchen, aus welchen die kalte dunkle Materie besteht, sind bisher unbekannte Teilchen ausserhalb des Standardmodells der Teilchenphysik. Die wahrscheinlichsten Kandidaten sind Axionen und Teilchen aus supersymmetrischen Theorien (SUSY). Im Kapitel 7 präsentieren wir Simulationen zur Entstehung der ersten, kleinsten Halos, welche im SUSY-CDM Modell entstehen. Die Mikrophysik dieser schwach wechselwirkenden, massiven Teilchen (weakly interacting massive particles, "WIMPs") führt zu einem abrupten Abfallen der typischen Amplituden der Dichtefluktuationen unterhalb Skalen von etwa $10^{-6}\mathrm{M}_\odot$ (für ein 100 GeV Teilchen) (Green et al., 2004). Wir zeigen, dass die Abundanz dieser Halos in einem Bereich liegt, den man erhält, indem man die bekannte Abundanz der Galaxienhalos, unter der Annahme $n(>m) \propto m^{-1}$, bis nach $m = 10^{-6}\mathrm{M}_\odot$ extrapoliert. Die inneren Eigenschaften dieser ersten Strukturen sind noch nicht sehr gut aufgelöst ($N_{\mathrm{virial}} \simeq 1000$), aber im aufgelösten Bereich ähneln die Dichteprofile denjenigen von (reskalierten) Galaxien oder Galaxienhaufen. Die grosse mittlere Dichte dieser Minihalos kann ihr Überleben als Subhalos im Halo der Milchstrasse ermöglichen. In diesem Fall wäre die lokale Anzahldichte diese Minihalos enorm gross, und die nächsten von ihnen könnten im Gammastrahlen-Signal aus der Annihilation von SUSY-CDM Teilchen beobachted werden.

Summary

This thesis studies the distribution of dark matter in the universe with cosmological N-body simulations.

Non-baryonic dark matter is the dominant component in the formation of cosmic structures, because it is much more abundant than baryonic matter and because there is more time to grow structures with it, since dark matter decouples earlier from hot cosmic plasma which suppresses structure formation. Cosmological N-body simulations are able to follow the non-linear evolution of the dark matter distribution in a given cosmological model. The standard model of cosmology and its observational support is introduced in Chapter 1.

In cosmological N-body simulations one uses a large number ("N") of super-massive particles to represent dark matter fluid elements, typical state-of-the-art (in the year 2004) simulations use N of the order ten millions to a few billions. But these super-particles are still many orders of magnitude heavier than the real dark matter particles, which are expected to have a mass of the order of 100 GeV. These super-particles undergo encounters during the simulations that lead to changes in their orbits and energies. One uses a softer gravitational force than the one from Newton's law on short scales (i. e. below a so called softening length) to reduce these discreteness effects (and also to reduce the computation time). However this softening cannot eliminate discreteness effects ("numerical relaxation") entirely since they are caused to a large amount by the less violent but much more numerous encounters with relatively large separations. N-body simulations of the hierarchical formation of cosmic structures suffer from the problem that the first objects to form always contain just a few particles. Although relaxation is not an issue for virialised objects containing millions of particles, collisional processes will always dominate within the first structures that collapse. In Chapter 2 we quantify the relaxation within isolated haloes and in cosmological simulations. We explore the effect of resolution on the degree of relaxation and we find that increasing N slowly reduces the degree of relaxation in CDM simulations $\propto N^{-0.25}$ rather than proportional to N as expected from the collisionless Boltzmann equation. We also show that relaxation tends to flatten the density profiles of dark matter halos in the inner part.

In Chapters 3 and 4 we determine the dark matter density profiles of galaxy clusters with the currently highest resolution cosmological simulations. By resolving the same system at various mass resolutions one can find which regions have converged to a robust result and which regions are affected by numerical flattening of the profiles. We find that the resolved scale slowly becomes smaller when the number of particles is increased, as expected from Chapter 2. The scaling goes as $r \propto N^{-1/3}$. Over the entire resolved regions the density profiles are well fitted by a generalized NFW profile which asymptotes to a central cusp [1] $\rho \propto r^{-\gamma}$, where we find $\gamma = 1.16 \pm 0.14$ from the mean of the fits to our six

---

[1] In a cusp the density grows towards infinity as one approaches the halo center, in reality there will of

highest resolution clusters (see Chapter 3). The NFW profile is a two power law function, it curves form $\rho \propto r^{-3}$ in the outer part to an inner cusp of $\rho \propto r^{-1}$. Moore et. al 1998 have proposed a similar fitting function with a steeper cusp in the inner part: $\rho \propto r^{-1.5}$. However in the profiles presented in Chapter 3 and simulations by other groups at similar resolution there was no evidence for a constant inner logarithmic slope, the profiles seem the become gradually shallow over to entire resoved range. This lead Stoehr et. al (2002) and Navarro et al. (2004) to propose new fitting functions that have a constant density core in the center instead of a cusp. This would radically change the predictions of the CDM theory for various measurements: For example the predicted galaxy rotations curves would be much shallower near the center (and closer to the observations from LSB galaxies (Stoehr, 2004)) and the gamma-ray signal from anihilations of SUSY-CDM particles in the galactic center would be orders of magnitudes smaller and much below the sensitivity of ongoing indirect dark matter searches, like AMANDA, AMS, GLAST, MAGIC (Eidelman et al., 2004).

With much higher resolution simulations one can distinguish between inner density profiles that asymptote to a core or a cups. Therefore in Chapter 4 we resimulate an average cluster of this sample at ten times better mass resolution in the inner part by using a new way of refining the cosmological initial conditions. At this resolution we indeed resolve for the first time the part near the center of a halo where its logarithmic slope is constant, this means that we found strong evidence against the proposed cored profiles and show that dark matter density profiles asymptote to a cusp. The confirmation of cuspy inner profiles greatly enhances the possibility to indirectly detect dark matter in the galactic center with present and future experiments. The first dark matter halos in simulation where rather smooth, but with the increase of resolution one discovered that CDM halos are not smooth at all, ten to twenty percent of their mass are bound to a large number of small sub-clumps that orbit within the main halo. In Chapter 5 we analyze the present day distribution of substructure in the same six high resolution cluster studied in Chapter 3 and also in four galaxy size halos. With thousands of subhalos per object we can accurately measure their spatial clustering and velocity distribution functions and compare these with observational data. The substructure properties of galactic halos closely resembles those of galaxy clusters with a small scatter in the mass and circular velocity functions. The velocity distribution function is non-Maxwellian and flat topped with a negative kurtosis of about -0.7. Within the virial radius there is a clear velocity bias $b = \sigma_{\mathrm{sub}}/\sigma_{\mathrm{DM}} \sim 1.12 \pm 0.04$, increasing to $b > 1.3$ within the halo centers. Slow subhalos are much less common, due to physical disruption by gravitational tides early in the merging history. This leads to a spatially anti-biased subhalo distribution that is well fitted by a cored isothermal. Observations of cluster galaxies do not show such biases which we interpret as a limitation of pure dark matter simulations - we estimate that we are missing half of the halo population which has been destroyed by physical overmerging. High resolution hydrodynamical simulations are required to study these issues further. If CDM is correct then the cluster galaxies must survive the tidal field, perhaps due to baryonic inflow during elliptical galaxy formation. Spirals can never exist near the cluster centers and the elliptical galaxies there will have little remaining dark matter. This implies that the morphology-density relation is set *before* the cluster forms, rather than a subsequent transformation of disks to S0's by virtue of the cluster environment.

---

course be some maximum density (which is much higher than the ones we can resolve in current cosmological simulations) set by the microphysics of the dark matter particle through collisions and anihilations.

In Chapter 6 we analyze the orbital history of subhalos and find that half of the halos at distances of one to two virial radii today have previously orbited through the cluster, most of them have even passed through the inner half of the cluster. Some halos at distances of up to three times the virial radius have also passed trough the cluster core earlier. This could explain why some spiral galaxies in the outskirts of the Virgo cluster are observed to be deficient in neutral Hydrogen (Sanchis, Lokas & Mamon, 2004) and why Virgo's intracluster light extends to similar distances (Feldmeier et al., 2004). We do not find a significant correlation of "infall age" versus present day position for *substructures* and the scatter at a given position is very large. This relation may be significant if we could resolve the physically overmerged galaxies in the central region and our result does not exclude a significant correlation for *cluster galaxies*.

The particle(s) which make up CDM are yet unknown particles beyond the standard model of particles physics, the favored candidates are axions or supersymmmetric particles (SUSY). In Chapter 7 we present simulations of the formation of the first, smallest dark matter halos that form in a SUSY-CDM model. The micro-physics of the weakly interacting massive particles (WIMPs) leads to a sharp cut-off in the power spectrum, which depends on the WIMP mass and other SUSY parameters and lies at about $10^{-6}\mathrm{M}_{\odot}$ for a 100 GeV particle (Green et al., 2004). We find that the abundance of these minihalos lies in a range obtained by extrapolation of the well known mass function on galactic scales with a steep slope of $\alpha = -1$ down to $10^{-6}\mathrm{M}_{\odot}$. The internal properties of the minihalos are not well resolved yet ($N_{\mathrm{virial}} \simeq 1000$) but in the resolved range they resemble rescaled versions of galactic halos. Their very high mean densities could enable them to survive as substructures in the Milky Way halo. In this case there would be a huge local number density of minihalos and the closest minihalos could be detected as point sources in the γ-ray signal from SUSY-CDM annihilations.

Chapter 1

Introduction

In this chapter we briefly introduce the standard cosmological model and its most important observational probes, and the role of dark matter and cosmological simulations. A detailed description of physical cosmology is given for example by Peacock (2003). An updated review of the cosmological model, its parameters and observational probes can be found in the 2004 Review of Particle Physics, Eidelman et al. (2004).

1.1 The standard model of cosmology

The expansion of the Universe was discovered by Hubble & Humason (1931) who noted that most galaxies move away from us and that their average radial velocities grow with distance. Now the expansion rate has been measured with much higher precision and out to very large distances by the "Hubble Space Telescope" (Freeman et al., 2001) and we have other independent evidence that we live in an expanding Universe which emerged from an extremely dense, hot phase (the "Big Bang") about 14 billion years ago.

For a general description, the Universe is usually taken to be a perturbed Robertson-Walker space-time with the dynamics governed by Einstein's theory of general relativity. The field equation is:

$$G_{\mu\nu} = 8\pi G T_{\mu\nu} + \Lambda g_{\mu\nu}, \tag{1.1}$$

where G is the gravitational constant, $T_{\mu\nu}$ the energy-momentum tensor, Λ the vacuum energy and $G_{\mu\nu}$ is the Einstein tensor. The metric $g_{\mu\nu}$ is related to the line element:

$$ds^2 = a^2 \left(\frac{dr^2}{1 - kr^2} + r^2 d\Omega^2 \right), \tag{1.2}$$

where $k = +1, 0, -1$ describes the curvature of space, corresponding to an closed, flat or open Universe, respectively, with spherical, flat or hyperbolic geometry.
The scale factor[1] a defines, for a given value of k, a one-parameter family of similar spaces. Its time dependence, leading to the Hubble constant[2] $H(t)$, is derived from (0-0)

---

[1] The redshift z is related to the scale factor: $1 + z \equiv \frac{a_0}{a}$, where a_0 denotes the present value of the scale factor.

[2] The present value of the Hubble parameter is usually written as $H(t_0) = 100\, h\, km\, s^{-1}\, Mpc^{-1}$.

component of the field equation (1.1), the Friedmann equation:

$$H(t) \equiv \left(\frac{\dot{a}}{a}\right)^2 = \frac{8\pi G}{3}\rho - \frac{k}{a^2} + \frac{\Lambda}{3}, \tag{1.3}$$

where ρ is the matter and radiation density of the universe. The Friedmann equation is usually rewritten by defining the critical density $\rho_c(t)$ corresponding to $k = \Lambda = 0$:

$$\rho_c(t) \equiv \frac{3H^2(t)}{8\pi G}, \tag{1.4}$$

and by defining the ratios of different matter components i (including vacuum energy and curvature) as ratios of the critical density:

$$\Omega_i \equiv \frac{\rho_i}{\rho_c}, \qquad \Omega_\Lambda \equiv \frac{\Lambda}{3H^2}, \qquad \Omega_k \equiv -\frac{k}{a^2H^2}. \tag{1.5}$$

The Friedmann equation can thus be written:

$$\sum_i \Omega_i + \Omega_\Lambda + \Omega_k = 1. \tag{1.6}$$

For a complete picture of the Universe we also need a description of deviations from homogeneities. Interestingly, studying the evolution of perturbations (from the early Universe) gives some of the most powerful probes of the parameters described above.
A generic (spatially localized) perturbation $f(\mathbf{x})$ is usually expanded in a Fourier integral:

$$f(\mathbf{x}) = \frac{1}{(2\pi)^{3/2}} \int f(\mathbf{k}) \exp(i\mathbf{k}\cdot\mathbf{x})\, d^3k, \tag{1.7}$$

with the corresponding power spectrum $\mathcal{P}$:

$$< f^*(\mathbf{k}) f(\mathbf{k}') >= \delta^3(\mathbf{k}-\mathbf{k}')\frac{2\pi^3}{k^3}\mathcal{P}(k), \tag{1.8}$$

where one usually assumes that the Universe is isotropic on average, i.e. $\mathbf{k} \equiv k$.
If the perturbations obey Gaussian statistics, the power spectrum gives a complete description of their properties. Very often one approximates the power spectrum by a power law:

$$\mathcal{P}(k) = \mathcal{P}(k_*) \left(\frac{k}{k_*}\right)^{n-1}, \tag{1.9}$$

where k_* is an arbitrarily chosen scale. Observations show that $n \approx 1$, which corresponds to scale invariant perturbations.
The simplest way to generate the observational data is the inflationary scenario, see e. g. Kolb & Turner 1990;Liddle & Lyth 2000. Inflation generates perturbations through the amplification of quantum fluctuations, which are stretched to observable astrophysical scales by a rapid exponential expansion. Several inflationary models have been invoked. The simplest ones generate two types of perturbations: Scalar field fluctuations which lead to density perturbations with a corresponding metric fluctuation and tensor metric fluctuations which can produce gravitational waves. Whereas the former will experience gravitational instabilities, leading to structure formation and observable objects, the later

would not contribute to structure formation but would also influence the Cosmic Microwave Background (CMB) anisotropies. For the CMB, the perturbations are still small and they can be calculated with a linear (numerical) model. On small scales and at later times, non-linear evolution becomes more important which can be followed by cosmological N-body simulations.

Of particular interest are CMB anisotropies. The CMB gives a fingerprint of the Universe at $z \sim 1000$ with a temperature $T \sim 3000\,K$. At this epoch there was a tight coupling between electrons and photons. Measuring CMB anisotropies directly reveals the surface of last scattering (taking into account the time evolution) where primary anisotropies are imprinted. At the time of free streaming (after decoupling), the electron and photon fluid were evolving separately. The photon fluid evolution is described by the Liouville equation, which shows how spatial variations on the last scattering surface map into angular variations on the observed sky today. In the evolution of the photon distribution function, the isotropic temperature perturbations are transferred to higher multipoles. As the gauge invariant temperature brightness perturbations are directly related to the fluctuations in the photon distribution function, precise temperature maps of the CMB will give exact information of the surface of last scattering.
The temperature perturbations, expanded in spherical harmonics, can be written:

$$\frac{T(\hat{n})}{T_0} = 1 + \sum_{\ell=1}^{\infty} \sum_{m=-\ell}^{\ell} a_{\ell m}^{T} Y_{\ell m}(\hat{n}), \tag{1.10}$$

with the temperature multipole coefficients:

$$a_{\ell m}^{T} = \frac{1}{T_0} \int d\hat{n} T(\hat{n}) Y_{\ell m}^{*}(\hat{n}). \tag{1.11}$$

The observed temperature angular power spectrum $\mathcal{C}_\ell$ is defined by:

$$< a_{lm}^{*T}, a_{\ell' m'}^{T} >= \mathcal{C}_\ell \delta_{\ell\ell'} \delta_{mm'}, \tag{1.12}$$

for which an unbiased estimator is:

$$\hat{\mathcal{C}}_\ell^{T} = \frac{1}{2l+1} \sum_{m=-\ell}^{\ell} a_{\ell m}^{*T} a_{\ell m}^{T}. \tag{1.13}$$

The so called cosmic variance is due to statistical uncertainties, since only one Universe can be observed. One usually assumes a statistical isotropy, i.e. $\ell = \ell', m = m'$, and therefore the temperature fluctuations mainly reveal density perturbations.

A final important parameter in a cosmological model is the optical depth for scattering of CMB photons τ, it is related to ionization state of the Universe.
The basic set of 10 cosmological parameters is therefore:

Hubble parameter	h
Cosmological constant	Ω_Λ
Dark matter density	Ω_{dm}
Baryon density	Ω_B

Radiation density	Ω_{rad}
Neutrino density	Ω_ν
Density perturbation amplitude	$\mathcal{P}(k_*)$
Density perturbation spectral index	n
Tensor to scalar ratio	r
Ionization optical depth	τ

Models based on these parameters are able to give a good fit to the complete set of data available at present. For an extension to the standard model and a list of the parameters measured by WMAP, see e.g. Spergel et al. (2003) and Eidelman et al. (2004).

1.2 Observational probes

In this section we will outline some of the main resent observational results to constrain the cosmological parameters introduced in the last section, see Eidelman et al. (2004) and references therein for more details.

Galaxy clustering:
The matter distribution is most easily probed by observing the galaxy distribution. The present day dark matter distribution on galaxy and cluster scales can be calculated with cosmological simulations for a given set of cosmological parameters (see Figure 1.6). However, galaxies are biased tracers of dark matter and comparisons to measurement of galaxy clustering are not trivial. Using some reasonable assumptions about how to populate dark matter halo with galaxies it is possible to match the observed galaxy clustering very well (e.g. Davis et al. 1985;Peacock 2003;Yang, Mo, & van den Bosch 2003; Berlind et al. 2003;Magliocchetti & Porciani 2003;van den Bosch et al. 2004;).
The two degree field (2dF) Galaxy Redshift Survey is now complete with more than 245,000 redshifts (Colless, 2003). The measured power spectrum is well fitted with a CDM (Cold Dark Matter) model with $\Omega_m = 0.3$ (Hawkins et al. 2003;(Peacock 2003). The present epoch power spectrum is not sensitive to dark energy, so it is mainly a probe of the matter density.
The ongoing Sloan Digital Sky Survey (SDSS, see www.sdss.org and e.g. Abazajian et al. 2003) will systematically map one-quarter of the entire sky and has already produced a wealth of publicly available data and similar power spectrum results as 2dF.

Clusters of galaxies:
The normalisation of the power spectrum $\mathcal{P}(k_*)$ is related to σ_8, which is the root mean square of the mean density in randomly placed spheres of 8h^{-1}Mpc at z=0. Clusters are usually used to constrain σ_8, as an 8h^{-1}Mpc sphere contains about the right amount of material to form a cluster. The most useful information comes from X-ray emission from the hot gas which can be used to constrain the total cluster mass. Recent data give:

$$\sigma_8 = 0.78^{+0.30}_{-0.06}, \tag{1.14}$$

for $\Omega_m = 0.35$. Scaling to lower Ω_m increases σ_8.
If clusters are representative of the mass distribution in the Universe, the fraction of the

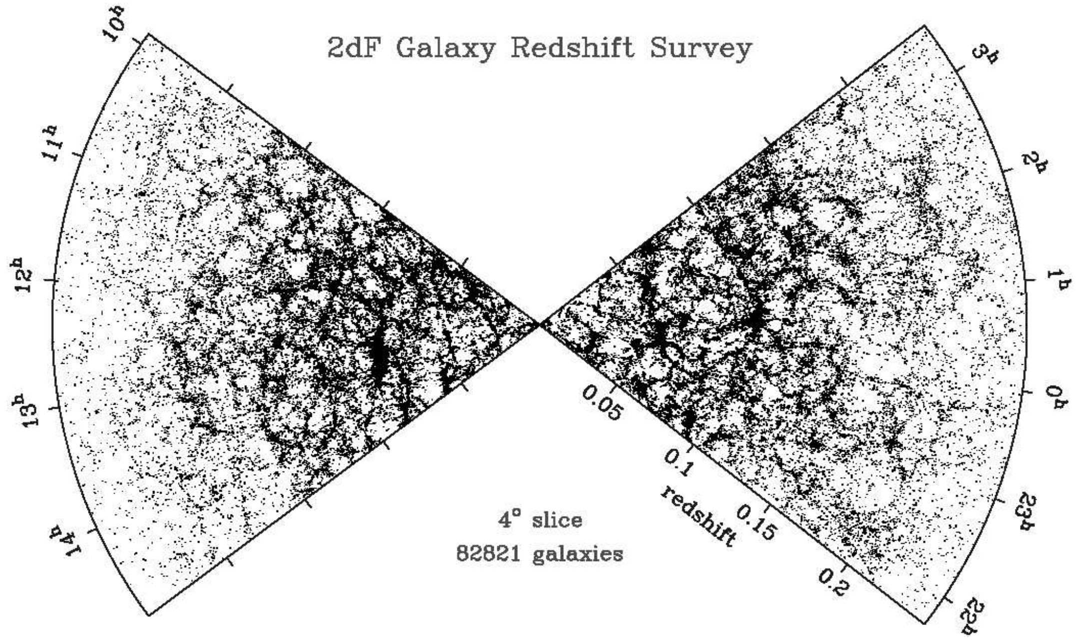

Figure 1.1: The distribution of galaxies in part of the 2dFGRS: slices 4° thick, centered at declination −2.5° in the NGP and −27.5° in the SGP. This magnificently detailed image of large-scale structure provides the basis for measuring the shape of the primordial fluctuation spectrum and hence constraining the matter content of the universe (courtesy of the 2dF Team).

mass in baryons to the overall mass would be: $f_B = \Omega_B/\Omega_m$. Assuming Ω_B to be known from primordial nucleosynthesis, the cluster baryon fraction f_B can be used to constrain Ω_B and h. The baryons in clusters of galaxies are in the form of X-ray emitting gas and stellar baryonic mass. f_B is thus estimated to be:

$$f_B = \frac{\Omega_B}{\Omega_m} \simeq f_{gas} + f_{gal}. \tag{1.15}$$

Writing $f_B = M_B/M_{tot}$, $f_{gas} = M_{gas}/M_{tot}$, $f_{gal} = M_{gal}/M_{tot}$ (with the total gravitating mass M_{tot}), Ω_m can be related to h with:

$$\Omega_m = \frac{\Omega_B}{f_{gas} + f_{gal}} \simeq \frac{\Omega_B}{0.08\,h^{-1.5} + 0.01\,h^{-1}}. \tag{1.16}$$

Assuming $\Omega_B\,h^2 \approx 0.02$ from Big Bang Nucleosynthesis, the above relation gives $\Omega_m h^{0.5} \approx 0.25$, which is consistent with $\Omega_m = 0.3$ from recent Chandra observations.

CMB:

The CMB carries a record of conditions at the time of decoupling: the primary anisotropies. As the CMB propagates towards us, it is affected by various processes: The effect of time-varying gravitational potential (integrated Sachs-Wolf effect), gravitational lensing and scattering from ionized gas at low redshifts (Sunyaev-Zeldovich effect, secondary anisotropy).

The observed angular power spectrum defined in eq.(1.12) depends on all the cosmological parameters. In a typical cosmology, the power spectrum (plotted as $\ell(\ell+1)\mathcal{C}_\ell$) has a flat plateau at large angular scales (small ℓ) and a series of oscillatory features at higher angular scales. These features (acoustic peaks) represent the oscillations of the photon-baryon fluid around the time of decoupling. Typically, the location of the first peak (now measured to be $\ell \approx 200$) probes the geometry of the Universe and the relative heights of the peaks probe the baryon density.

The most accurate results to date are provided by the WMAP experiment. A comparison of the anisotropies in the temperature maps of COBE and MAP is given in Fig.1.2. The consistency of the 30 times higher resolution and higher sensitivity WMAP results with COBE is apparent. The determination of the temperature power spectrum up to $\ell \simeq 1000$ with the first measurement of the correlation spectrum between temperature and polarization is shown in Fig.1.3.

Furthermore, WMAP gives a very precise measurement of the first acoustic peak which is consistent with spatial flatness and excludes a significantly curved Universe (see Figure 1.5). Nevertheless, one has to remark that the parameter fitting is done in a multi-parameter space and one has thus to assume a prior range for each of the parameters.

Finally, one of the most interesting results (from the large-angle polarization-temperature correlation in the first year data of from WMPA) is the discovery of high optical depth to reionization, $\tau \sim 0.17$, which corresponds in an reionization redshift $z_{ion} \sim 17$. If confirmed by further measurement this early reionization gives stringent constraints for structure formation. Warm dark matter models fail to form the necessary structures at this high redshift that could host the ionizing sources (Yoshida ett al., 2003a). The same holds for models with a running primordial power spectrum (Yoshida et al., 2003b).

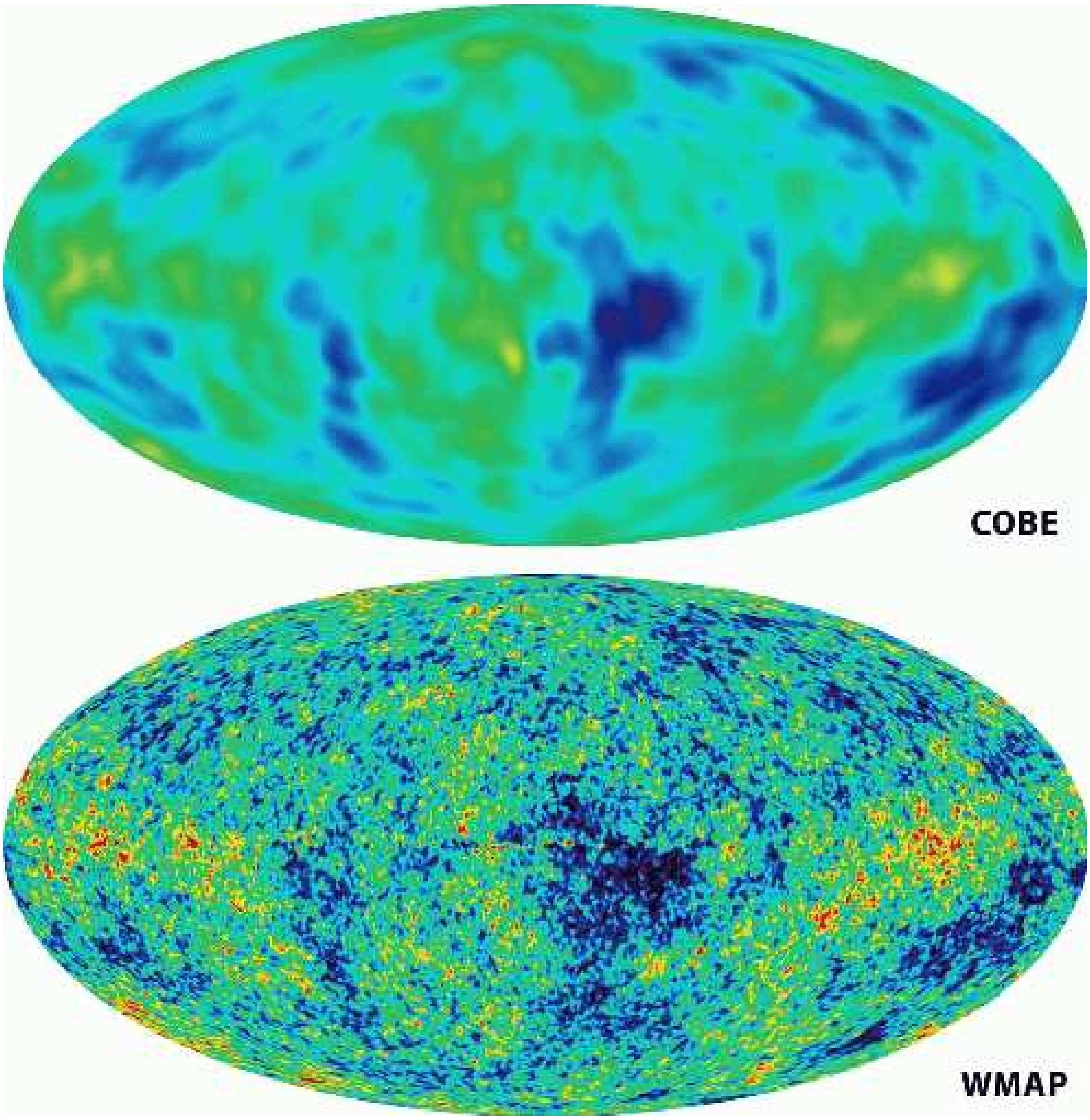

Figure 1.2: Anisotropy of the cosmic microwave background: All-sky maps, made by COBE (upper) and by WMAP (lower); range of color scale is ±200μ Kelvin (courtesy of NASA/WMAP Science Team.)

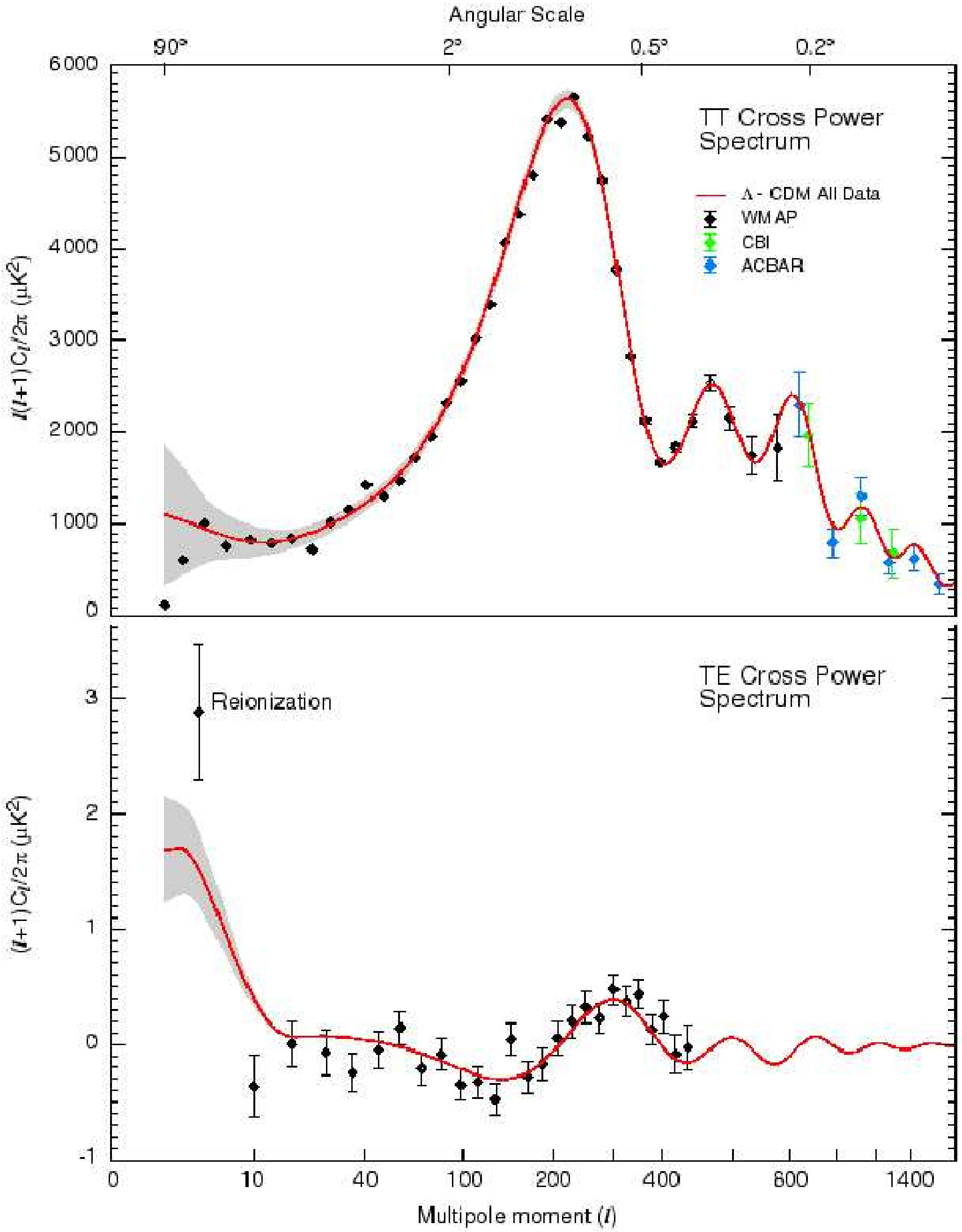

Figure 1.3: Anisotropy of the cosmic microwave background: The WMAP angular power spectrum (also includes data from CBI and ACBAR). The curve is the consensus cosmology model; the grey band includes cosmic variance. The WMAP measurements up to $\ell \sim 35$ are cosmic variance limited. The lower panel shows the anisotropy cross polarization power spectrum; the high point marked re-ionization is the evidence for re-ionization of the Universe at $z \sim 20$. (courtesy of NASA/WMAP Science Team.)

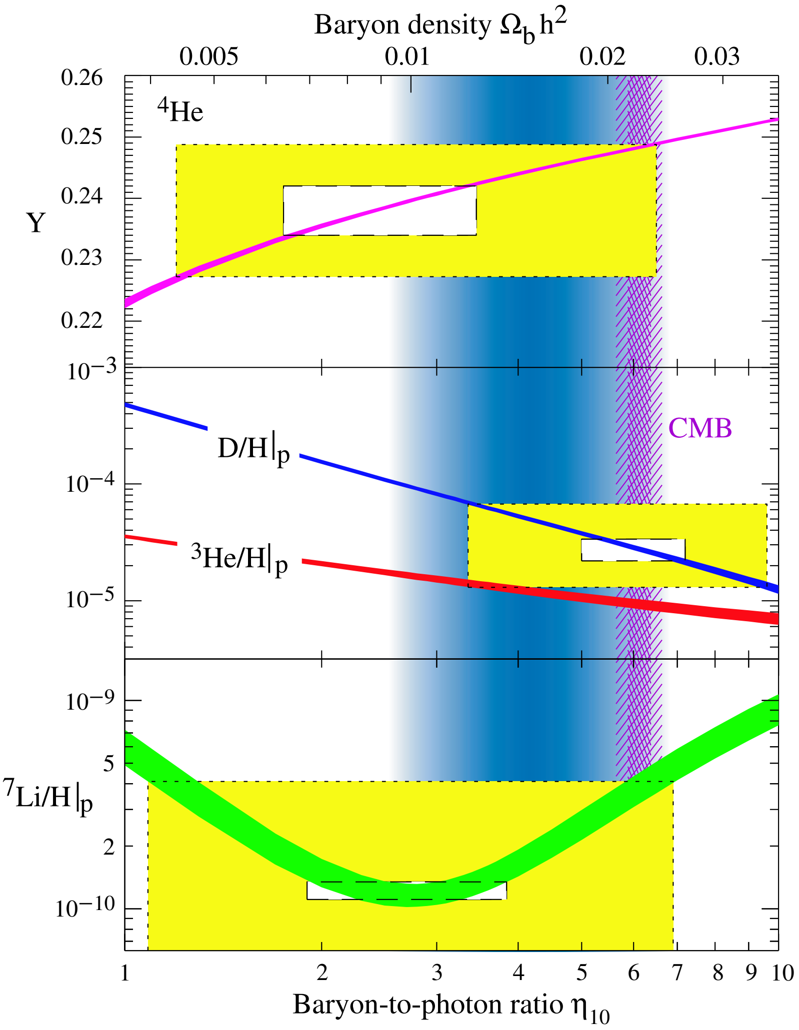

Figure 1.4: The abundances of ^{4}He, D, ^{3}He and ^{7}Li as predicted by the standard model of big-bang nucleosynthesis. Boxes indicate the observed light element abundances (smaller boxes: 2σ statistical errors; larger boxes: $\pm 2\sigma$ statistical and systematic errors added in quadrature). The narrow vertical band indicates the CMB measure of the cosmic baryon density. (courtesy of the Particle Data Group,2004).

Abundance of light elements:

A major success of the Big Bang theory is the explanation of the observed abundance ratios of the light elements, mainly Hydrogen, Deuterium and Helium (both ^{3}He and ^{4}He), and also Lithium. The predicted abundance ratios depend only one one free parameter, the baryon-to-photon ratio η. Current measurement find $\eta_{10} = \eta \times 10^{10}$ in the range 3.4-6.9 (95% CL). This implies an present day baryon density of $\Omega_B = \rho_B/\rho_{\rm crit} = (0.012 - 0.025)h^{-2}$. With $h = 0.71$ this gives $\Omega_B = \rho_B/\rho_{\rm crit} = (0.024 - 0.050)$. Since $\Omega_M \simeq 0.3$, this means that most of the matter in the universe is in some non-baryonic form. And $\Omega_B >> \Omega_{\rm lum} \simeq 0.0034$, therefore most baryons must be optically dark (Eidelman et al., 2004).

High-redshift supernovae :

Type Ia supernovae are remarkably good cosmological standard candles. From their luminosity distance and redshift and can extend Hubble's redshift-distance relation out to

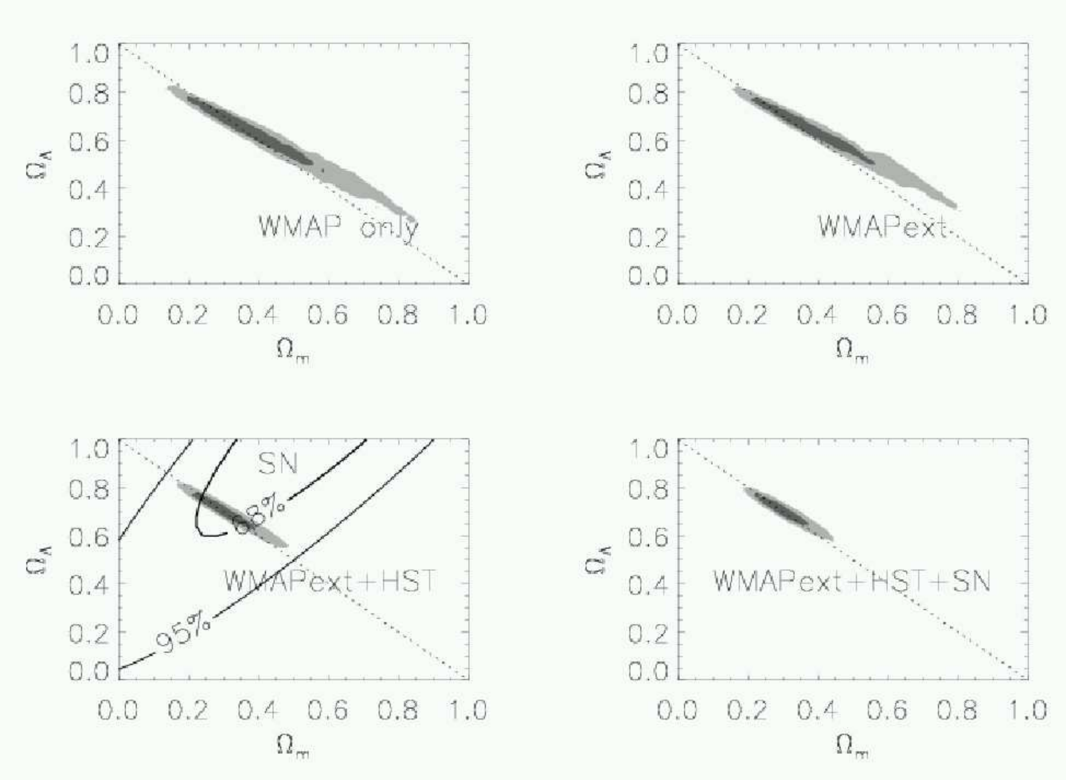

Figure 1.5: Constraints on the geometry of the universe: $\Omega_m - \Omega_\Lambda$ plane. This figure shows the two dimensional likelihood surface for various combinations of data: (upper left) WMAP (upper right) WMAPext (lower left) WMAPext + HST Key Project (supernova data (Riess et al., 1998, 2001) is shown but not used in the likelihood in this part of the panel; (lower right) WMAPext + HST Key Project + supernova . (courtesy of NASA/WMAP Science Team.).

very large distances ($z \simeq 2$), and therefore also to earlier epochs. This allows us to detect changes in the expansion rate, and has lead to the very surprising discovery that the expansion rate is *increasing*, i.e. that Λ is positive (Riess et al. 1998;Perlmutter et al. 1999). The supernova data gives constraints in the Ω_m - Ω_{Lambda} parameter plane which are complementary and consistent with the constraints from the CMB data (see Figure 1.5 and Spergel et al. 2003).

1.3 Dark matter and cosmological simulations

Dark matter was first dedected about 70 years ago by the Swiss astrophysicist Fritz Zwicky, who noted that the speeds of galaxies in the Coma cluster are much too great for a gravitationally bound object, unless there is much more mass than in the visible component (Zwicky, 1937). Today there is a large body of evidence that supports the existence of dark matter and indicates that most of it is in a non-baryonic component (see Section 1.2 and references therein). The currently favored dark matter candidate is a weakly interacting massive particle (WIMP). Due to its weak interactions it decouples from the hot radiation fluid very soon after the Big Bang before free streaming could wipe out any but the very smallest scale fluctuations. These density fluctuations probably originate from quantum fluctuations that were blown up during inflation. Due to its large mass, the thermal particle velocities are effectively zero after decoupling, leading to the name 'cold' dark matter (CDM).

Because of the early decoupling CDM can form structures on all scales down to very small masses, comparable to the mass of Jupiter (e.g. Green et al. 2004). Particles physics predicts candidates for such a CDM particle. One popular candidate is the neutralino from super-symmetric (SUSY) scenarios. There are now many experiments trying to detect the yet unknown dark matter particle(s) directly (e.g. DAMA, EDELWEISS, ORPHEUS) or indirectly (e.g. AMANDA, AMS, GLAST, MAGIC), see Eidelman et al. (2004) for details and experimental references. Experiments at the LHC at CERN will also search for indirect evidence for the existence of these particles.

CDM is the component that dominates structure formation because it is much more abundant than baryonic matter and because there is more time to grow structures since dark decouples earlier from hot cosmic plasma which suppresses structure formation. First the smallest fluctuations collapse and these clumps then merge and hierarchically to form larger structures up to the mass of galaxy clusters that are the largest virialised systems today. On scales much larger than galaxy clusters the universe is homogeneous (compare Figures 1.1 and 1.6).

The highly nonlinear process of structure formation can only be followed using numerical simulations. They require advanced computational techniques and the most powerful supercomputers. In the last decade these simulations have revealed the detailed distribution of the dark matter on scales as large as the observable universe (over a Gpc) down to the cores and subhalos of very small galaxies (a few kpc). Comparison of mock galaxy catalogues produces from CDM cosmological simulations to the observed positions of galaxies work very well, an are considered a major triumph for the CDM model (see Section 1.2).

The internal structure of CDM halos can now also be resolved thanks to advances in numerical techniques and the fast growing computational power of supercomputers: steep density cusps and a large abundance of substructures were found (see Figure 5.1). Comparisons with the observed universe brought up several difficult questions: Why are the dark matter density profiles of galaxies and clusters inferred form observations in most cases shallower than predicted? Why are there many fewer satellites around the Milky Way and Andromeda than the number of subhalos that CDM predicts? Is there enough angular momentum in CDM halos to allow the formation of pure disk galaxies? These are important challenges that the CDM model has to face on small scales, and these questions are the motivation for much of the research presented in this work.

The distribution of the baryons is much harder to calculate reliably, because of the complex interplay of various astrophysical mechanisms most of them poorly-understood (star formation, reionization by the first stars or active galactic nuclei, supernova feedback, ...). Smoothed particles hydrodynamics and adaptive mesh based codes, both combined with approximative recipes to treat the physical processes that happen below the resolved scales have brought some progress in this respect and made many interesting and observable predictions, from the formation of giant gas planets out of proto-planetary gas disks to the morphological transformations of galaxies in the dense environment of a galaxy cluster. However no one has managed yet to simulate the formation of a pure disk galaxy that resembles the observed systems.

The output of numerical simulations can be visualized in pictures (like Figures 1.6, 1.7 and 5.1) and animations[3] which are a useful way to communicate scientific results,

---

[3] Movies of our simulations are included in the electronic version of this thesis, they are also available

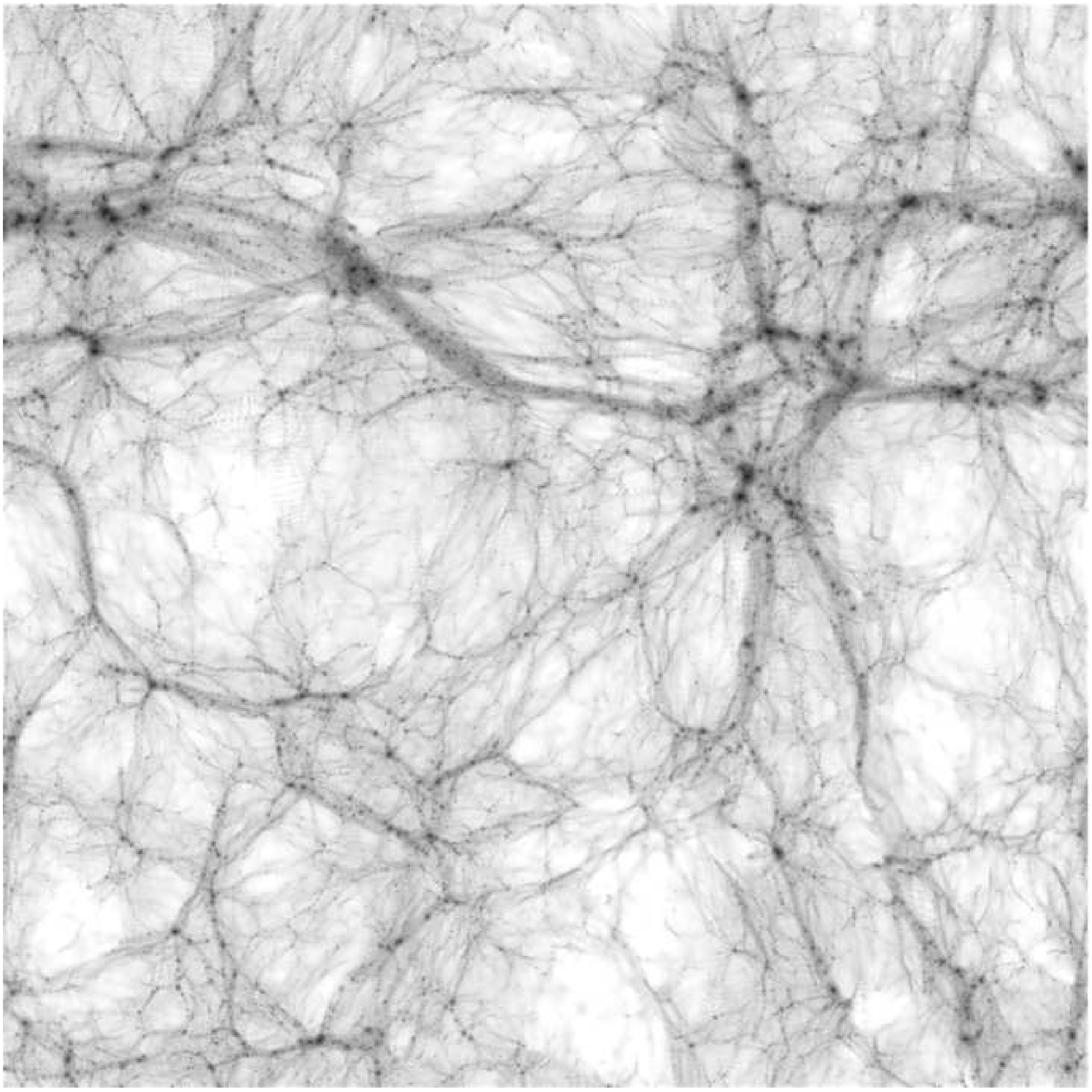

Figure 1.6: Density map of the dark matter distribution in a 30 Mpc deep slice through a 300 Mpc cube. This cube was simulated using 216 million particles, using the standard ΛCDM model with the best fit parameters form the WMAP first year data.

ideas and concepts within the research community and with also the general public. Computational astrophysics is also important in driving progress in other fields: Half of the recipients of the Gordon Bell Prize for supercomputing applications went to astrophysicists in the 1990's; numerical techniques from astrophysics have been applied in a wide range of areas, from biochemistry to fusion research.

---

on the web http://www-theorie.physik.unizh.ch/∼diemand/

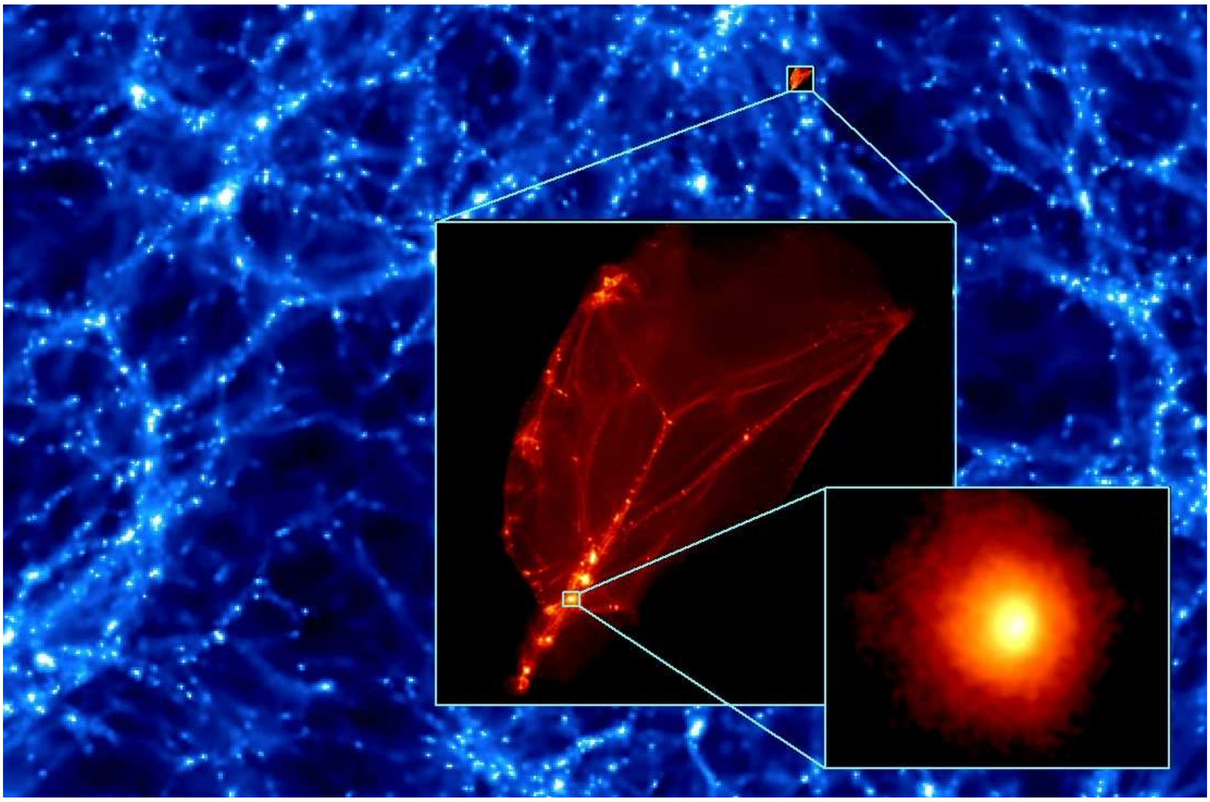

Figure 1.7: A zoom into the first object to form in the universe. The colours show the density of dark matter where brigher colours corrospond to regions of higher concentrations of matter. The blue background image shows the small scale structure in the 3 kpc top cube which has a similar filementary topology as the large scale structure in the CDM universe. The first red image zooms by a factor of 100 into one of the high resolution regions. The final image shows a close up of one of the individual dark matter halos in this region, again by a factor of hundred so that the box has length 0.03 parsecs. The halo has a cuspy density profile and is smooth, devoid of the substructure that is found within all large scale dark matter halos.

Chapter 2

Two body relaxation in CDM simulations [1]

2.1 Abstract

N-body simulations of the hierarchical formation of cosmic structures suffer from the problem that the first objects to form always contain just a few particles. Although relaxation is not an issue for virialised objects containing millions of particles, collisional processes will always dominate within the first structures that collapse. First we quantify how the relaxation varies with resolution, softening, and radius within isolated equilibrium and non-equilibrium cuspy haloes. We then attempt to determine how this numerical effect propagates through a merging hierarchy by measuring the local relaxation rates of each particle throughout the hierarchical formation of a dark matter halo. The central few percent of the final structures - a region which one might naively think is well resolved at the final time since the haloes contains $\approx 10^6$ particles - suffer from high degrees of relaxation. It is not clear how to interpret the effects of the accumulated relaxation rate, but we argue that it describes a region within which one should be careful about trusting the numerical results. Substructure haloes are most affected by relaxation since they contain few particles at a constant energy for the entire simulation. We show that relaxation will flatten a cusp in just a few mean relaxation times of a halo. We explore the effect of resolution on the degree of relaxation and we find that increasing N slowly reduces the degree of relaxation $\propto N^{-0.25}$ rather than proportional to N as expected from the collisionless Boltzmann equation. Simulated with the same relative mass resolution (i.e. equal numbers of particles) cluster mass objects suffer significantly more relaxation than galaxy mass objects since they form relatively late and therefore more of the particles spend more time in small N haloes.

2.2 Introduction

A standard technique to study the formation and evolution of gravitating systems is to perform an N-body simulation in which the mass distribution is discretised into a series of softened point particles. This solution can be exact for a star cluster where each particle represents a single star, but for cosmological simulations of the dark matter each particle

---

[1] This chapter is published in: MNRAS, 2004, 348, 977. (Diemand et al., 2004a).

can be 10^{70} times larger than the GeV mass candidates being simulated. In this approach the particles represent a coarse grained sampling of phase space which sets a mass and spatial resolution. Unfortunately these super-massive particles will undergo two body encounters that lead to energy transfer as the system tends towards equipartition. In the real Universe the dark matter particles are essentially collisionless and pass unperturbed past each other.

The processes of relaxation is difficult to quantify, but in the large N limit the discreteness effects inherent to the N-body technique vanish, so one tries to use as large a number of particles as computationally possible. Increasing the mass resolution of a given simulation allows a convergence test of properties such as the dark matter density profile i.e. Moore et al. (1998), Ghigna et al. (2000), Klypin et al. (2001) and Power et al. (2003). These authors find that to resolve the central one per cent of a dark matter halo the entire system must contain of the order a million particles. It is not known what process sets this resolution scale since with one million particles relaxation is expected to be small, even at one per cent of the virial radius.

Unfortunately in most cosmological simulations the importance of two body interactions does not vanish if one increases N. Structure formation in the cold dark matter (CDM) model occurs hierarchically since there is power on all scales, so the first objects that form in a simulation always contain only a few particles (Moore et al., 2001), (Binney & Knebe, 2002). With higher resolution the first structures form earlier and have higher physical densities because they condense out of a denser environment. Two body relaxation increases with density, so it is not clear if increasing the resolution can diminish the overall amount of two body relaxation in a CDM simulation, i.e. if testing for convergence by increasing the mass resolution is appropriate.

In isolated equilibrium systems relaxation rates can be measured from the energy dispersion. In cosmological simulations one can measure the amount of mass segregation of multi-mass simulations (Binney & Knebe, 2002) where lighter particles gain more energy from collisional processes than the heavier particles. In Section 2.3 we present a Fokker-Planck type relaxation time estimate, which was fitted to a series of test simulations (Section 2.4.1) where we explore the relaxation rates as a function of N, radius and softening parameter in both equilibrium and non-equilibrium cuspy haloes. We then use this local relaxation rate estimate to follow the relaxation history of each particle during 1000 time-steps of a hierarchical CDM simulation. The resulting degree of relaxation as a function of spatial position within galaxy and cluster mass haloes is analysed in Section 2.5 and in Section 2.6 we discuss the effects that relaxation has on haloes at $z = 0$.

2.3 A local relaxation time estimate

In this paper we adopt the energy definition of the relaxation time (Chandrasekhar, 1942) stating that the mean relaxation time T of a group of stars is the time after which the mean square energy change due to successive encounters equals the mean kinetic energy of the group:

$$T = \Delta t \, \frac{\overline{E_{kin}}^2}{\overline{\Delta E^2(\Delta t)}} \,, \tag{2.1}$$

where $\Delta E(\Delta t)$ is the energy difference of one particle after time interval Δt and the bar denotes the group average.

Note that this time is half of the relaxation time T_v defined in Binney & Tremaine (1987) who calculate a mean velocity change, because $\Delta E^2/E^2 \simeq 2\Delta v^2/v^2$. The orbit averaged Fokker-Planck estimate for T_v is

$$T_v = 0.34 \frac{\sigma^3}{G^2 m \rho \ln \Lambda}\,, \ \Lambda \equiv \frac{b_{max}}{b_{min}}\,, \tag{2.2}$$

where σ is the one dimensional velocity dispersion, ρ the density and m the particle mass. The parameters b_{min} and b_{max} are the minimum and maximum limits for the impact parameter.

To assess the degree of relaxation in cosmological simulations (section 2.5) we estimate the local relaxation rate for each particle after every time-step and integrate this up over the whole run:

$$d(t_k) := \sum_{n=1}^{k} r_{LE}(t_n)\,\Delta t\,. \tag{2.3}$$

For the local relaxation rate we use a formula similar to (2.2)

$$T_{LE} = \frac{1}{r_{LE}} = \gamma \frac{\sigma^3}{G^2 m \rho C}\,, \ \gamma \equiv 0.17\,. \tag{2.4}$$

The value of γ, and the parameters in the Coulomb logarithm C are chosen to roughly fit measured relaxation times of equilibrium haloes, see section (2.4). The Coulomb logarithm is

$$C \equiv 0.5 \left[\ln(1+\Lambda^2) - \frac{\Lambda^2}{1+\Lambda^2}\right] (\simeq \ln\Lambda,\ \text{if}\Lambda \gg 1)\ , \tag{2.5}$$

the analytical calculation for Newtonian potentials shows that $b_{min} = b_0 = 2Gm/v_{rel}^2$, b_0 is the impact parameter where the deflection angle reaches $\pi/2$ (Bertin, 2000). In a softened potential the scattering calculation has to be done numerically and the results agree roughly with the Newtonian case if one sets $b_{min} = \epsilon$, i.e. one ignores all encounters with an impact parameter smaller than the softening length (Theis, 1998). We set

$$b_{min} \equiv \max(\mathrm{Gm}/3\sigma^2, \epsilon) \simeq \max(\mathrm{b}_0, \epsilon)\,, \tag{2.6}$$

because $\overline{v_{rel}^2} = 6\sigma^2$. The proper choice of b_{max} is controversial, it is not clear whether it should be related to the size of the whole system or to the mean interparticle distance. For cosmological simulations we prefer the second choice

$$b_{max} \equiv \beta(m/\rho)^{1/3} \tag{2.7}$$

because this is a local quantity that is easy to measure and less ambiguous than defining the size of irregular shaped, collapsing structures.

We calculate the local velocity dispersion and density surrounding each particle by averaging over its 16 nearest neighbours. We do a simple top-hat average, because using an SPH spline kernel leads to biased results when using only 16 particles. We found good agreement with all measured relaxation rates (2.4) when using $\beta = 10$ and $\gamma = 0.17$. Averaging over different numbers of nearest neighbours the optimal parameters differ slightly due to different amounts of numerical noise in the local density and velocity dispersion.

2.4 Two body relaxation in spherical halo models

In this section we present a number of test cases which we used to gauge our local estimate (2.3) for the degree of relaxation and show that it agrees quite well (within 15 per cent) with measured levels of relaxation for a wide range of particle numbers, softening lengths and virial ratios. This range covers the haloes that form in cosmological simulations, however all the test cases are isotropic, spherical haloes. Haloes in cosmological simulations are close to isotropic, but are triaxial and contain substructures. But one can argue that locally the two are similar, and if a local relaxation time estimate works in the spherical haloes, it should give a reasonable estimate also in the cosmological case.

2.4.1 Equilibrium haloes

In an equilibrium model the energy of each particle would be conserved in the $N \to \infty$ limit. For finite N the energies of particles suffer abrupt changes due to encounters. Therefore we just have to measure these energy differences to get the relaxation time with (2.1).

Here we present a sequence of tests using spherical and isotropic Hernquist models (Hernquist, 1990) which are a reasonable approximation to the haloes found in cosmological N-body simulations. (We found no difference between these simulations and tests using Navarro, Frenk & White (1996) and Moore et al. (1999b) profiles, constructed by solving for the exact phase space distribution function numerically as described in Kazantzidis, Magorrian & Moore (2004a).) The density profile of the Hernquist model is

$$\rho(r) = \frac{M}{2\pi}\frac{a}{r}\frac{1}{(r+a)^3}\,. \tag{2.8}$$

We set [1] the total mass to $M = 3.5 \times 10^9 \mathrm{M}_\odot$ and the scale length to $a = 10$ kpc. Then the half mass radius is $r_h \simeq 2.4a = 24$ kpc and the crossing time at half mass radius is $T_c \equiv r_h/v_{circ}(r_h) \simeq 1.3$ Gyr.

All the simulations have been carried out using PKDGRAV, a state of the art, multi-stepping, parallel tree-code (Stadel, 2001). The time-steps are chosen proportional to the square root of the softening length over the acceleration on each particle, $\Delta t_i = \eta\sqrt{\epsilon/a_i}$. We use $\eta = 0.25$, and a node-opening angle $\theta = 0.55$ for all runs in this section, expect the long term integrations in subsection 2.4.3 where we use $\eta = 0.03$. Energy conservation was better than 0.1 per cent after several crossing times for all runs in this section.

Due to softening the initial models are not exactly in equilibrium, the total kinetic energy is a few percent larger than half of the potential energy. For this reason we evolved the models for five crossing times before measuring the energy dispersion, which results in up to 10 per cent longer relaxation times.

Figure 2.1 shows $\overline{\Delta E^2(\Delta t)}$ as a function of time within haloes constructed with $N = 10^4$ and $N = 100$ particles. The upper panel shows that for small numbers of particles $N \ll 10^3$ $\Delta E(\Delta t)$ becomes very noisy since there are fewer, but more significant encounters. To obtain more reliable results in small N groups we added a sufficiently large number (10^4) of massless tracer particles following the same distribution in real and velocity space as

---

[1] To rescale the results to different size haloes just change the distance scale by some factor $x \to fx$, mass scale $M \to f^3 M$ and the dynamical and relaxation timescales do not change. To rescale to different timescales $T \to cT$ do $M \to c^{-2}M$ with fixed length scale.

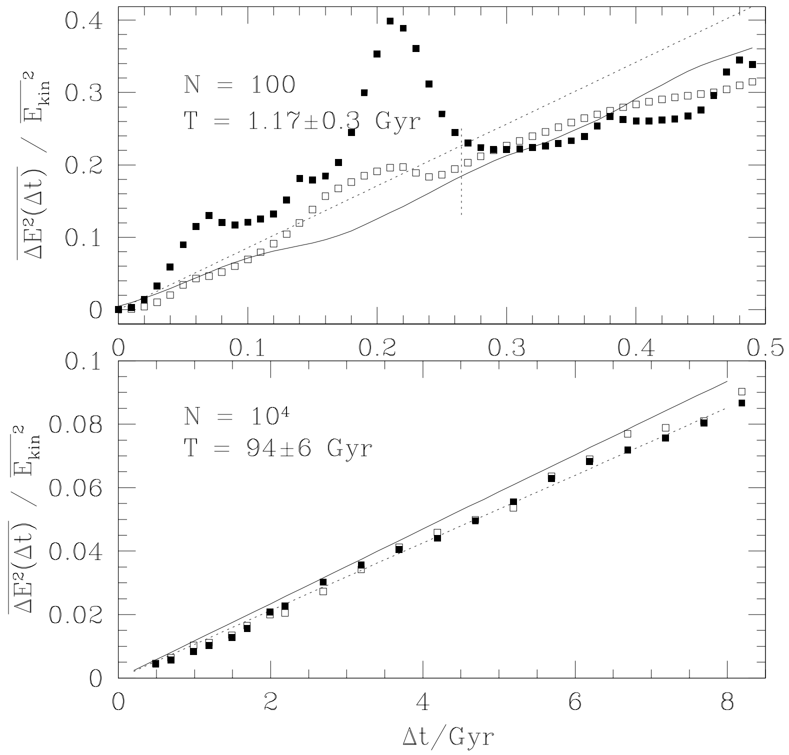

Figure 2.1: Mean squared energy change $\overline{\Delta E^2(\Delta t)}$ as a function of time. The filled squares show the mean squared energy change of the actual particles, the open squares for the massless tracer particles. The dotted lines are linear fits to the mean squared energy change of the tracers, in the upper panel only the points left of the vertical bar are taken into account. The solid lines are averages of (2.3) over all massive particles.

the massive particles. The open squares in Figure 2.1 show the 'energy' dispersion of the tracers, which in large N groups is just the same as the energy dispersion of the massive particles, but it evolves much smoother with time in small N groups. We obtain the mean relaxation times (2.1) of these haloes with linear fits to the energy dispersion of the tracer particles (open squares), taking into account points where $\overline{\Delta E^2} < 0.2$, i.e. in the upper panel only the points left of the vertical bar, to make sure that Δt is small compared to the relaxation time. The local relaxation estimate (solid line) (2.4) gives similar average degrees of relaxation in these test cases (see also Figures 2.2 and 2.3).

Note that the tracers are not in equilibrium with the halo, on average they gain speed in encounters and are ejected from the core. Typically after one relaxation time the number of tracers inside of $r = a$ drops to one half of the initial number. Therefore it is important to use a Δt shorter than T and to add the tracers after evolving the halo for five crossing times, otherwise the relaxation in the core is not sufficiently reflected in the energy dispersion of the tracers and T could be underestimated significantly.

2.4.1.1 Dependence on N and softening

Figures 2.2 and 2.3 show the measured mean relaxation times as a function of N and softening parameter, ϵ, compared with the average over all particles of the local relaxation estimate (2.4). We find that the measured relaxation times are proportional to N (dashed

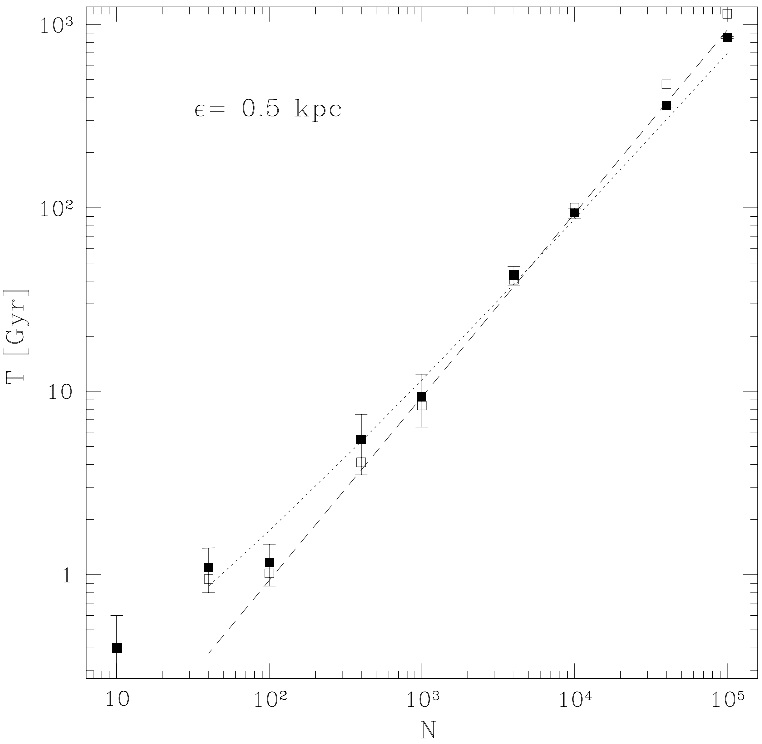

Figure 2.2: Average relaxation times of isotropic Hernquist models versus particle number N, with a constant softening $\epsilon = 0.5$ kpc. The filled squares are the measured relaxation times, with error bars form the linear fit of $\overline{\Delta E^2(\Delta t)}$. The open squares are the local estimates of the relaxation time (2.4).

reference line), rather than to $N/\ln(N)$ (dotted line), as expected for a softened potential. The same result was found for King models by Huang, Dubinski & Carlberg (1993). The local estimate of the relaxation time increases slightly faster with N than the measured values. This is due to the fact that we choose a maximum impact parameter proportional to the mean interparticle separation, i.e. $b_{max} \propto N^{-1/3}$, but the difference is less than 10 per cent for all relaxation times shorter than a Hubble time, i.e. for $N \leq 10^4$.

The dependence on the softening length is shown in Figure 2.3 for a $N = 10^4$ model. The measured values (filled squares) increase faster with ϵ than the local estimate (open squares) (like in Figure 2 of Huang et al. 1993), but the differences are small ($\gtrsim$15 per cent) for realistic softenings $\epsilon \lesssim 0.1a = 1$ kpc. The average relaxation time of this model increases from 30 Gyr to 180 Gyr when the softening parameter is changed from 0.01 kpc to 1 kpc. This is slightly higher than expected from the scaling with $\ln(\epsilon)$ since the density profile and central cusp are better resolved with smaller softening.

2.4.1.2 Dependence on radius

Measuring the relaxation time as a function of radius $T(r)$ proved to be quite difficult. The most credible method seems to take (2.1) and replace the average over all particles by the average over those which are in the corresponding radial bin at the beginning (or at the end) of the time interval Δt. Clearly one has to choose $\Delta t \ll \delta r/\sigma(r)$, where δr is the size of the bins, to make sure that most particles spend most of Δt in the same bin.

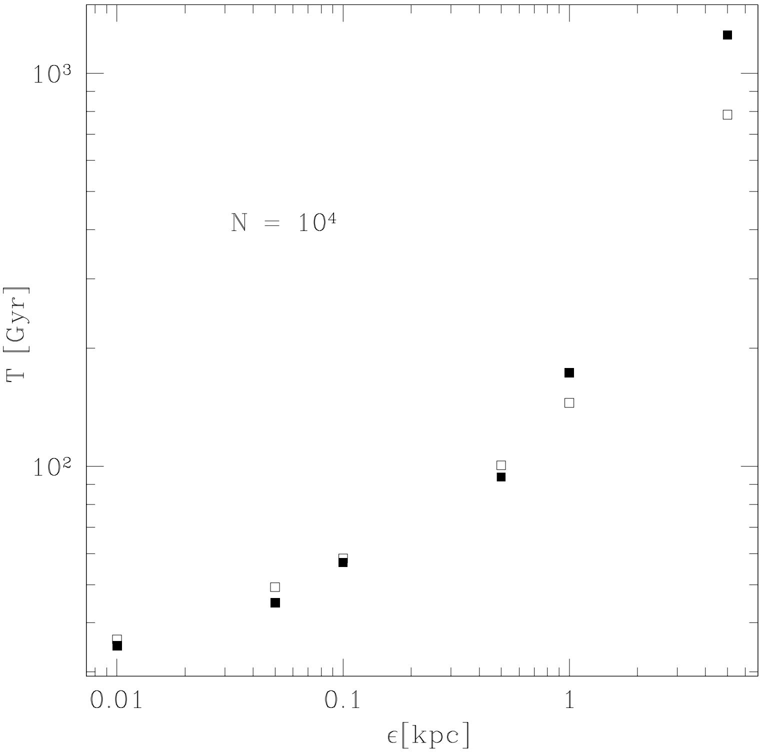

Figure 2.3: Average relaxation times of an $N = 10^4$ Hernquist models versus softening length ϵ. The filled squares are the measured relaxation times, the open squares are the local estimate (2.4).

This could also be achieved by placing the tracers on circular orbits, which leads to very similar results for $T(r)$ if $r \sim r_h$, but in to the centre this method fails, because there the circular velocity is much smaller than the velocity dispersion[2].

In Figure (2.4) we plot the relaxation rate against radius for a Hernquist model with 10^4 particles. We measured the energy dispersion (filled squares) during $\Delta t = 0.1$ Gyr for each particle, and averaged the values of particles starting in the same radial bin. We also measured the local relaxation rate r_{LE} (2.4) at 100 time-steps during Δt for each particle and summed them up. The radial averages are plotted with open squares. Again the agreement with the measured energy changes is better than 35 per cent except in the last three bins where the relaxation rates are many thousands of Gyrs and the local relaxation measurement overestimates the true rate of relaxation. In the inner three bins the crossing times are shorter than 0.2 Gyr, i.e. many of the particles had time to move through these bins during $\Delta t = 0.1$ Gyr.

The dashed line is the inverse of half the Fokker-Planck estimate (2.2) with $\Lambda = r_h/\epsilon$, calculated using all particles in the bin, not only from 16 nearest neighbours. It scales like the phase space density $\rho(r)/\sigma^3(r)$ which scales almost exactly like r^{-2} in a Hernquist model. The local estimate also follows this r^{-2} scaling in the seven outer bins. The measured relaxation scales more like $\propto r^{-3}$ in the outer region, but the slope depends strongly on Δt, i.e. on how many particles from the core with 100 times higher relaxation rate have had time to reach the outer region.

The average relaxation times[3] are about 10 times shorter than measured relaxation times at half mass radius, due to the fast relaxation in the high density core of cuspy haloes. For a less concentrated King model ($\Psi_0 = 5$) the Fokker-Planck estimate seems to agree not only with the measured relaxation time at half mass radius, but also with the mean relaxation time (Huang et al., 1993).

2.4.2 Non-equilibrium systems

The definition of the relaxation time (2.1) is mostly used for systems close to dynamical equilibrium like globular clusters, i.e. systems with constant (or only slowly changing) mean kinetic energy. In this case the mean relaxation rate is also (roughly) constant and the degree of relaxation grows linear with time (like in Figure 2.1). Generalising this definition to non-equilibrium situations is straightforward: The degree of relaxation of a group at some given time is the accumulated mean square energy change due to encounters divided by the mean square kinetic energy at this time.

Now not all energy changes are due to encounters, so one needs another method to measure the degree of relaxation. Again we use massless tracer particles like in the last section. Instead of setting up their initial conditions exactly like those of the massive particles, one can also restrict the tracers to a common orbital plane. In a spherical system this does not change their density profile nor the relative velocities in encounters with the massive particles. If we choose the orbital plane of the tracers to be the xy-plane,

---

[2] From a convolution of the velocity distributions one finds that the relative velocities in encounters with tracers on circular orbits have a different dispersion ($\sigma^2_{v_{rel}} = 3\sigma^2 + v^2_{circ}$) than those of encounters between the massive particles ($\sigma^2_{v_{rel}} = 6\sigma^2$). In non isothermal haloes, $3\sigma^2 \neq v^2_{circ}$ and this leads to systematic errors in the measured relaxation times. In Hernquist models $3\sigma^2 \sim v^2_{circ}$ holds only for $r \sim r_h$, and indeed we found good agreement with the other methods only in this range.

[3] Note that analytically the average of the relaxation rate estimate r_{LE} (2.2) is divergent for models with central cusps $\propto r^{-1}$ and steeper: $T = \int_0^R r_{LE}(r)\rho(r)r^2dr \propto \int_0^R r^{-2}\rho(r)r^2dr = \int_0^R \rho(r)dr$.

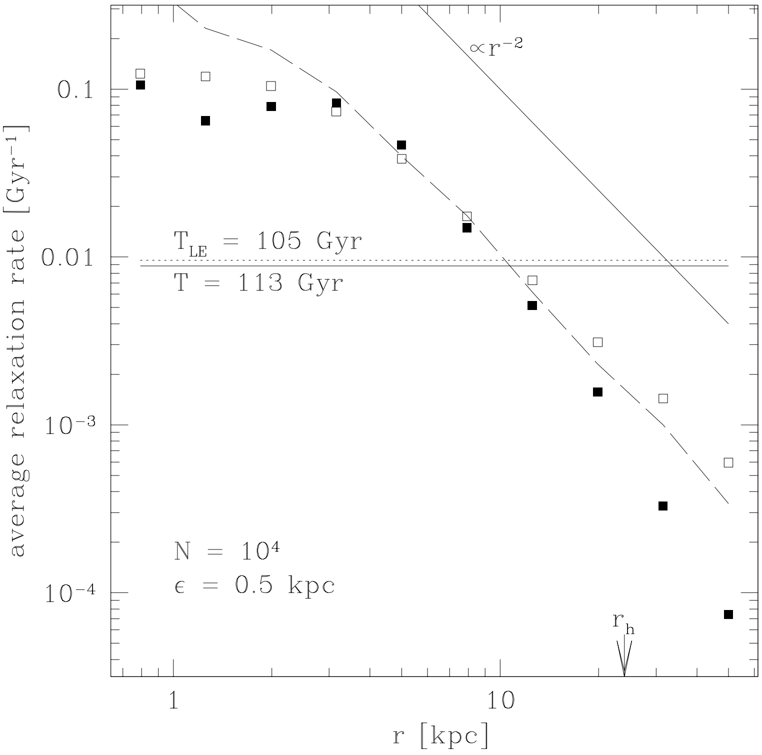

Figure 2.4: Relaxation rate of an $N = 10^4$ halo vs. radius. The filled squares are the measured relaxation, the open squares are the local estimate r_{LE}, calculated from 16 nearest neighbours during 0.1 Gyr. The horizontal lines give the halo averages of measured (solid line) and estimated (dotted line) relaxation rates. We also plot $2/T_v$ (dashed line) calculated from all particles in the radial bin.

then the accumulated energy change due to encounters $\Delta_{enc}E$ is

$$\frac{\overline{\Delta_{\rm enc}E(t)^2}}{\overline{E_{kin}(t)}^2} \simeq \frac{\overline{\Delta_{\rm enc}E_{kin}(t)^2}}{\overline{E_{kin}(t)}^2} \simeq 2\frac{\overline{\Delta_{\rm enc}v(t)^2}}{\overline{v(t)}^2} = 4\frac{\overline{v(t)_z^2}}{\overline{v(t)}^2}\,, \tag{2.9}$$

as long as $v_z(t)^2 \ll v(t)^2$, i.e. for small degrees of relaxation. This relates the energy dispersion to a more demonstrative quantity and in the edge on view of the xy-plane one can actually observe the relaxation process since the degree of relaxation is roughly proportional to the thickness of the disk[4]. When the amount of relaxation approaches unity (2.9) tends to underestimate the degree of relaxation, because tracers on new out of plane orbits will eventually reach a turnaround point where $v_z = 0$. Also the probability that one tracer suffers more than one encounter grows with time, therefore one should place a new set of tracers into the plane to get an accurate relaxation rate as soon as the amount of relaxation is close to unity.

With (2.9) we can measure the amount of relaxation in non-equilibrium situations, we only need one symmetry plane to be able to apply this method, therefore it allows us to measure the amount of relaxation during a collapse or a merger.

2.4.2.1 Collapsing haloes

In CDM simulations the virial ratio $\alpha \equiv 2E_{kin}/|E_{pot}|$ is close to zero at the beginning of a halo collapse and grows towards unity as the halo reaches dynamical equilibrium. In the previous sections we showed that the local estimate (2.4) works for $\alpha = 1$, but for $\alpha \to 0$ the phase space density $\propto \alpha^{-1.5}$ goes to infinity. Down to which virial ratio can we trust our local estimate?

To answer this question we began with equilibrium Hernquist models (same parameters as in section 2.4.1.1) with 10^4 particles and multiplied all velocities with $\sqrt{\alpha}$. Therefore $\sigma^3 \propto \alpha^{1.5}$ and the phase space density $\rho/\sigma^3 \propto \alpha^{-1.5}$. To these models we added 10^4 massless tracer particles with the same phase-space distribution and tilted their orbital planes into the xy-plane. Then we measure $\overline{v_z^2}/\overline{v}^2$ and the local estimate (2.4) at 100 time-steps during the first 0.1 Gyr of the collapse. Linear fits give the relaxation times plotted in Figure (2.5), the dashed line shows the scaling $\propto \alpha^{1.5}$ expected from the Fokker-Planck type estimates (2.2) and (2.4), since these times are proportional to one over phase-space density. Our relaxation time estimate becomes very small when the virial ratio goes to zero, but the measured relaxation times remain on the order of a few dynamical times. T_{LE} is within a factor of two for $\alpha \gtrsim 0.075$ and within 10 per cent for $\alpha \gtrsim 0.5$. Also after the first 0.1 Gyr the local estimate follows the measured values, one example ($\alpha = 0.25$) is plotted in the top panel of Figure (2.6).

2.4.2.2 Mergers

The last test case for the local relaxation estimate is a merger of a small system into a more massive one. The problem in this case is that the small halo gains a lot of kinetic energy when falling into the main halo, so its accumulated energy changes due to encounters can become smaller *relative* to the mean kinetic energy of the group. A local estimate can never capture this decrease since it can not know about the gain in external kinetic

---

[4] Simulation movies are available at: www-theorie.physik.unizh.ch/~diemand/tbr/

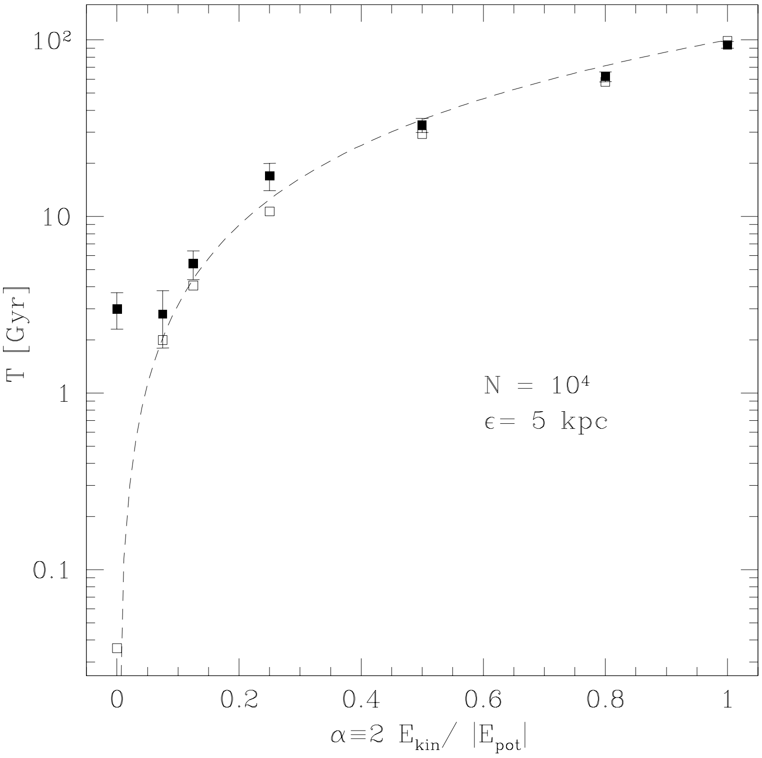

Figure 2.5: Relaxation times of a $N = 10^4$ non-equilibrium Hernquist model vs. virial ratio. The filled squares are measured with $\overline{v_z^2}/\overline{v}^2$, the open squares are the local estimate (2.4). The reference line is $\propto \alpha^{1.5} \propto v^3/\rho$.

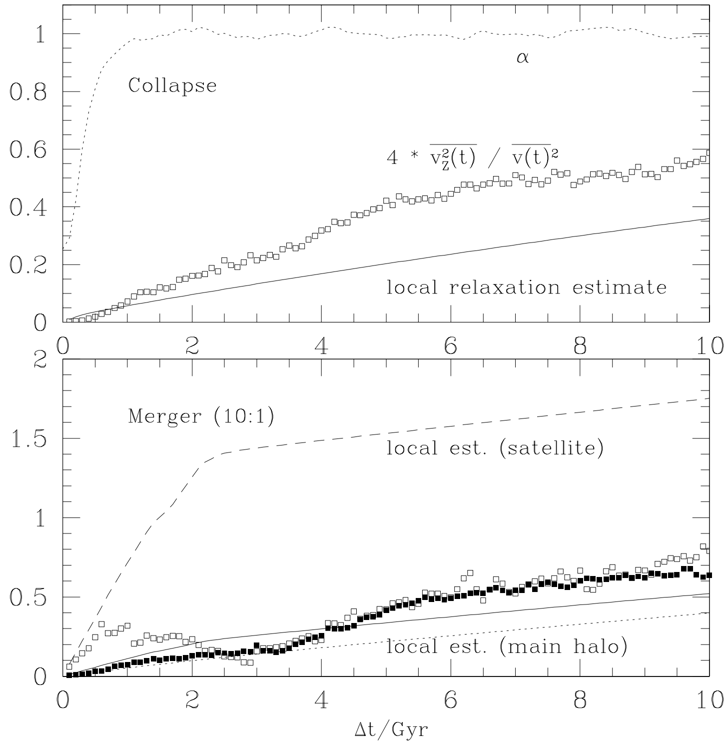

Figure 2.6: Average degrees of relaxation during a collapse of an $N = 10^4$ Hernquist halo, the initial virial ratio α is 0.25 (top). The lines are the average of the local relaxation estimate (2.4), the squares are the amount of relaxation measured from a group of tracer set in a plane initially (2.9). The bottom panel shows average degrees of relaxation during a a merger of an $N = 10^3$ halo into a ten times more massive system with $N = 10^4$. Here the open squares are the measured average for the satellite and the filled squares for the main halo.

energy. For a surviving subhalo one can argue that its accumulated energy changes should still be compared to its roughly constant internal kinetic energy to get an estimate of how affected it is by relaxation. But for haloes that are disrupted (and stripped particles from subhaloes) one has to worry about how their overestimated degrees of relaxation affect the average relaxation of the main halo.

The bottom panel of Figure (2.6) shows how relaxation develops in a head on merger of a $N = 10^3$, $a = 3$ kpc halo into a ten times more massive halo with $N = 10^4$ and $a = 10$ kpc. The initial separation was 100 kpc with a small relative velocity of 2.2 km/s. The satellite falls in and reaches the centre of the main halo after 3 Gyr. Note how the relaxation of the satellite (open squares) *decreases* during infall, this can not be followed by the average local estimate (2.4) of the satellite (dashed line), but still the average over the whole system (solid line) gives a good estimate for the mean degree of relaxation. We also verified this for equal mass mergers, there the decrease during infall is small because both haloes have quite large internal energies initially.

2.4.3 Evolution of isolated halos

The dynamical evolution of globular clusters is driven by relaxation, which can lead to core collapse and evaporation on a timescale of a few tens of half mass relaxation times, i.e. the core loses energy to an expanding outer envelope of stars and gets denser and hotter (Binney & Tremaine 1987; Spitzer 1987).

In the next section we show that haloes in cosmological simulations are typically between one and ten mean relaxation times old. (In terms of the much longer half mass relaxation time they are younger than one or two half mass relaxation times.) Therefore we do not expect that density profiles in cosmological simulations are significantly affected by the core collapse process.

Studies of globular cluster evolution start with models that are isothermal in the centre (e.g. Plummer spheres, King models) and then show a slow but monotonic density increase in the core. In contrast the cuspy haloes in cosmological simulations are not isothermal: the velocity dispersion decreases in the central regions. In this case relaxation leads to an energy flow inwards, the core evolves towards a less dense, isothermal state first. Later the system evolves just like the models in globular cluster calculations (Quinlan, 1996). The N-body simulations of Hayashi et al. (2003a) show this evolution starting from an NFW profile. We confirmed their result by evolving an $N = 4'000$ Hernquist model for 360 crossing times (see Figure 2.7).

Figure 2.8 shows the evolution of five $N = 4'000$ Hernquist models during 16 Gyr, using a softening of $\epsilon = 0.1$kpc. For this long term evolution we use a more conservative time step parameter $\eta = 0.03$, energy is conserved within 0.36 per cent even after 360 crossing times. The crossing time at the half mass radius is 1.3 Gyr, the initial mean relaxation time is 16 Gyr and the initial half mass relaxation time is 71 Gyr. After 50 Gyr this halo is about three mean relaxation times old, a realistic value for haloes in current cosmological simulations, see section (2.5). The same would happen to a $N = 100$ halo in only 1.25 Gyr, we use $N = 4'000$ just to have a well defined density profile down to $0.1a = 1$ kpc.

Within few mean relaxation times the velocity dispersion rises in the centre and at the scale radius it drops slightly, in the end the core is already close to isothermal. This energy gain is compensated with core expansion, the inner two mass shells plotted in

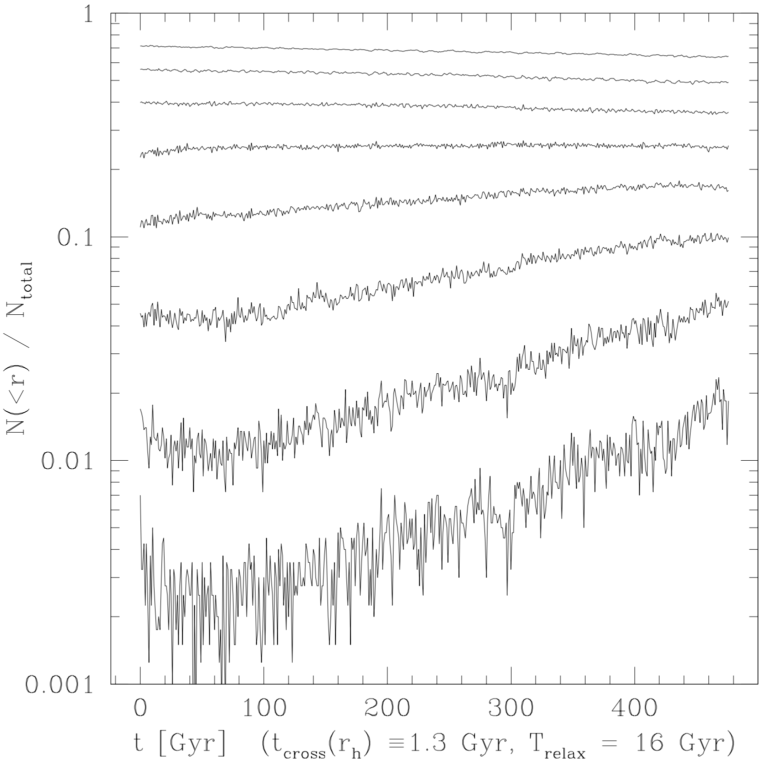

Figure 2.7: From top to bottom, the mass fraction within $0.89, 1.58, 2.81, 5.00, 8.90, 15.8, 28.1$ and 50.0 kpc of a $N = 4'000$ Hernquist models vs. time.

Figure 2.8 clearly lose mass. This is not a numerical artifact, the softening we used is much smaller than the inner bin and in a $N = 4 \times 10^4$ reference model the mass loss in the inner two bins is about ten times slower, i.e. this is really an effect driven by relaxation. The corresponding density profiles are less steep in the inner 3 per cent of the halo, see Figure 2.9, and show constant density cores in this region.

2.5 Relaxation in cosmological simulations

Here we present results from four low to medium resolution ΛCDM simulations ($\Omega_\Lambda = 0.7$, $\Omega_m = 0.3$, $\sigma_8 = 1.0$). We generate initial conditions with the GRAFIC2 package (Bertschinger, 2001). We start with a 128^3 particle cubic grid with a comoving cube size of 60Mpc (particle mass $m_p = 3.6 \times 10^9 \mathrm{M}_\odot$). Later we refined two interesting regions, in the first one a cluster halo ($M_{200} = 7.4 \times 10^{13} \mathrm{M}_\odot$, $r_{200} = 1440$ kpc) forms, the refinement factors are 2 and 3 in length, ie. 8 and 27 in mass (run C2,C3). In the second region a galaxy size halo ($M_{200} = 1.4 \times 10^{12} \mathrm{M}_\odot$, $r_{200} = 350$ kpc) forms. There we used a refinement of 9 in length, ie. 729 in mass, and included a buffer region, about 2 Mpc deep, with an intermediate refinement factor of 3 (run G9). We start the simulations when the standard deviation of the density fluctuations in the refined region reaches 0.2. The softenings used in the refined regions are $\epsilon = 1.86$ kpc for the cluster and $\epsilon = 0.5$ kpc for the galaxy. i.e. $\epsilon \simeq 0.0013 r_{vir}$ in both cases. We also run the unrefined cube again with this softening in the cluster forming region (run C0). The numerical parameters are as in section 2.4.1, but at late epochs we use a larger node-opening angle to speedup the runs, $\theta = 0.7$ for $z < 2$.

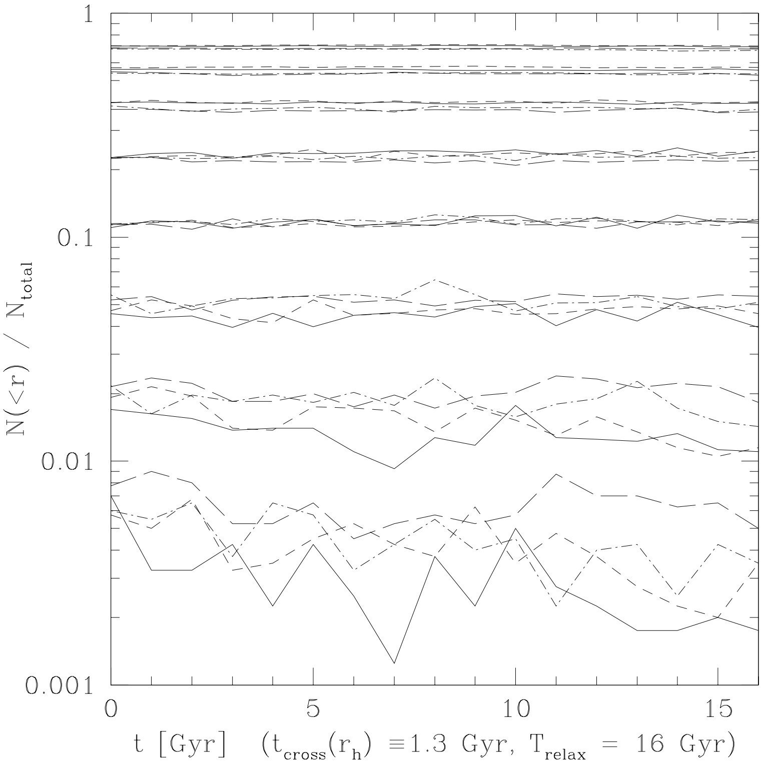

Figure 2.8: From top to bottom, the mass fraction within $0.89, 1.58, 2.81, 5.00, 8.90, 15.8, 28.1$ and 50.0 kpc of five $N = 4'000$ Hernquist models vs. time.

In non equilibrium, non spherical haloes of a cosmological simulation it is not possible to measure two body relaxation times with the methods used in section 2.4. Binney & Knebe (2002) used initial conditions with two species of particles with different mass. Both species start from a regular lattice, such that the nodes of one grid are at the centres of the cells of the other, and both are then displaced according to the Zel'dovich approximation. In a collisionless simulation the final distribution of the particles would be independent of mass. They found differences in the number density of the light and heavy particles in the centres of haloes.

Here we compliment the study of Binney & Knebe by applying the results of the previous sections to cosmological simulations. We assign a degree of relaxation d to each particle, which is calculated after each of 1000 fixed time-steps Δt from the local relaxation rate estimate (2.4) and summed up over the whole cosmological simulation (2.3).

As shown in section 2.4.2.1, r_{LE} reflects the measured relaxation rates only for virial ratios $\alpha \gtrsim 0.1$. Since this is not case for the first steps in a CDM simulation, we set r_{LE} to zero before the local density reaches some threshold. When the local density reaches $6\rho_0$ ($\simeq$ density at turnaround in the spherical collapse) the typical values for α are close to 0.4, later at $170\rho_0$ ($\simeq$ density at virialisation in the spherical collapse) α is close to unity. We used these two density thresholds, in the first case we write $d_{\rm TA}$ for the "degree of relaxation since turnaround", otherwise $d_{\rm VIR}$ for "degree of relaxation since virialisation". The relaxation averages over all particles inside r_{200} and $0.1\,r_{200}$ at $z = 0$ are given in table 2.1.

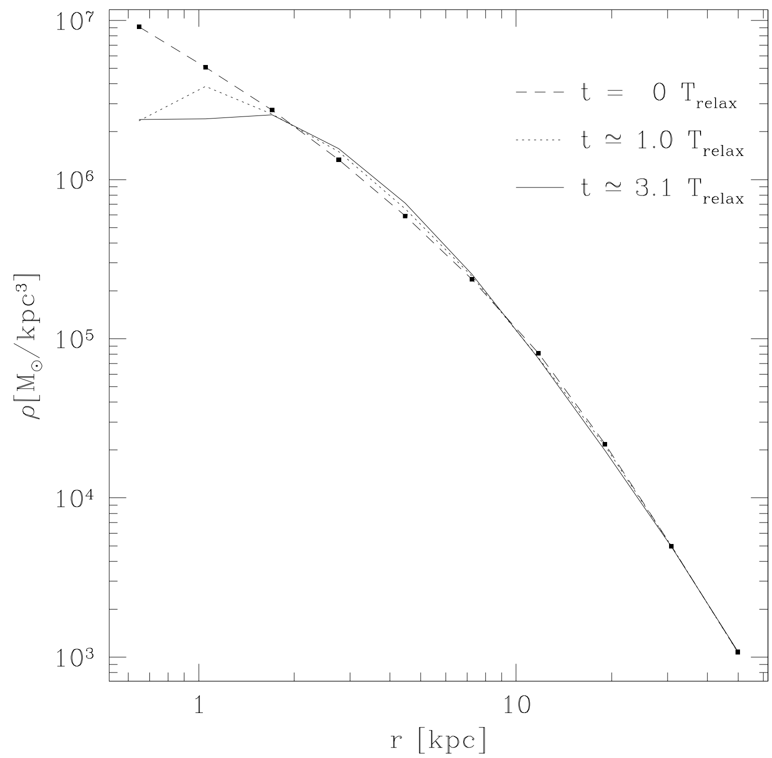

Figure 2.9: Averaged density profiles of five $N = 4'000$ Hernquist models (same models as in Figure 2.8), initial profile (dashed line), after 16 Gyr (dotted line) and after 50 Gyr (solid line). The points indicate the radius of the outer borders of the spherical bins.

Table 2.1: Average Degrees of Relaxation

Run	C0	C2	C3	G9
N_{200}	$20'500$	$177'000$	$650'000$	$250'000$
d_0 inside $0.1r_{200}$	5.98	3.62	3.06	1.67
d_0 inside r_{200}	5.23	3.34	2.52	1.15
d_{TA} inside $0.1r_{200}$	4.74	2.40	1.78	0.72
d_{TA} inside r_{200}	3.67	2.42	2.12	1.02
d_{VIR} inside $0.1r_{200}$	3.58	1.61	1.17	0.42
d_{VIR} inside r_{200}	2.50	1.52	1.34	0.58

2.5.1 Number of particles

A reassuring result is that with more particles the simulations are less affected by two-body relaxation, even though one resolves more small N progenitors. This confirms the significance of convergence tests that vary the number of particles. The average degree of relaxation inside of $0.1r_{200}$ scales like $N^{-0.3}$, and the relaxation inside of r_{200} like $N^{-0.2}$.

Figure 2.11 shows the relaxation in the cluster as a function of the final particles position, for three different resolutions. In the outer part ($r \gtrsim 0.1r_{200}$) the cluster has substructure, which are small N systems that exist at the present time, so they are still relaxing at a high rate at $z = 0$ (bottom panel). Substructure haloes with $N \simeq 500$ can reach averages of $d_{\mathrm{VIR}} \simeq 10$ in all runs, the highest peaks in d_{VIR} are found in the centre of substructure haloes, where d_{VIR} can be as high as 100, much higher than in the centre of the host halo (see Figure 2.10).

Note that the degrees of relaxation (top and middle panel) are much larger than what you would estimate using the final distribution of particles (bottom panel). Other studies consider only the relaxation rate at $z = 0$, and claim to resolve a halo down to a radius where this relaxation time $r_{LE}^{-1}(z = 0)$ is larger than Hubble time (Power et al., 2003) or larger than three Hubble times (Fukushige & Makino, 2001). This radius scales $\propto N^{-0.5}$, whereas convergence in N-body simulations seem to be slower; In Moore et al. (1998) and Ghigna et al. (2000) the resolved radii are determined by comparing density profiles between simulations with different numbers of particles. They found that the "resolved radius" $r \simeq 0.5(N_{200}/V_{200})^{-1/3}$ for a wide range of N_{200} fromm 10^2 to $10^{5.7}$. It appears like the resolved radius scales in the same way as the average degree of relaxation, but further relaxation studies for a wider range N are needed to verify this.

2.5.2 Mass and time dependence

Figure 2.12 compares the relaxation rate within the high resolution cluster and the galaxy simulations. The average degree of relaxation at $z = 0$ for the galaxy ($\overline{d_{\mathrm{VIR}}} \simeq 0.58$) is much smaller than for the cluster ($\overline{d_{\mathrm{VIR}}} \simeq 1.34$), even though N is larger for the cluster and therefore the present relaxation rate $r_{LE}(z = 0)$ is smaller in the cluster. The reason is that the cluster forms much later than the galaxy therefore most of its particles have spent a longer period of time in small N progenitor haloes.

In Figures 2.13 and 2.14 we plot how the degree of relaxation increases with time for both haloes for particles within 10 per cent of the virial radius and for all the particles within the virial radius. Most of the relaxation within the central region of the galaxy occurs within the first couple of Gyrs of the evolution of the Universe. The cluster forms over a longer timescale and this is reflected in the longer increase in the degree of relaxation with time.

The cluster runs (C0,C2,C3) show how relaxation in small N groups starts earlier, after 1 Gyr the highest resolution run (C3) is most affected by relaxation. This result is not an artifact from using a density threshold, we checked that the d_0 shows the same behaviour as d_{VIR}. The entire haloes (bottom panel) show some relaxation during the whole simulation which arises from the poorly resolved substructure haloes in the outer regions.

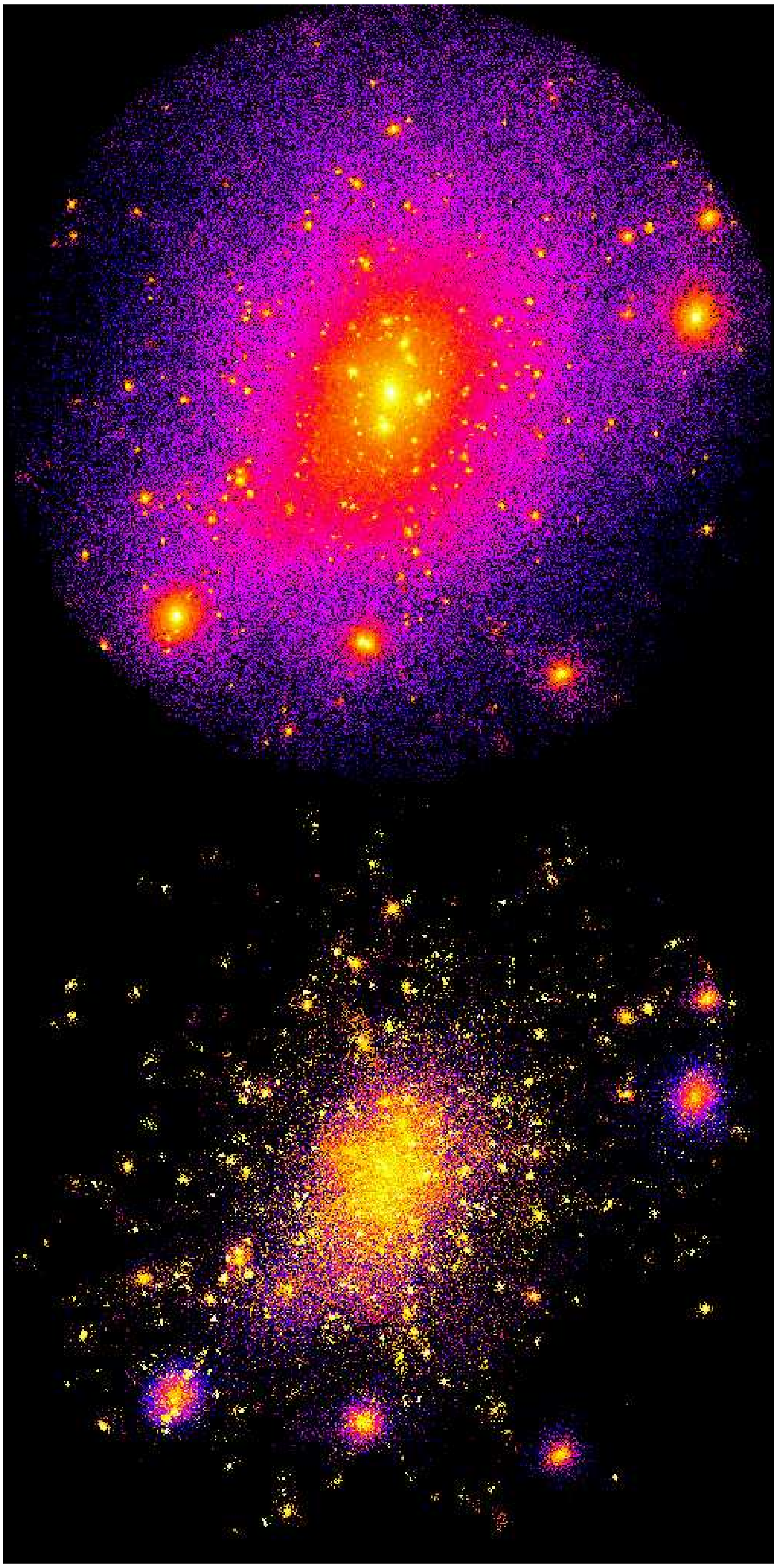

Figure 2.10: Maps of the cluster's density (top) and relaxation since virialisation (bottom) out to r_{200} for the C3 run ($N_{200} \simeq 650'000$). The logarithmic scale for the degree of relaxation goes form 0.01 (black) to 100 (white).

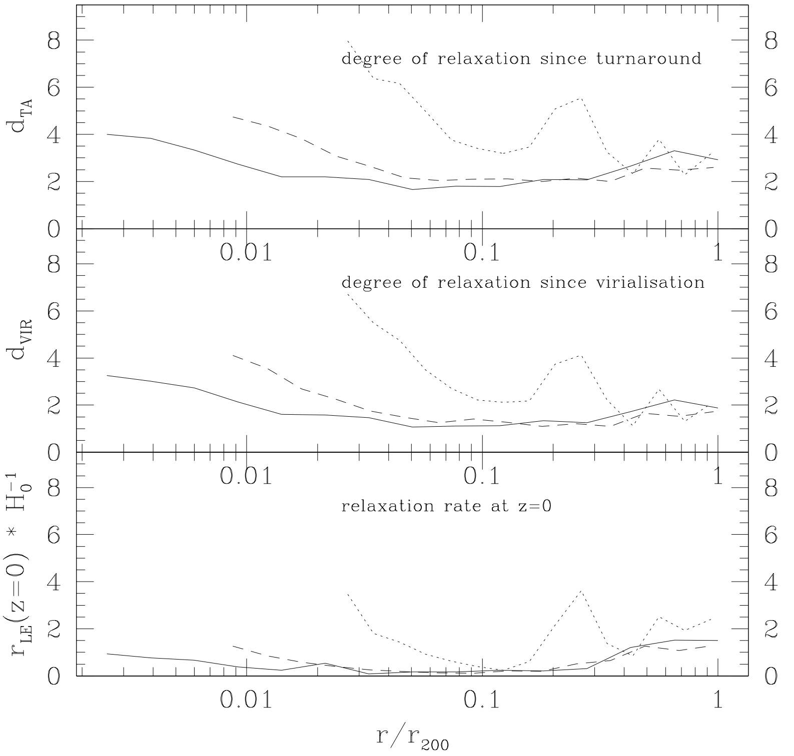

Figure 2.11: Relaxation versus radius. The solid line is for run C3, the dashed line for run C2 and the dotted line for run C0.

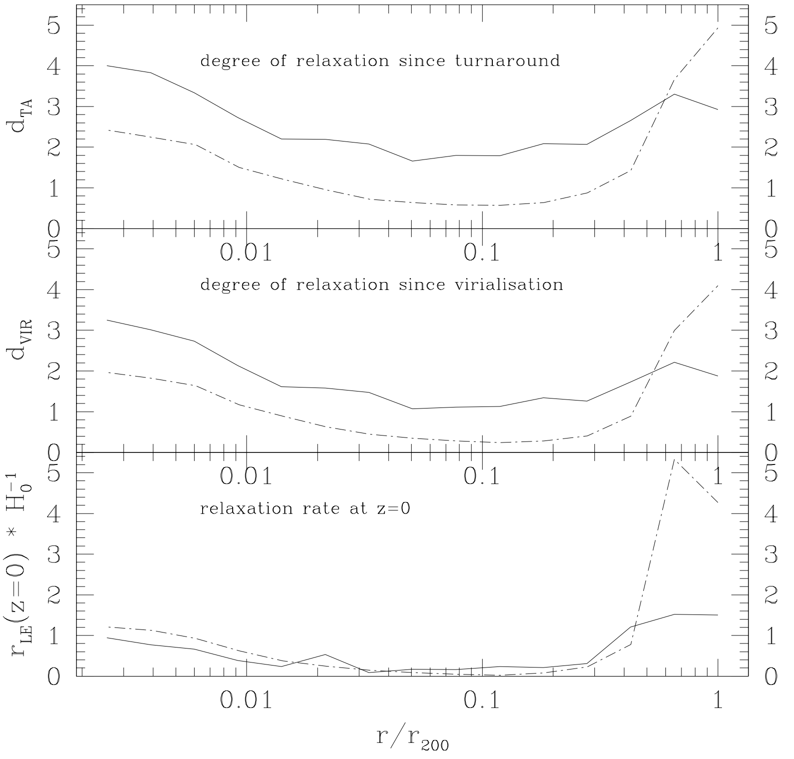

Figure 2.12: Relaxation vs. radius. The solid line is the cluster run C3 ($N_{vir} \simeq 650'000$), the dot - dashed line for the galaxy ($N_{vir} \simeq 250'000$).

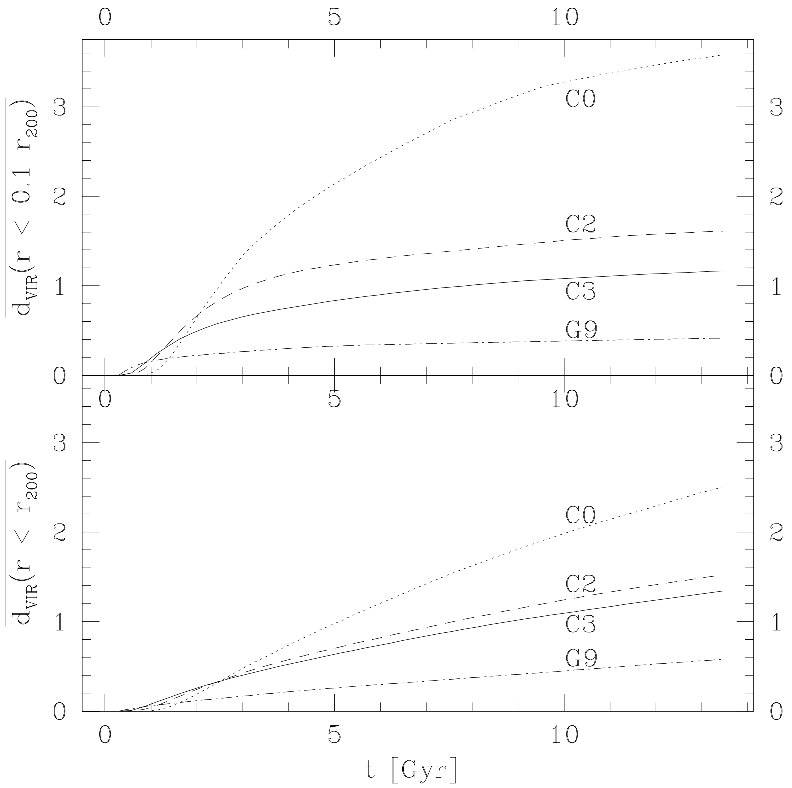

Figure 2.13: The degree of relaxation, $d_{\rm VIR}$, averaged over all particles as a function of time. In the top panel we average over particles inside $0.1\,r_{200}$ at $z = 0$ and in the bottom panel over all inside r_{200}.

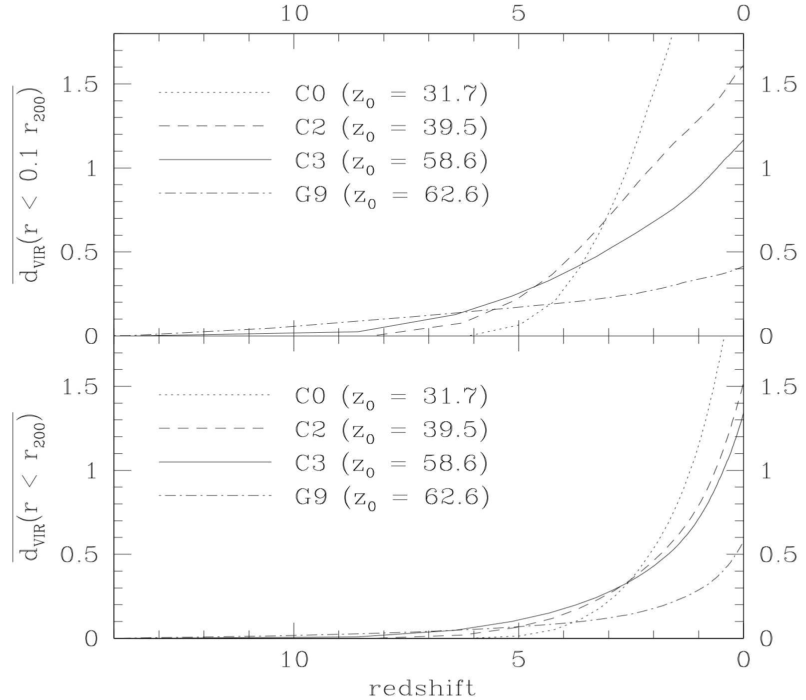

Figure 2.14: Same as Figure 2.13 but as a function of redshift. z_0 is the starting redshift of the runs.

2.6 Conclusions and discussion

N-body cosmological simulations attempt to model a collisionless system of particles using a technique that is inherently collisional on small scales. We have examined the relaxation rates of isolated equilibrium cuspy haloes as a function of particle number, radius and softening parameter. Our results apply primarily to n-body, P^3M codes, such as direct or treecodes. Adaptive grid based methods, such as ART (Kravtsov, Klypin & Khokhlov, 1997) and MLAPM (Knebe, Green & Binney, 2001) also seem to suffer from relaxation but at slightly lower rates than from those quantified here (Binney & Knebe, 2002).

We show how one can define a local relaxation timescale for each particle by measuring its local phase space density which we applied to cosmological simulations in an attempt to determine the regions most affected by numerical relaxation. We summarise our results here:

1. The relaxation rates in cuspy dark matter haloes are in good agreement with the rates predicted by the orbit averaged Fokker-Planck equation. However the average relaxation time is an order of magnitude less than that measured at the half mass radius.

2. We verify that the average relaxation time of a halo is proportional to the number of particles it contains and to the inverse natural logarithm of the softening parameter.

3. The relaxation time is proportional to the local phase space density which allows us to measure the cumulative amount of relaxation each particle undergoes during the evolution of a halo.

4. We show that we can measure the relaxation rate in collapsing or non-equilibrium haloes that have kinetic to potential energy ratios up to ten times smaller than the equilibrium value.

5. Averaging over several simulations of cuspy Hernquist haloes we show that within few mean relaxation times the central cusp is transformed into a constant density core.

6. We show that the hierarchical build up of galaxy or cluster mass haloes leads to a greatly enhanced degree of relaxation within their central regions. The substructure haloes suffer from the highest rates of relaxation since they contain the fewest particles for the longest period of time. Subhaloes are typically several relaxation times old therefore one should be cautious about interpreting their internal structure using simulations of order 10^6 particles (Stoehr et. al, 2002).

7. Cluster haloes suffer three times the amount of relaxation as galaxy haloes simulated at the same relative spatial and mass resolution. This is because the cluster forms later and more of its particles spend time in poorly resolved progenitors.

8. Increasing the resolution (N) at a fixed force softening reduces the the accumulated amount of relaxation. The average degree of relaxation in CDM haloes at $z = 0$ scales $\propto N^{-0.2}$, in the inner 10 percent $\propto N^{-0.3}$. Relaxation may therefore provide a simple explanation for the slow convergence (resolved radius $\propto N^{-1/3}$) in density profiles of CDM haloes simulated at different resolutions (Moore et al. 1998; Ghigna et al. 2000).

9. Most of the affected particles become "relaxed" very early and within the first few Gyrs of the evolution of the Universe. This is hardest epoch to accurately resolve in a cosmological simulation since the relative force errors can be large and the densities of forming haloes can be very high.

The high degrees relaxation show that at $z = 0$ many particles have completely different energies and orbits compared to their evolution in the mean field limit ($N \rightarrow \infty$). Current cosmological simulations cannot model all the subtle dynamics like orbital resonances which can be important e.g. during tidal stripping (Weinberg, 1998). But does relaxation also affect the coarse structure of the object, e.g. their density profiles? It is unclear as to how one should interpret these results for the following reason. The highest rates of relaxation are accumulated early during the formation of the haloes. Once a subhalo falls into a larger system the particles achieve a higher energy and it is not clear that one should accumulate the relaxation timescale in the way that we have done since the final "hot" system may lose the memory of the initial conditions through violent relaxation processes. Indeed, Moore et al. (1999b) show that the initial conditions play little role in determine the final gross structure of dark matter haloes.

The technique of accumulating the relaxation times by measuring the local phase density works very well for near equilibrium structures. In some instances, the energies of particles in a cosmological simulation will increase due to the mass increase from merging. From the virial theorem the growth in mass must be accompanied by an increase in velocity dispersion. Thus it is not clear how relaxation at a high redshift propagates to the final time. However we are mainly interested in the structure of the central dark matter halo and the substructure haloes. These are the regions where most effort is going into comparing theoretical predictions with observational data (e.g. Moore 1994; Stoehr et. al 2002).

The velocity dispersion in the substructure haloes actually decreases slowly with time as mass is stripped. On the other hand the velocity dispersion of the central halo increases with time as it grows by merging. We can quantify the decrease in the mean velocity dispersion in subhaloes or the central halo region by extrapolating the particles backwards through time to examine the velocity dispersion in the progenitor haloes. For the galaxy cluster, half of the relaxation is accumulated since $z = 3$. We therefore trace all the particles in the central few percent of the cluster back to $z = 4$ where we find that all the particles lie in the most massive collapsed haloes at that time – the most massive structures at high redshift form the central cluster region through natural biasing. We find that for the central cluster particles, $\sigma(z = 4)/\sigma(z = 0) = 1.6$, i.e. the mean dispersion only increases by 60%. Similarly for cluster substructure haloes, the ratio is practically constant through time. For this reason we are confident that the accumulated degrees of relaxation are a good indicator of the true relaxation of the interesting regions within the simulations.

We note that the following thought experiment illustrates a possible way in which relaxation in the first haloes can affect the central structure of the final halo, even though the energies of the particles may have changed over time: The first haloes to form are several relaxation times old and they achieve this in an near equilibrium state. We have demonstrated that our cumulative estimator works very well for non-equilibrium systems that have P.E./K.E. ratios as large as ten times the equilibrium mean (Figure 5). We also show that these first poorly resolved haloes will develop constant density cores through relaxation (Figure 8). Now consider what happens when this halo accretes into a larger system. Because of the constant density core the satellite will completely disrupt at some distance from the centre of the final object (Moore, Katz & Lake, 1996). If the accreting halo had a steep cusp resolved with more particles then it may sink deeper within the potential and deposit mass at smaller radii (e.g. Barnes 1999, Syer & White 1998). Thus the early relaxation could affect the final density profile even if the relative energies of the particles were initially quite different from their final energies. Unfortunately, quantifying this effect and determining if it is at all important is best achieved by increasing the resolution by several orders of magnitude over the haloes simulated in this paper.

Acknowledgments

We thank Adrian Jenkins and Alexander Knebe for helpful suggestions and comments. We also would like to thank the Swiss supercomputing centre at Manno for computing time where many of these numerical simulations were performed.

Chapter 3

Convergence and scatter of cluster density profiles [1]

3.1 Abstract

We present new results from a series of ΛCDM simulations of cluster mass halos resolved with high force and mass resolution. These results are compared with recently published simulations from groups using various codes including PKDGRAV, ART, TPM, GRAPE and GADGET. Careful resolution tests show that with 25 million particles within the high resolution region we can resolve to about 0.3% of the virial radius and that convergence in radius is proportional to the mean interparticle separation. The density profiles of 26 high resolution clusters obtained with the different codes and from different initial conditions agree very well. The average logarithmic slope at one percent of the virial radius is $\gamma = 1.26$ with a scatter of ± 0.17. Over the entire resolved regions the density profiles are well fitted by a smooth function that asymptotes to a central cusp $\rho \propto r^{-\gamma}$, where we find $\gamma = 1.16 \pm 0.14$ from the mean of the fits to our six highest resolution clusters.

3.2 Introduction

A highly motivated and well defined problem in computational astrophysics is to compute the non-linear structure of dark matter halos. This is especially timely given the abundance of new high resolution data that probe the central structure of galaxies (e.g. de Blok et al. 2001a; de Blok, McGaugh & Rubin 2001b; McGaugh, Rubin & de Blok 2001; Swaters et al. 2003; de Blok & Bosma 2002; Gentile et al. 2004) and clusters (e.g. Sand et al. 2004). Furthermore, a standard cosmological paradigm has been defined that gives a well defined framework within which to perform numerical calculations of structure formation (e.g. Spergel et al. 2003). This subject has developed rapidly over the past few years, building upon the pioneering results obtained in the early 1990's by Dubinski & Carlberg (1991) and Warren et. al (1992). More recently, the systematic study of many halos at a low resolution led to the proposal that the profile of an 'average' cold dark matter halo in dynamical equilibrium could be fit by an universal two parameter function (Navarro, Frenk & White, 1996), with a slope of that asymptotically approaches -1 as $r \rightarrow 0$. At the same time, the study of a few halos at high resolution questioned these results (Fukushige

---

[1] This chapter is accepted for publication in: MNRAS. (Diemand et al., 2004c).

& Makino 1997; Moore et al. 1998; Moore et al. 1999b; Jing & Suto 2000; Ghigna et al. 2000). These latter authors claimed that of the order a million particles within the virialised region where necessary to resolve the halo structure to 1% and the slopes at that radius could be significantly steeper. Just within the last few months, we have seen several groups publish reasonably large samples of halos simulated with the necessary resolution that we can finally determine the scatter in the density profiles across a range of mass scales (Fukushige, Kawai & Makino 2004; Tasitsiomi et al. 2004; Wambsganss, Bode & Ostriker 2004; Hayashi et al. 2003b; Navarro et al. 2004; Reed et. al 2003b).

Much of the recent controversy in the literature has been due to limited statistics and the lack of agreement over what is a reliable radius to trust a given simulation with a given set of parameters. Several studies have attempted to address this issue (Moore et al. 1998; Knebe et al. 2000; Klypin et al. 2001; Power et al. 2003; Diemand et al. 2004a). Integration and force accuracy can be understood using controlled test simulations. However, discreteness is probably the most important and least understood numerical effect that can influence our numerical results which is exacerbated due to the lack of an analytic solution with which to compare simulations. Our particle sampling of the nearly collisionless fluid we attempt to simulate can lead to energy transfer and mass redistribution, particularly in the central regions that we are often most interested in.

Collisional effects in the final object or in the early hierarchy of objects can be reduced by increasing the number of particles N in a simulation (Diemand et al., 2004a). The limitation to the phase space densities that can be resolved due to discreteness in the initial conditions can also be overcome by increasing the resolution (Binney, 2004). As we increase the resolution within a particular non-linear structure, we find that the global properties of the resolved structure is retained, including shape, density profile, substructure mass functions and even the positions of the infalling substructures. This gives us confidence that our N-body calculations are not biased by using finite N (Baertschiger et al., 2002). The fact that increasing the resolution allows us to resolve smaller radii is important since the baryons often probe just the central few percent of a dark matter structure - the latest observations of galaxy and clusters probe the mass distribution within one percent of the virial radius, which until recently was unresolved by numerical simulations. Forthcoming experiments, such as VERITAS (Weekes et. al, 2002) and MAGIC (Flix, Martinez & Prada, 2004) will probe the structure of dark matter halos on even smaller scales by attempting to detect gamma-rays from dark matter annihilation within the central hundred parsecs ($\sim 0.1\% R_{virial}$) of the Galactic halo (e.g. Calcaneo-Roldan & Moore 2000). These scales are still below the resolution limit of todays cosmological simulations, the estimates of the dark matter densities in these regions are still based on extrapolations which introduce large uncertainties

A simple estimate of the scaling of N with time shows remarkable progress over and above that predicted by Moore's law. The first computer simulations used of the order 10^2 particles and force resolution of the order of the half mass radii (Peebles, 1970). Today we can follow up to 10^8 particles with a resolution of 10^{-3} of the final structure. The increase in resolution is significantly faster than predicted by Moore's law since equally impressive gains in performance have been due to advances in software.

We are finally at the stage whereaby the dark matter clustering is understood at a level where the uncertainties are dominated by the influence of the baryonic component. It is therefore a good time to review and compare existing results from different groups together with a set of new simulations that we have carried out that are the state of the art in this

Table 3.1: Parameters of simulated cluster halos

Run	z_i	ϵ_0 [kpc]	$\epsilon_{\rm max}$ [kpc]	$N_{\rm vir}$	$M_{\rm vir}$ $10^{15}[{\rm M}_\odot]$	$r_{\rm vir}$ [kpc]	$Vc_{\rm max}$ [km s^{-1}]	$r_{\rm max}$ [kpc]	$r_{\rm resolved}$ [kpc]
$A9$	40.27	2.4	24	24’987’606	1.29	2850	1428	1853	9.0
$B9$	40.27	4.8	48	11’400’727	0.59	2166	1120	1321	14.4
$C9$	40.27	2.4	2.4	9’729’082	0.50	2055	1090	904	9.0
$D3h$	29.44	1.8	18	205’061	0.28	1704	944	834	27
$D6h$	36.13	1.8	18	1’756’313	0.31	1743	975	784	13.5
$D6$	36.13	3.6	36	1’776’849	0.31	1749	981	840	13.5
$D9$	40.27	2.4	24	6’046’638	0.31	1752	983	876	9.0
$D9lt$	40.27	2.4	24	6’036’701	0.31	1752	984	841	9.0
$D12$	43.31	1.8	18	14’066’458	0.31	1743	958	645	6.8
$E9$	40.27	2.4	24	5’005’907	0.26	1647	891	889	9.0
$F9$	40.27	2.4	24	4’567’075	0.24	1598	897	655	9.0
$F9cm$	40.27	2.4	2.4	4’566’800	0.24	1598	898	655	9.0
$F9ft$	40.27	2.4	99.06	4’593’407	0.24	1601	905	464	9.0

subject and represent what is achievable with several months of dedicated supercomputer time. For certain problems, such as predicting the annihilation flux discussed earlier, it would be necessary to significantly increase the resolution. This is not possible with existing resources and new techniques should be explored. We begin by presenting our new simulations in Section 2. Section 3 discusses convergence tests and the asymptotic best fit density profiles. In Section 4 we compare our results with recently published results from four other groups mentioned above.

3.3 Numerical experiments

Table 3.1 gives an overview of the simulations we present in this paper. With up to 25×10^6 particles inside the virial radius of a cluster and an effective 10^5 timesteps, they are among the highest resolution ΛCDM simulations performed so far. They represent a major investment of computing time, the largest run was completed in about 10^5 CPU hours on the zBox supercomputer [1].

3.3.1 N-body code and numerical parameters

The simulations have been performed using a new version of PKDGRAV, written by Joachim Stadel and Thomas Quinn (Stadel, 2001). The code was optimised to reduce the computational cost of the very high resolution runs we present in this paper. We tested the new version of the code by rerunning the “Virgo cluster” initial conditions (Moore et al., 1998). We confirmed that density profile, shape of the cluster and the amount of substructure it contains is identical to that obtained with the original code presented in Ghigna et al. (1998).

---

[1] http://www-theorie.physik.unizh.ch/~stadel/zBox/

Individual time steps are chosen for each particle proportional to the square root of the softening length over the acceleration, $\Delta t_i = \eta\sqrt{\epsilon/a_i}$. We use $\eta = 0.2$ for most runs, only in run $D9lt$ we used larger timesteps $\eta = 0.3$ for comparison. The node-opening angle is set to $\theta = 0.55$ initially, and after $z = 2$ to $\theta = 0.7$. This allows higher force accuracy when the mass distribution is nearly smooth and the relative force errors can be large in the treecode. Cell moments are expanded to fourth order in PKDGRAV, other treecodes typically use just second or first order expansion. The code uses a spline softening length ϵ, forces are completely Newtonian at 2ϵ. In Table 3.1 ϵ_0 is the softening length at $z = 0$, ϵ_{max} is the maximal softening in comoving coordinates. In most runs the softening is constant in physical coordinates from $z = 9$ to the present and is constant in comoving coordinates before, i.e. $\epsilon_{\rm max} = 10\epsilon_0$. In runs $C9$ and $F9cm$ the softening is constant in comoving coordinates for the entire run, in run $F9ft$ the softening has a constant physical length for the entire run.

3.3.2 Initial conditions and cosmological parameters

We adopt a ΛCDM cosmological model with parameters from the first year WMAP results: $\Omega_\Lambda = 0.732$, $\Omega_m = 0.268$, $\sigma_8 = 0.9$, $h = 0.71$, (Spergel et al., 2003). The initial conditions are generated with the GRAFIC2 package (Bertschinger, 2001). The starting redshifts z_i are set to the time when the standard deviation of the density fluctuations in the refined region reaches 0.2.

First we run a parent simulation: a 300^3 particle cubic grid with a comoving cube size of 300 Mpc (particle mass $m_{\rm p} = 3.7 \times 10^{10}{\rm M}_\odot$, force resolution $\epsilon_0 = 100kpc$, $\epsilon_{\rm max} = 1Mpc$). Then we use the friends-of-friends (FoF) algorithm (Davis et al., 1985) with a linking length of 0.164 mean interparticle separations to identify clusters. We found 39 objects with virial masses above $2.3 \times 10^{14}{\rm M}_\odot$. We selected six of these clusters for resimulation, discarding objects close to the periodic boundaries and objects that show clear signs of recent major mergers at $z = 0$. We label the six cluster with letters A to F according to their mass. It turned out that two of the clusters selected in this way (runs A and C) have ongoing major mergers at $z = 0$ (i.e. two clearly distinguishable central cores), which is not evident from the parent simulation due to lack of resolution. These clusters were evolved slightly into the future to obtain a sample of six 'relaxed' clusters.

For re-simulation we mark and trace back the particles within a cluster's virial radius to the initial conditions. All particles which lie within a 4 Mpc (comoving) thick region surrounding the marked particles in the initial conditions are also added to the refinement region. This ensures that there is no pollution of heavier particles within the virial radius of the resimulated cluster. Typically one third or one quarter of the refinement particles ends up within the virial radius. To reduce the mass differences at the border of the refinement region we define a 5 Mpc thick 'buffer region' around the high resolution region, there an intermediate refinement factor of 3 or 4 in length is used. The final refinement factors are 6, 9 and 12 in length, i.e., 216, 729 and 1728 in mass, so that the mass resolution is $m_{\rm p} = 2.14 \times 10^7{\rm M}_\odot$ in the highest resolution run. We label each run with a letter indicating the object and number that gives the refinement factor in length. To reduce the mass differences at the border of the refinement region we define a 5 Mpc thick 'buffer region' around the high resolution region, there an intermediate refinement factor of 3 or 4 in length is used.

3.3.3 Measuring density profiles

We define the virial radius $r_{\rm vir}$ such that the mean density within $r_{\rm vir}$ is $178\Omega_M^{0.45}\rho_{\rm crit} = 98.4\rho_{\rm crit}$ for the adopted model (Eke, Cole & Frenk, 1996). We use 30 spherical bins of equal logarithmic width, centered on the densest region of each cluster using TIPSY [2]. We confirmed that using triaxial bins adapted to the shape of the isodensity surfaces (at some given radius, we tried 0.1, 0.5 and $1r_{\rm vir}$) does not change the form of the density profile, in agreement with Jing & Suto (2002). For simplicity and easier comparison to other results we will present only profiles obtained using spherical bins. Data points are plotted at the arithmetic mean of the corresponding bin boundaries; the first bin ends at 1.5 kpc, the last bin at the virial radius.

3.4 Lambda CDM cluster profiles

3.4.1 Profile convergence tests

Numerical convergence tests show that with sufficient timesteps, force accuracy and force resolution the radius a CDM simulation can resolve is limited by the mass resolution (Moore et al. 1998; Ghigna et al. 2000; Knebe et al. 2000; Klypin et al. 2001; Power et al. 2003; Hayashi et al. 2003b; Fukushige et al. 2004; Reed et. al 2003b). These tests compare different mass resolution simulations of the same object to determine the resolved radius. The resulting radii scale with $N^{-0.45}$ according to Power et al. (2003), Hayashi et al. (2003b) and Fukushige et al. (2004), but only with $N^{-1/3}$ in the tests in Moore et al. (1998),Ghigna et al. (2000) and Reed et. al (2003b).

3.4.1.1 Mass resolution

The finite mass resolution of N body simulations always leads to two body relaxation effects, i.e. heat is transported into the cold halo cores and they expand. It is not obvious that better mass resolution reduces the effects of two body relaxation, since in hierarchical models the first resolved objects always contain just a few particles and with higher resolution these first objects form earlier, i.e. they are denser and more affected by relaxation effects (Moore et al. 2001; Binney & Knebe 2002). Estimates of relaxation based on following the local phase-space density in simulations show that the amount of relaxation can be reduced with better mass resolution, but the average degree of relaxation scales roughly like $N^{-0.3}$ much slower than N^{-1} expected from the relaxation time of the final structure (Diemand et al., 2004a). This confirms the validity of performing convergence tests in N, but one has to bear in mind that convergence can be quite slow.

We checked a series of resimulations of the same cluster (D) for convergence in circular velocity, mass enclosed [3] and density. Outside of the converged radii the values must be within 10% of the reference run D12. Table 3.2 shows the measured converged radii.

1. Convergence is slow, roughly $\propto N^{-1/3}$. Therefore a high resolution reference run should have at least 8 times as many particles. Between run D9 and D12 the factor

---

[2] TIPSY is available form the University of Washington N-body group: http://www-hpcc.astro.washington.edu/tools/tipsy/tipsy.html

[3] Convergence within 10% in cumulative mass is the same as convergence in circular velocity with a tolerance of 5%

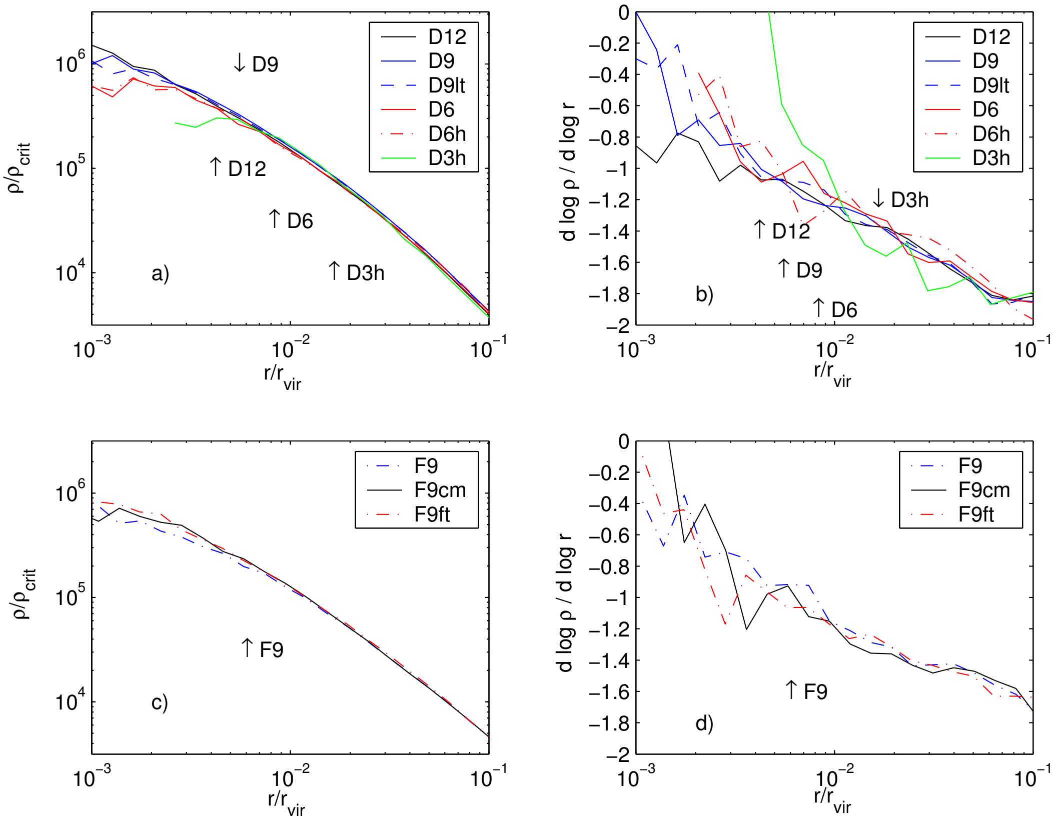

Figure 3.1: Numerical convergence tests for the cluster profiles: Panel (a): Density profiles of cluster D resolved with $N_{\mathrm{vir}} = 205k, 1.8M, 6M$ and $14M$ particles. Panel (b): Logarithmic slope for the profiles from (a). Panel (c): Density profiles of cluster F simulated with different numerical parameters: $F9ft$ used 4096 fixed timesteps and constant ϵ in physical coordinates as in Fukushige et al. (2004). $F9cm$ and $F9$ used adaptive timesteps $0.2\sqrt{\epsilon(z)/a}$ with comoving softening in $F9$ and mixed comoving/physical softening in $F9$ ($\epsilon_{\max} = 10\epsilon_0$). Panel (d): Logarithmic slope for the profiles from (c).

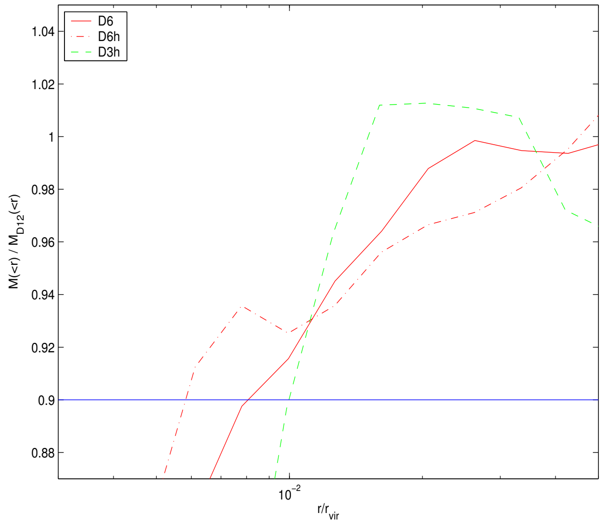

Figure 3.2: Ratios of the mass enclosed in low resolution runs to mass enclosed in the high resolution run $D12$. By comparing runs with equal softening (smaller than one third of the convergence scale) like $D3h$ and $D6h$ one finds that the resolved radii scale like $r \propto N^{-1/3}$. A larger softening (see run $D6$) can increase the converged scales and change this scaling.

Table 3.2: Convergence radii measured by comparing with run $D12$. The numbers in the run labels are $\propto N^{1/3}$, at fixed force resolution we get $r \propto N^{-1/3}$ (bold values). Question marks indicate that a run with much better mass resolution than $D12$ would be needed to measure this convergence radii reliably. Stars indicate estimated radii assuming a convergence rate of $r \propto N^{-1/3}$.

Run	ϵ_0 [kpc]	$N_{\rm vir}$	$r_{10\%\rm vc}$ [kpc]	$r_{10\%\rm M}$ [kpc]	$r_{10\%\rho}$ [kpc]
$D3h$	1.8	205'061	**17.2**	**21.9**	**9.5**
$D6h$	1.8	1'756'313	**8.4**	**10.7**	**4.6**
$D6$	3.6	1'776'849	8.4	17.3	12.1
$D9$	2.4	6'046'638	3.2 ?	5.2 ?	2.2 ?
$D9lt$	2.4	6'036'701	5.2 ?	6.6 ?	2.8 ?
$D9$	2.4	6'046'638	5.7 *	7.3 *	3.2 *
$D12$	1.8	14'066'458	4.2 *	5.3 *	2.4 *

is only 2.37. Using D12 to determine the converged radii of D9 gives radii that are about a factor two too small (Table 3.2). Fukushige et al. (2004) compare runs with $N_{\mathrm{vir}} = 14 \times 10^6$ and $N_{\mathrm{vir}} = 29 \times 10^6$. At radii where both runs have similar densities it is still not clear if the simulations have converged, even higher resolution studies are needed to demonstrate this.

2. If one sets the force resolution to one half of expected resolved radius, then it is not surprising to measure a resolved radius close to the expected value. With this method one can demonstrate almost arbitrary convergence criteria, as long as they overestimate r_{conv}. Therefore convergence tests in N should be performed with small softenings (high force resolution). Runs D3h, D6h and D12 all have $\epsilon_0 = 1.8$ kpc, their converged radii scale like the mean interparticle separation $N^{-1/3}$. In run D6 $\epsilon_0 = 3.2$ kpc is close to the 'optimal value' from Power et al. (2003), and the converged radii are larger than in D6h (see Figure 3.2).

3. Different small scale noise in the initial conditions leads to different formation histories. Therefore the shape and the density profile can differ even at radii were all runs have converged. For example between r=10 kpc and 320 kpc the densities in run D9 are about 7% higher than in run D12. Therefore the densities in D9 are within 10% from those of D12 quite early. If one rescales ρ in this range $r_{10\%\rho}$ of D9 grows from 2.2 kpc to 4.6 kpc.

Extrapolating $r_{\mathrm{conv}} \propto N^{-1/3}$ to our highest resolution runs gives the values on the last two lines of Table 3.2. Note that this is just an extrapolation, it is not clear that this scaling is valid down to this level, only larger simulations could verify this. To be conservative we assume the limit due to mass resolution to be 9 kpc for the '9-series' of runs, and 6.8 kpc for run D12. The force resolution sets another limit at about $3\epsilon_0$ (Moore et al. 1998, Ghigna et al. 2000). We give the larger of the two limits as the trusted radius in Table 3.1.

3.4.1.2 Force and time resolution

Finite timesteps and force resolution also sets a limiting radius/density that a run can resolve. We use multistepping, individual timesteps for the particles that are obtained by dividing the main timestep (usually $t_0/200$) by two until it is smaller than $\eta\sqrt{\epsilon(z)/a}$, where a is the local acceleration. Our standard choice is $\eta = 0.2$ and $\epsilon(z = 0)$ between $0.001 r_{\mathrm{vir}}$ and $0.0022 r_{\mathrm{vir}}$, which is chosen to be less than one third of the resolution limit expected from the finite mass resolution. ϵ is constant in physical length units since $z = 9$ and comoving before that epoch. Here we argue that the resolution limit imposed by this choice of multistepping lie well below the scale affected by finite mass resolution.

In run $D9lt$ the number of timesteps was reduced by using $\eta = 0.3$, at equal force resolution as in $D9$. Run $F9cm$ had a constant comoving softening during the entire simulation, in run $F9ft$ the softening is physical and the timesteps are fixed $\Delta t = t_0/4096$ and equal for all particles (i.e. the same numerical parameters as in Fukushige et al. (2004)). The density profiles are very similar (Figure 3.1, Panel c), there is no significant difference above the mass resolution scale of 9 kpc. There is a small difference in the inner profile of $F9$ compared to $F9ft$ and $F9cm$, at large z this run has larger ϵ and therefore larger timesteps than $F9cm$. So it is possible that runs with our standard parameters have

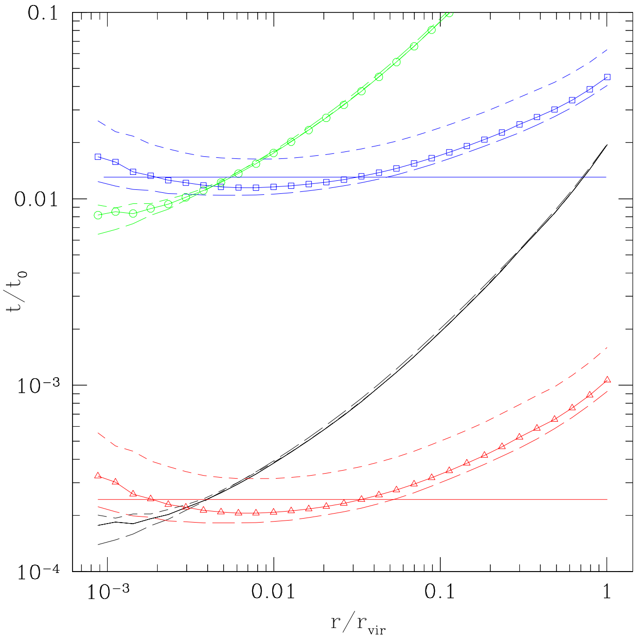

Figure 3.3: The triangles show the timestep criterium $\eta\sqrt{\epsilon(z)/a}$ as a function of radius for run $D9$ at $z = 0$. The dashed line is for run $D9lt$, which has $\eta = 0.3$, and the long dashed line for run $D12$. The open squares give $15(\Delta t/t_0)^{5/6} t_{\mathrm{circ}}(r_{vir})$ form Power et al. (2003), the circles are the circular orbit timescale $2\pi r/v_{\mathrm{circ}}(r)$. Lines without symbols show $t_{\mathrm{dyn}}/15 = 1/(\sqrt{G\rho(<r)}15)$. The two horizontal lines are the timesteps and $15(\Delta t/t_0)^{5/6} t_{\mathrm{circ}}(r_{vir})$ for run $F9ft$.

slightly shallower density profiles at the resolution limit than runs with entirely comoving softening, or runs with a sufficiently large number of fixed timesteps. However run $F9cm$ takes twice as much CPU time as run $F9$ and run $F9ft$ three times more, therefore we accept this compromise.

Figure 3.3 shows the timestep criterion $\eta\sqrt{\epsilon(z)/a}$ as a function of radius at $z = 0$ for runs $D9$ (triangles, solid line), $D9lt$ (dashed) $D12$ (long dashed) and for $F9ft$ (horizontal line). Particles near the cluster centre must take timesteps below $2 \times 10^{-4} t_0$, i.e. their timesteps are $t_0/200 \times 2^{-5} = t_0/6400$. According to Power et al. (2003) the resolution limit due to finite timesteps t_{ts} is where the circular velocity (circles) equals $15(\Delta t/t_0)^{5/6} t_{\mathrm{circ}}(r_{vir})$ (open squares). This radius is indeed close to that where the circular velocities and densities start to differ, however for run $D9lt$ this estimate is even a bit too conservative, since the density (and also v_{circ}) profiles of $D9lt$ and $D9$ agree down to at least $0.005 r_{\mathrm{vir}}$. This suggest that about 15 timesteps per local dynamical time are sufficient for the simulations presented here. Note that this is probably not a general condition for all cosmological simulations: Other codes seem to require different convergence conditions than those we present in this paper. For example, Fukushige et al. (2004) found that their runs converge down to $0.003 r_{\mathrm{vir}}$ even with only 2048 fixed timesteps, which corresponds to only eight timesteps per dynamical time at this radius.

Table 3.3: Density profile parameters. Δ is the root mean square of $(\rho - \rho_{\rm fit})/\rho$ for the four fitting functions used.

Run	$c_{\rm NFW}$	$\Delta_{\rm NFW}$	$c_{\rm M99}$	$\Delta_{\rm M99}$	$\gamma_{\rm G}$	$c_{\rm G}$	$\Delta_{\rm G}$	$\alpha_{\rm N}$	$c_{\rm N}$	$\Delta_{\rm N}$
$A9$	5.7	0.10	1.7	0.21	1.16	3.9	0.057	0.167	4.2	0.033
$B9$	4.2	0.16	1.5	0.13	1.29	2.1	0.083	0.141	2.6	0.093
$C9$	7.6	0.09	3.0	0.26	0.92	8.7	0.081	0.247	7.2	0.068
$D3h$	7.4	0.17	3.9	0.13	1.42	4.0	0.103	0.175	7.3	0.101
$D6h$	7.9	0.11	3.8	0.13	1.17	4.6	0.089	0.206	7.2	0.081
$D6$	7.9	0.12	3.8	0.16	1.25	5.4	0.101	0.193	7.2	0.097
$D9$	8.8	0.12	3.9	0.12	1.21	6.2	0.096	0.190	7.8	0.087
$D9lt$	8.7	0.12	3.8	0.12	1.20	6.2	0.098	0.191	7.7	0.087
$D12$	8.4	0.12	3.1	0.14	1.25	4.5	0.066	0.174	6.9	0.051
$E9$	7.4	0.12	3.0	0.10	1.25	4.5	0.072	0.176	6.2	0.069
$F9$	6.9	0.06	3.0	0.14	1.02	6.7	0.054	0.224	6.5	0.048
$F9cm$	7.3	0.06	3.1	0.14	1.10	6.2	0.055	0.212	6.6	0.057
$F9ft$	7.2	0.05	3.1	0.16	1.05	6.6	0.043	0.218	6.5	0.045

3.4.2 Density profiles

In this section we present the profiles of the six high resolution runs: $A9$,$B9$,$C9$,$D12$,$E9$,$F9cm$. The output at $z = 0$ was used, except for clusters $A9$ and $C9$ which had a recent major merger [4] and the core of the infalling cluster is at about $0.02r_{\rm vir}$ in $A9$ and at $0.1r_{\rm vir}$ in $C9$. These cores spiral in due to dynamical friction and in the 'near' future both clusters have a regular, 'relaxed' central region again. Therefore we use outputs at $z = -0.137$ (+2.1 Gyr) for run $A9$ and $z = -0.167$ (+2.6 Gyr) for $C9$.

3.4.3 Two parameter fits

Figure 3.4 shows the density profiles of the six different clusters. We also show best fits to functions previously proposed in the literature that have asymptotic central slopes of -1 (Navarro, Frenk & White 1996;NFW) and -1.5 (Moore et al. 1999b;M99). The fits are carried out over the resolved region by minimising the mean square of the relative density differences. These two profiles have two free parameters, namely the scale radius r_s and the density at this radius $\rho_s = \rho(r_s)$. The scale radii r_s of these best fits give the concentrations $c = r_{\rm vir}/r_s$ listed in Table 3.3. The residuals are plotted in the top and bottom panels of Figure 3.4 and the rms of the residual are given in Table 3.3 as $\Delta_{\rm NFW}$ and $\Delta_{\rm M99}$. The residuals are quite large and show that neither profile is a good fit to all the simulations which lie somewhere in between these two extremes.

---

[4] An mpeg movie of the formation of cluster $C9$ can be downloaded from http://www-theorie.physik.unizh.ch/~diemand/clusters/

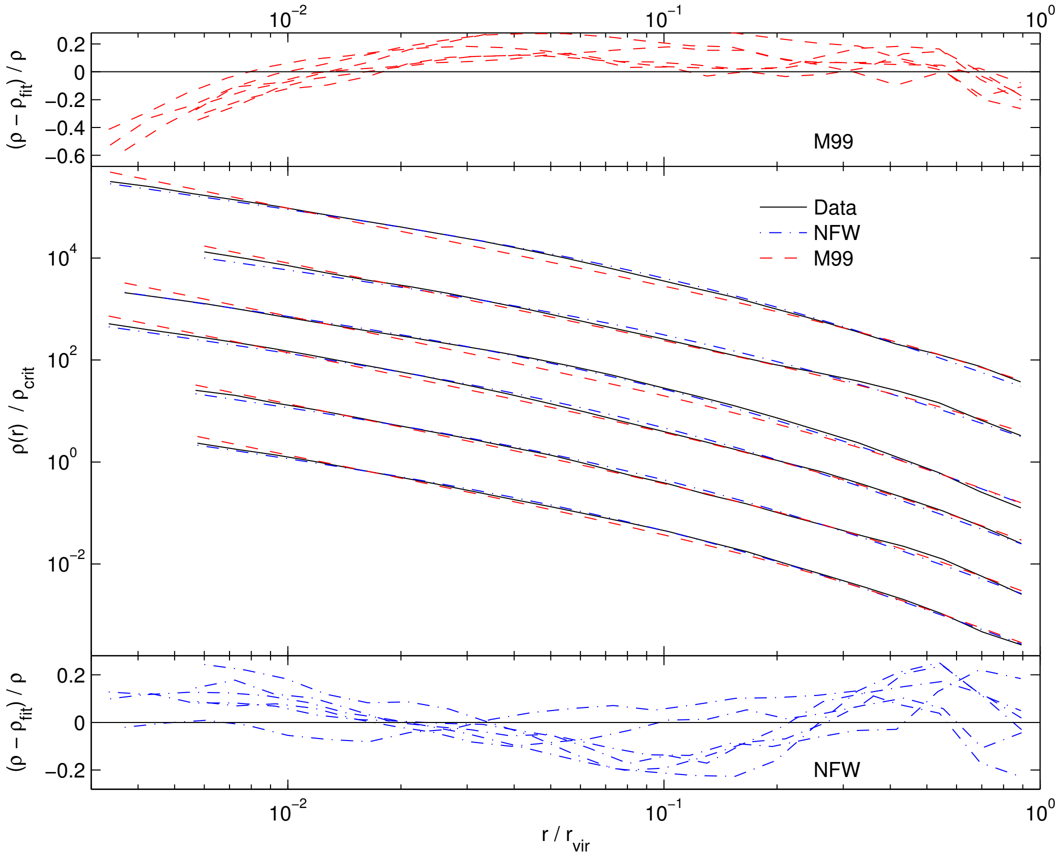

Figure 3.4: Density profiles of the six clusters in our sample, clusters B to F are shifted downwards for clarity. Clusters are ordered by mass form top to bottom. Profiles of cluster A and C are shown at redshifts -0.14 and -0.17, i.e. when they have reached a 'relaxed' state with one well defined centre. Best fit NFW and M99 profiles and residual are shown, obtained by minimising the squares of the relative density differences.

3.4.4 Three parameter fits

Navarro et al. (2004) argue the large residuals of NFW and M99 fits are evidence against any constant asymptotic central slope and propose a profile which curves smoothly over to a constant density at very small radii:

$$\ln(\rho_{\mathrm{N}}(r)/\rho_s) = (-2/\alpha_{\mathrm{N}})\,[(r/r_s)^{\alpha_{\mathrm{N}}} - 1] \tag{3.1}$$

This function gives a much better fit to the simulations, see the dashed dotted lines in Figure 3.5, but this should be expected since there is an additional third free parameter α_{N}, while the NFW and M99 profiles only have two free parameters. α_{N} determines how fast the profile (3.1) turns away from an power law near the centre. Navarro et al. (2004) found that α_{N} is independent of halo mass and $\alpha_{\mathrm{N}} = 0.172 \pm 0.032$ for all their simulations, including galaxies and dwarfs. The mean and scatter of our six high resolution clusters is $\alpha_{\mathrm{N}} = 0.186 \pm 0.037$. (Excluding cluster $C9$ yields $\alpha_{\mathrm{N}} = 0.174 \pm 0.025$).

We also show fits to a general $\alpha\beta\gamma$-profile (Zhao, 1996) (ρ_{G}, subscript 'G' stands for 'general') that asymptotes to a central cusp $\rho(r) \propto r^{-\gamma}$:

$$\rho_{\mathrm{G}}(r) = \frac{\rho_s}{(r/r_s)^{\gamma}(1 + (r/r_s)^{\alpha})^{(\beta-\gamma)/\alpha}}\,. \tag{3.2}$$

We fix the outer slope $\beta = 3$ and the turnover parameter $\alpha = 1$. For comparison the NFW profile has $(\alpha, \beta, \gamma) = (1, 3, 1)$, the M99 profile has $(\alpha, \beta, \gamma) = (1.5, 3, 1.5)$. We fit the three parameters γ, r_s and ρ_s to the data and find that this cuspy profile also provides a very good fit to the data. The best fit values and rms residual are listed in Table 3 and we find a mean slope of $\gamma = 1.16 \pm 0.14$.

Using a sharper turnover $\alpha = 1.5$ makes the fits slightly worse (the average of Δ_G is about 20 percent larger) and the best fit inner slopes are somewhat steeper $\gamma = 1.31 \pm 0.11$. We also made some attempts with fitting procedures where α or β or both α and β are also free parameters. Like Klypin et al. (2001) we found strong degeneracies, i.e. very different combinations of parameter values can fit a typical density profile equally well. Therefore we only present results from the fits with fixed α and β parameters in this paper.

The fitting functions (3.1) and (3.2) fit the measured density profiles very well over the whole resolved range. Function (3.1) is even a relatively good approximation *below* the resolved scale: For example if one is extremely optimistic about r_{resolved} in run $D6$ and uses $r_{\mathrm{resolved}} = 2.8$ kpc instead of 13.5 kpc one gets $\alpha_{\mathrm{N}} = 0.0203$, $c_{\mathrm{N}} = 7.1$ and $\Delta_{\mathrm{N}} = 0.127$, while the generalised fit is now clearly worse: $\gamma_{\mathrm{G}} = 0.99$, $c_{\mathrm{G}} = 3.6$ and $\Delta_{\mathrm{G}} = 0.216$. Also note that the residuals near r_{resolved} are very small or positive for (3.1), i.e. the measured density is as large as the fitted value. But at r_{resolved} it is possible that the measured density is slightly too low since in this region the numerical limitations start to play a role. If extrapolation beyond the converged radius is necessary it is not clear which profile is a safer choice. We agree with Navarro et al. (2004) that all simple fitting formula have their drawbacks, that direct comparison with simulations should be attempted whenever possible and that much higher resolution simulations are needed to establish (or exclude) that CDM halos have divergent inner density cusps (as predicted in Binney 2004).

3.4.5 Maximum inner slope

The results from the last section suggest that profiles with a central cusp in the range $\gamma = 1.16 \pm 0.14$ provide a good approximation to the inner density profiles of ΛCDM

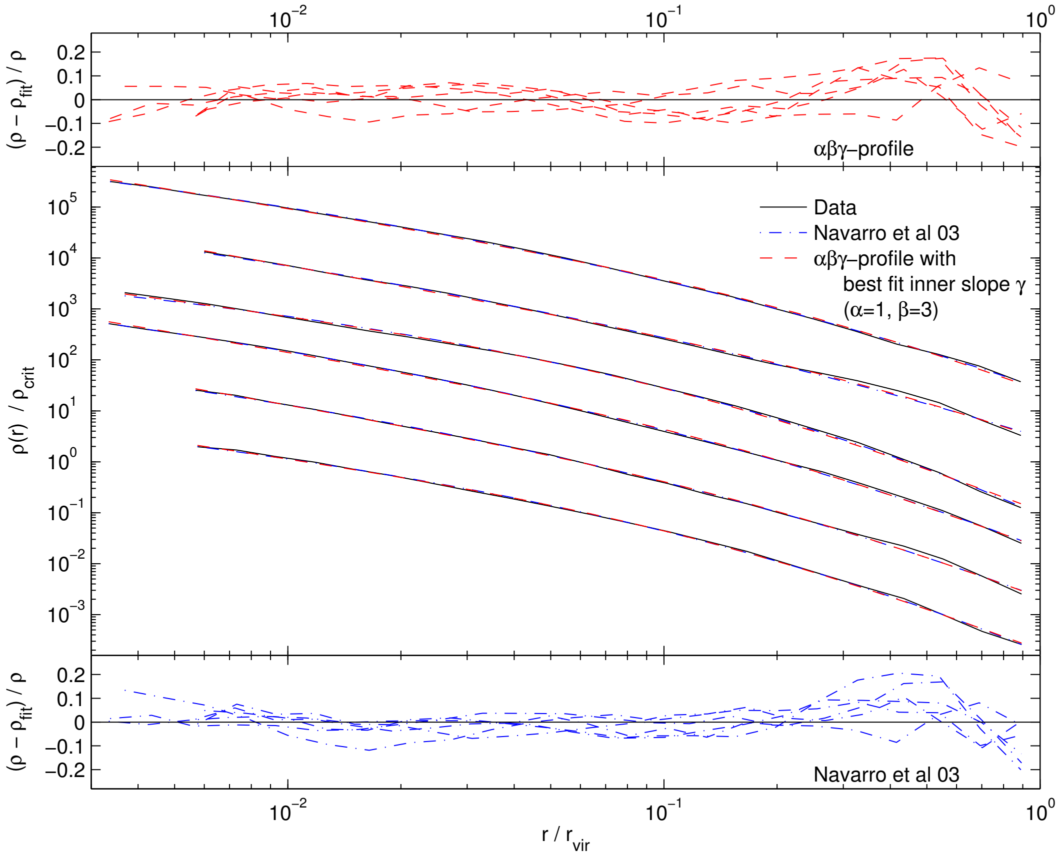

Figure 3.5: Same as Figure 3.4, but with fitting functions that have one additional free parameter. The dashed dotted lines show the profile (3.1) proposed by (Navarro et al., 2004). The dashed lines show a general $\alpha\beta\gamma$-profile (3.2). We fitted the inner slope γ to the data and used fixed values for the outer slope $\beta = 3$ and turning parameter $\alpha = 1$. $\gamma = 1$ corresponds to the NFW profile. The fit parameters and rms of the residuals are given in Table 3.3.

halos. But Figure 4 in Navarro et al. (2004) seems to exclude our mean value for more than half of their cluster profiles. This is not totally inconsistent, but a hint for a mild discrepancy that we will try to explain: In principle the mass inside the converged radius limits the inner slope: $\gamma_{\max} = 3(1 - \rho(r)/\overline{\rho(,r)})$. This is true if both the density and the cumulative density are correct down to the resolved scale. But up to now the central density of a simulated profile always increased with better numerical resolution, so it is likely that also todays highest resolution simulations underestimate the dark matter density near the centre. This means that cumulative quantities like $v_{\rm circ}(r), \overline{M(<r)}$ and $\overline{\rho(<r)}$ tend to be too low even at radii where the density has converged. The converged radii used in Navarro et al. (2004) are close to the radius where the circular velocity is within 10 percent of a higher resolution run, while the density converges further in at about $0.6r_{\rm conv}$ (Hayashi et al., 2003b). If we assume that this is also true for their highest resolution runs then $\overline{\rho(<r)} \propto v_{\rm circ}(r)^2$ is up to 20 percent too low, while the error in $\rho(r)$ is much smaller. This raises the values for $\gamma_{\max}$ by about $0.2 \sim 0.3$ and our mean value $\gamma = 1.16$ is not excluded by any of their clusters anymore. If the convergence with mass resolution is not as fast as $r_{\rm conv} \propto N^{-0.45}$ but rather $r_{\rm conv} \propto N^{-1/3}$, see Section 3.4.1, then the maximum inner slopes could have even larger errors.

3.5 Comparison with other groups

Recently, several groups have published simulations of dark matter clusters in the concordance cosmological model. These authors kindly supplied their density profiles and we show the comparison here. Fukushige et al. (2004)('F03') simulated four ΛCDM clusters with 7 to 26 million particles using a Treecode and the GRAPE hardware. These authors also used the GRAFIC2 software (Bertschinger, 2001) to generate their initial conditions. Hayashi et al. (2003b)('H03') and Navarro et al. (2004) presented eight clusters resolved with up to 1.6 million particles within r_{200} simulated with the GADGET code (Springel et al., 2001a), the method used to generate the initial conditions is described in Power et al. (2003). Tasitsiomi et al. (2004)('T04') simulated six clusters with up to 0.8 million particles within r_{180} using the adaptive refinement tree code ART (Kravtsov et al., 1997) and a technique for setting up multi-mass initial conditions described in Klypin et al. (2001). Wambsganss et al. (2004)('W03') present a cosmological simulation without resimulation of refined regions, i.e. constant mass resolution (1024^3 particles in a 320 h^{-1}Mpc box). The four most massive clusters in this cube are resolved within 0.5 to 0.9 million particles. This simulation was performed with a Tree-Particle-Mesh (TPM) code (Bode & Ostriker, 2003) with a softening of 3.2 h^{-1}kpc.

In Figure 3.6 we show these data along with the new simulations presented in this paper. We plot the density profiles and the logarithmic slopes of the clusters all normalized at the radius such that the circular velocity curve peaks $r_{\rm Vcmax}$ and to $\overline{\rho(<r_{\rm Vcmax})}$. This corresponds to the radius at which $dlog\overline{\rho}/dlogr = -2$. We plot the curves to the “believable” radius stated by each group and down to about 0.01 $r_{\rm vir}$ for W03.

The density profiles are reassuringly similar. Furthermore, the scatter is small, the standard deviation of all profiles is roughly ±0.15 in the logarithmic gradient at small radii ($0.01 - 0.5r_{\rm Vcmax}$). Table 3.4 lists the measured slopes at different radii. There is no value at $3\% r_{\rm Vcmax}$ for the cluster from Tasitsiomi et al. (2004) and Wambsganss et al. (2004) because this is below their quoted resolution limit. Most values agree within the

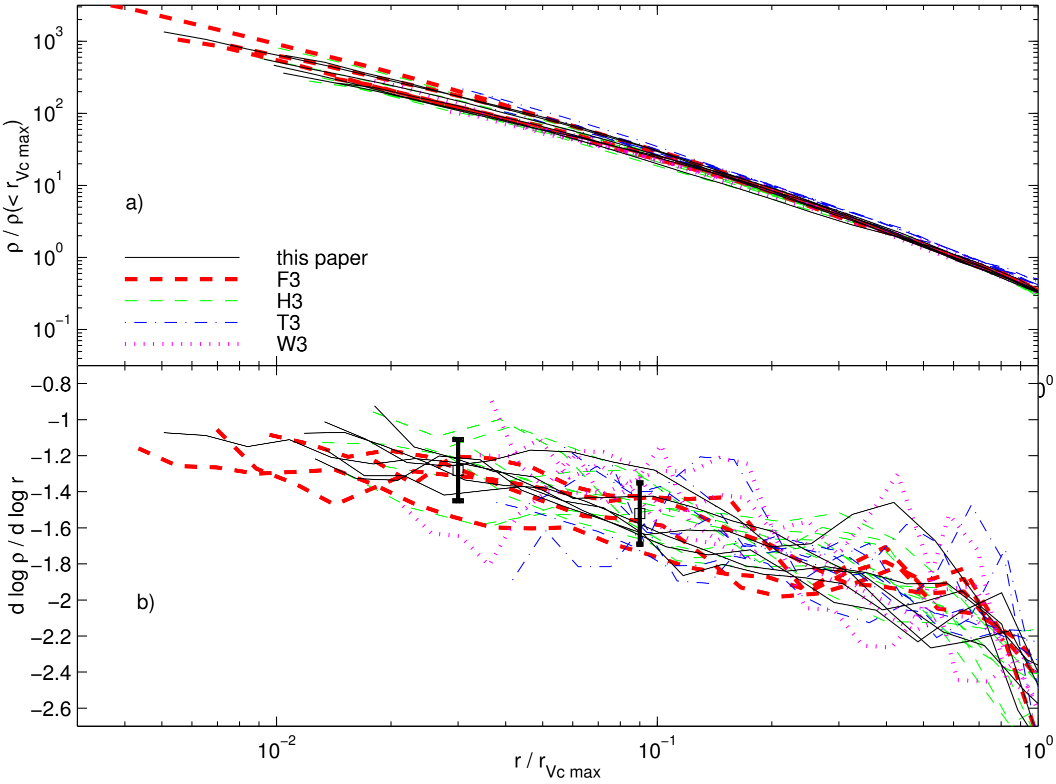

Figure 3.6: Panel (a): Density profiles of cluster simulated by different groups Normalized to the radius were the circular velocity peaks r_{Vcmax} and to $\overline{\rho(< r_{\mathrm{Vcmax}})}$: Six cluster from this paper (solid lines), four from Fukushige et al. (2004) (thick dashed lines), eight from Hayashi et al. (2003b) (thin dashed lines), six from Tasitsiomi et al. (2004) (dashed dotted lines)' four from Wambsganss et al. (2004) (dotted lines). Despite the different codes, parameters and initial conditions used the results are very similar. Panel (b): Logarithmic slope for the profiles from (a). Points with error bars give the averages at 0.03 and 0.09 r_{Vcmax} and a scatter of 0.15 (see Table 3.4).

Table 3.4: Logarithmic slopes (absolute values) of our six high resolution cluster density profiles. Line (a) gives the averages and scatter. (b)-(c) are average slopes from other groups (see text for details).

	$1\% r_{\rm vir}$	$3\% r_{\rm vir}$	$3\% r_{\rm Vcmax}$	$9\% r_{\rm Vcmax}$
$A9$	1.22	1.36	1.24	1.64
$B9$	1.33	1.43	1.21	1.63
$C9$	1.24	1.21	1.25	1.26
$D12$	1.28	1.54	1.32	1.58
$E9$	1.31	1.44	1.41	1.62
$F9cm$	1.19	1.47	1.22	1.43
a) A-F	1.26±0.05	1.41±0.11	1.28±0.08	1.53±0.15
b) F04	1.25±0.05	1.52±0.06	1.33±0.15	1.54±0.15
c) H03	1.18±0.13	1.38±0.14	1.23±0.17	1.50±0.14
d) T04	1.50±0.14	1.79±0.07	–	1.56±0.12
e) W03	1.11±0.04	1.41±0.13	–	1.35±0.06
avg.(a-e)	1.26	1.50	–	1.49
avg.(a-c)	1.23	1.44	1.28	1.52

scatter, the profiles from Tasitsiomi et al. (2004) are steeper when compared at 0.01 and 0.03 $r_{\rm vir} \equiv r_{98.4}$, but within the scatter at $3\% r_{\rm Vcmax}$. This could be due to different halo selection. The majority of their clusters are not isolated but in close pairs or triplets. In a close pair the density falls slower with radius to 98.4 ρ_{crit}, so $r_{\rm vir} \equiv r_{98.4}$ is further out as in a isolated cluster with similar inner profile. Among the samples of isolated clusters (F03; H03; W03 and our clusters) there is a small trend at 0.01 $r_{\rm vir}$ towards steeper slopes with better mass resolution. This could indicate that some numerical flattening of the profiles is still present at 0.01 $r_{\rm vir}$ in the lower resolution clusters.

3.6 Summary

We have carried out a series of six very high resolution calculations of the structure of cluster mass objects in a hierarchical universe. The clusters contain up to 25 million particles and have force softening as small as $0.1\% r_{\rm vir}$.

A convergence analysis demonstrates that for our Treecode with our integration scheme, the radius beyond which we can trust the density profiles scale according to the mean interparticle separation. In the best case we reach a resolution of about $0.3\% r_{\rm vir}$.

Neither of the two parameter functions, the NFW and M99 profiles, are very good fits over the whole resolved range in most clusters. One additional free parameter is needed to fit all six clusters: The asymptotically flat profile from Navarro et al. (2004) and an NFW profile with variable inner slope provide much improved fits. The best fit inner slopes are $\gamma = 1.16 \pm 0.14$. *Below* the resolved radius the two fitting formulas used are very different. Future simulations with much higher resolution will show which one (if either) of the two is still a good approximation on scales of $0.1\% r_{\rm vir}$ and smaller.

We compare our results with simulations from other groups who used independent codes and initial conditions. We find a good agreement between the cluster density profiles calculated with different algorithms. From $0.03 - 0.5 r_{\rm Vcmax}$ the scatter in the profiles is nearly constant and equal to about 0.17 in logarithmic slope. At one percent of the virial radius (defined such that the mean density within $r_{\rm vir}$ is $178\Omega_M^{0.45}\rho_{\rm crit} = 98.4\rho_{\rm crit}$) the slope of the density profiles is 1.26 ± 0.16.

Acknowledgments

We would like to thank the referee for many useful comments and detailed suggestions. We are grateful to Toshiyuki Fukushige, Eric Hayashi, Argyro Tasitsiomi and Paul Bode for providing the density profile data from their cluster simulations. We thank the Swiss Center for Scientific Computing in Manno for computing time to generate the initial conditions for our simulations. All other computations were performed on the zBox supercomputer at the University of Zurich. J. D. is supported by the Swiss National Science Foundation.

Chapter 4

Cusps in the centers of CDM halos

4.1 Abstract

We resolve the inner part of a massive cluster forming in a cosmological ΛCDM simulation with a mass resolution of $2.4 \times 10^6 \mathrm{M}_\odot$. This is about one order of magnitude better than the previous highest resolution ΛCDM simulations of galaxy cluster halos and allows us to probe a dark matter halo density profile down to 0.18 percent of the virial radius. We find that the inner density profile is well fitted by a power-law $\rho \propto r^{-\gamma}$ down to the resolved scale. For the first time an inner region with constant logarithmic slope is resolved, which indicates that cuspy profiles describe the inner profile better than recently proposed profiles with a core. For this cluster the inner slope is about $\gamma = 1.2$, note that the same system has a steepness close to the medium value in a sample of six high resolution cluster simulations of Diemand et al. (2004c).

4.2 Introduction

Recently much effort went into high resolution simulations which have revealed density profiles of cold dark matter halos down to scales well below one percent of the virial radius (Fukushige, Kawai & Makino 2004; Tasitsiomi et al. 2004; Hayashi et al. 2003b; Navarro et al. 2004; Reed et. al 2003b; Diemand et al. 2004c). These halos were resolved by at least several million and up to 25 million particles within the virial radius. But even with these large, computationally expensive simulations the form of the density profile below 0.3 percent of the virial radius remains unclear and there was no clear evidence for a cusp in the center, i.e. no significant inner region with a constant logarithmic slope. Note that galaxy clusters would be the ideal systems to find cusps because of their low concentration. In a galaxy or dwarf halo the inner power law is much harder to resolve because it lies a smaller radius relative to the size of the system.

The existence of a core or a cusp in the center of CDM halos has important observational consequences and is the crucial point in many tests of the CDM theory. Comparisons of dark matter simulations to LSB galaxy rotation curves depend strongly on extrapolations of the simulated profiles towards the center (e.g. Stoehr 2004). The same is true for calculations of the dark matter annihilation signal, there the possible results still spread over a few order of magnitude, depending on how one extrapolates the density profiles from the know, resolved region down to the center (Calcaneo-Roldan & Moore 2000; Stoehr et.

al 2002; Bertone et al. 2004; Prada et al. 2004).

The highest resolutions in cosmological simulations are reached with the widely used refinement procedure (e.g. Bertschinger (2001)): First one runs a cosmological simulation at uniform, low resolution and selects halos for resimulation. Then one generates a new set of initial conditions using the same large scale fluctuations with higher resolution in the selected region. With this technique Navarro, Frenk & White (1996) were able to resolve many halos with a few ten thousand particles and to infer their average density profile which asymptotes to a $\rho(r) \propto r^{-1}$ cusp. Other authors used fitting functions with steeper (-1.5) cusps (Fukushige & Makino 1997; Moore et al. 1998; Moore et al. 1999b; Jing & Suto 2000; Ghigna et al. 2000). Recently a large sample of halos resolved with a million and more particles was simulated (Springel et al. 2001b;Power et al. 2003; Tasitsiomi et al. 2004; Hayashi et al. 2003b; Navarro et al. 2004; Reed et. al 2003b) and the best resolved systems contain up to 25 million particles (Fukushige, Kawai & Makino 2004; Diemand et al. 2004c). But even these very large simulations resolved no inner region with a constant logarithmic slope. (Navarro et al. 2004; Stoehr et. al 2002:Stoehr et. al 2002) introduced cored profiles which seem to fit the data better than the cuspy profiles proposed earlier by Navarro et al. (1996) and Moore et al. (1999b). This better fit was interpreted as indication against cuspy inner profiles. However the cored profiles have one additional parameter and therefore the result that they produce much better fits to the data is not surprising. Diemand et al. (2004c) showed that an NFW like profile with the inner slope as additional free parameter fits the highest resolution profiles just as well as the cored ones. Some theoretical arguments seem to favor cusps (e.g. Binney 2004) but make only vague predictions about their slopes. At the moment higher resolution simulations seem to be the only way to decide the core vs. cusp question.

Here we present a new simulation of one of the galaxy clusters from Diemand et al. (2004c) with one magnitude better mass resolution which gives strong support to cuspy inner profiles. The increase in resolution was made possible by using a multi-mass refinement technique described in Section 4.3. In Section 4.4 we present our results and in Section 4.5 the conclusions.

4.3 Numerical experiments

Table 4.1 gives an overview of the simulations we present in this paper. With a mass resolution corresponding to 130×10^6 particles inside the virial radius of a cluster, DM25 is the highest resolution ΛCDM simulation performed so far and was completed in about 3×10^5 CPU hours on the zBox supercomputer [1]. The convergence radius of run DM25 is 3.3 kpc, estimated using the $r \propto N^{-1/3}$ scaling and the measured converged scales from Diemand et al. (2004c).

4.3.1 Multi mass refinements

The refinement procedure is usually applied to entire virialised systems, i.e. one marks all particles inside the virial radius of the selected halo and traces them back to the initial conditions. Then one refines the region that encloses the positions of the marked particles. Usually the region is further increased to prevent any mixing of low resolution particles

---

[1] http://www-theorie.physik.unizh.ch/~stadel/zBox/

Table 4.1: Parameters of the simulated cluster. At z=0 the viral mass is $3.1 \times 10^{14} \mathrm{M}_\odot$ and the virial radius is 1.75 Mpc. N_{HRP} is the number of high resolution particles and m_{HRP} is the mass of these particles.

Run	z_i	ϵ_0 [kpc]	N_{HRP}	m_{HRP} [$\mathrm{M}_\odot$]	r_{resolved} [kpc]
*D*9	40.27	2.4	31'922'181	5.2×10^7	9.0
*DM*9	40.27	2.4	3'115'017	5.2×10^7	9.0
*D*12	43.31	1.8	14'066'458	2.2×10^7	6.8
*DM*25	52.4	0.84	65'984'375	2.4×10^6	3.3

into the virial radius of the final system. In Diemand et al. (2004c) all particles within 4 comoving Mpc in the initial conditions were added to the high resolution region. This assures that only light particles end up within the virial radius of the final cluster and it also has the advantage that halos in the outskirts of the cluster (out to 2 or 3 virial radii) are still well resolved (Moore et al., 2004). But with this procedure only between one fourth to one third of all the high resolution particles end up in the cluster.

If one is only interested in the inner regions of a halo it is possible to use a new, more efficient way of refinement that we present here: Instead of refining the whole virialised system we only refine the region were the inner particles come form. This allows to reduce the size of the high resolution region considerably, because most of particles that end up near the center of the system start in quite small region, compared to the region that one gets by tracing back all the particles inside the virial radius. Using this technique we were able to reduce the computational cost of a CDM cluster simulation by an oder of magnitude at equal force and mass resolution in the inner region. Of course now one has different mass particles inside the final virialised structure, but in section 4.3.3 we show that the density profiles of such a multi-mass cluster (run DM9) is the same as the one of a fully refined cluster at equal peak resolution (run D9).

In this paper we apply the multi mass refinement to the cluster 'D' from Diemand et al. (2004c). This cluster is well relaxed and isolated at z=0 and it has an average density profile, i. e. its inner slope is close to the mean value. First we mark all particles within one percent of the virial radius in the final halo and trace them back to the initial conditions. Then we add all particles within one comoving Mpc of a marked particle to the set of marked particles, and finally we add all particles on intersections of any two already marked particles. After these two steps there is region with a fairly regular triaxial boundary which contains only marked particles. The number of marked particles grows by almost a factor of 8 during these additions, but it is still more than a factor of two smaller than the number of particles in the final cluster and a factor of ten smaller than the original high resolution volume used in Diemand et al. (2004c). The computational cost with our code and parameters is roughly proportional to the number of high resolution particles, therefore we gain about a factor of ten with this reduction of the high resolution region. Probably one can reduce the high resolution volume further and focus even more of the computational effort into the innermost region, we plan to explore this possibility with future simulations.

4.3.2 Codes and parameters

The simulations have been performed using PKDGRAV, written by Joachim Stadel and Thomas Quinn (Stadel, 2001). We use the same cosmological and numerical parameters as in Diemand et al. (2004c) with a few changes given below and in Table 4.1. We use the GRAFICS2 package (Bertschinger, 2001) to generate the initial conditions. The particle timestep criterium $\Delta t_i < \eta\sqrt{\epsilon/a_i}$, where a_i is the acceleration of particle "i", gives almost constant timesteps in the inner regions of a halo (see Figure 2 in Diemand et al. 2004c), but the dynamical times decrease all the way down to the center. Therefore the timestep criterium was slightly modified, to make sure enough timesteps are taken also near the halo centers: Instead of $\Delta t_i < \eta\sqrt{\epsilon/a_i}$ we now use

$$\Delta t < \min(\eta\sqrt{\epsilon/a_i}, \eta/4\sqrt{G\rho_i}) \quad , \tag{4.1}$$

where ρ_i is the density at the position of particle "i", obtained by smoothing over 64 nearest neighbors. We used $\eta = 0.25$ for all multi-mass runs. Note that in the inner region of a CDM halo $\rho(r) \simeq 0.6\rho(< r)$, i.e. $0.8\ \sqrt{G\rho(r_i)} \simeq \sqrt{G\rho(< r_i)}$ therefore the condition (4.1) with $\eta = 0.25$ assures that at least 12 timesteps per local dynamical time $1/\sqrt{G\rho(< r_i)}$ are taken.

The timesteps are obtained by dividing the main timestep ($t_0/200$) by factors of two until condition (4.1) is fulfilled. In run DM25 the smallest particle timesteps are $t_0/51200$. At each time between $z = 1.6$ and $z = 0.8$ only less than one thousand particles (and most of time just around 50) are on timesteps smaller than $t_0/12800$, therefore we introduce a maximal timestep of $t_0/12800$ from $z = 0.8$ to present to speedup the run. According to Figure 2 in Diemand et al. (2004c) this timestep is still sufficient to resolve at least 0.1 percent of the virial radius, which is less than the limit set by our mass resolution.

4.3.3 Testing the multi mass technique

Reducing the high resolution region in the way described above produces multi mass virialised systems, i.e. halos where particles of different mass are mixed up with each other. The inner regions are dominated by light particles and the region near the virial radius by heavier particles. But there are particles of both species everywhere in the final halo and one has to worry if this mixing introduces numerical effects, like energy transfer from the outer part to the inner part (from the heavy to the light particles) due to two body interactions. This could lead to numerical flattening of the density profile and make heavy particles sink to the center (Binney & Knebe 2002; Diemand et al. 2004a). To check if these effect are important for our multi mass runs, we did re-run the simulation D9 from Diemand et al. (2004c) with a reduced high resolution region and surrounded by 27 times heavier particles. The heavier particles have quite a large softening of 15 kpc to suppress discreteness effects. We call this multi mass run "DM9". Figure 4.1 shows that the density profiles of the fully refined run D9 and the partially refined run DM9 are identical over the entire resolved range. This indicates that the reduced refinement regions work well in run D9M and therefore we used the same refinement regions to set up the highest resolution run DM25. In this run the heavier particles are 125 more massive than the high resolution particles and they have a softening of 9 kpc. We cannot poof here that the multi-mass method works also with this larger mass ratio, it is possible that there is some numerical shallowing of the profiles simulated with this larger mass ratio. The panels on the left of

Figure 4.1 show how the initially separated species of light and heavy particles mix up during the the runs DM25 and DM9. Run DM9 has constant amounts of mixing both at z=0.8 and at z=0, and there smallest radius of a heavy particle is roughly constant at about 3 percent of the final virial radius. However in run DM25 there two species are more mixed up at both times, some heavy particles sink towards the center during the run: At z=0.8 the density of heavy particles at one percent of the virial radius is about 600 $\rho_{\rm crit}(z=0)$ and it grows to 2000 $\rho_{\rm crit}(z=0)$ at present time. DM9 and DM25 have similar peak densities of heavy particles at z=0.8, but at z=0 it is higher in DM25.

These tests show that the inner profile of DM9 does not suffer any numerical flattening due to the multi-mass setup and they indicate the same is true for run DM25 at z=0.8. However it is not clear if we can also trust the inner profile of DM25 at z=0.

4.4 The inner density profiles

Here we try to answer the question if the inner density profiles of dark matter halos have a constant density or a cusp $\rho(r) \propto r^{-\gamma}$. At resolutions of up to 25 million particles within the virial radius there is no evident convergence towards any constant inner slope (Fukushige et al. 2004;Diemand et al. 2004c). Run DM25 has an effective resolution corresponding to 127 million particles within the virial radius and a force resolution of $0.48 \times 10^{-3} r_{\rm vir}$. At this up to now unmatched resolution the inner slope is roughly constant from to the resolved radius (see Figure 4.2) out to about one percent of the virial radius of the final cluster at almost all times. Inside of the convergence radius the density profile is affected by numerical flattening and the slope goes to zero. During major mergers the inner profile is shallower than at quiet, relaxed states. At z=0.23 the main cluster is about to merge with another massive clusters, the separation of the cluster cores at this time is about 5 percent of the final virial radius which causes the exceptionally shallow the slope at this radius. (Earlier at z=0.47 these cores are separated by $0.16 r_{\rm vir}(z=0)$.) In the final output the slope is not constant down to the convergence radius anymore. We are not sure if this is due to numerical or physical effects. One worry is that the stronger mixing and larger mass difference in run DM25 compared to DM9 leads to energy transfer from the heavier to the lighter particles and to numerical shallowing of the cusp (see Section 4.3.3).

Run D12 resolves the same cluster with 14 million particles and shows no convergence to a constant inner slope. Note that the “D” cluster is one of six clusters analysed in Diemand et al. (2004c) and its inner profile is not special and rather close to the sample average.

Figure 4.2 indicates that there is a cusp in the centers of cold dark matter clusters and it becomes apparent only at this very high numerical resolution. The non-constant slopes just near the convergence scale are probably due to the first signs of numerical flattening that set in at this scale. About the density below the resolved scales one cannot make any robust predictions, but if one has to extrapolate into this region Figure 4.2 motivates the choice of a cusp $\rho(r) \propto r^{-\gamma}$ with $\gamma \simeq 1.2$.

4.4.1 Cored and cuspy fitting functions

In this section we fit one cuspy and two recently proposed cored functions to the density profiles at z=0.8 and at z=0.05. From the last section we expect the cuspy function to

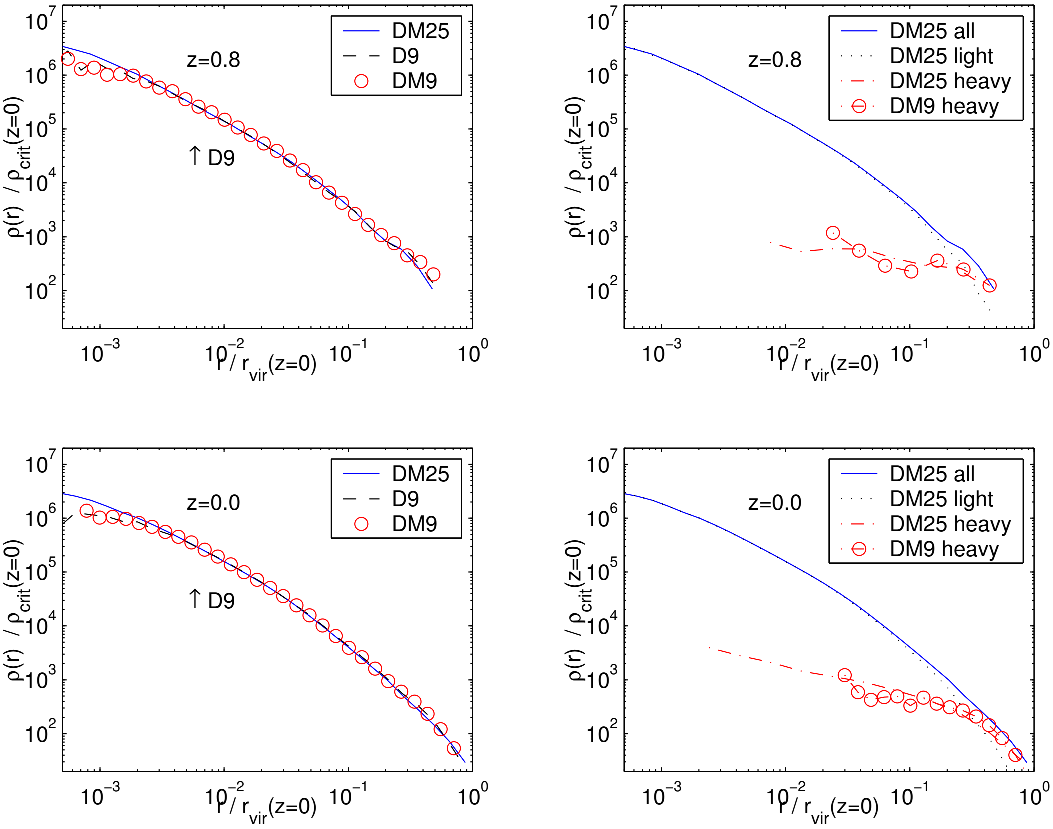

Figure 4.1: Tests of multi-mass refinement and convergence. Left panels show that run D9, which contains only high resolution particles within the virial radius, has the same density profile as the multi-mass run DM9. The arrows indicate the convergence radius of run D9 estimated in Diemand et al. (2004c). The panels on the right illustrate the mixing of light and heavy particles in runs DM9 and DM25. Both runs have identical refinement regions.

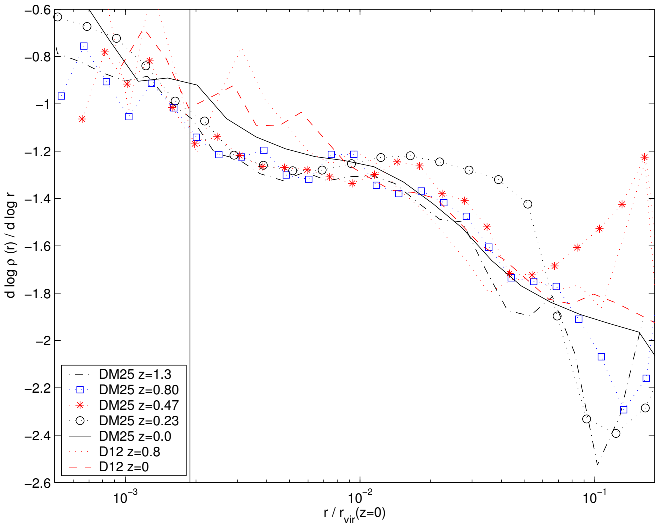

Figure 4.2: Logarithmic slope of the density profile of run DM25 at different output times between z=1.3 and z=0. The slope of run D12 at z=0.8 and z=0 is also shown for comparison. The vertical line indicates the estimated convergence radius of 3.3 kpc for DM25.

work better in the inner part, but we try to fit also the cored profiles for comparison.

We use a general $\alpha\beta\gamma$-profile (Zhao, 1996) that asymptotes to a central cusp $\rho(r) \propto r^{-\gamma}$:

$$\rho_{\rm G}(r) = \frac{\rho_s}{(r/r_s)^{\gamma}(1+(r/r_s)^{\alpha})^{(\beta-\gamma)/\alpha}}\,. \tag{4.2}$$

If one takes α, β and γ as free parameters one encounters strong degeneracies, i.e. very different combinations of parameter values can fit a typical density profile equally well Klypin et al. (2001). Therefore we fix the outer slope $\beta = 3$ and the turnover parameter $\alpha = 1$. For comparison the NFW profile has $(\alpha, \beta, \gamma) = (1, 3, 1)$, the M99 profile has $(\alpha, \beta, \gamma) = (1.5, 3, 1.5)$. We fit the three parameters γ, r_s and ρ_s to the data.

Navarro et al. (2004) proposed a different fitting function which curves smoothly over to a constant density at very small radii:

$$\ln(\rho_{\rm N}(r)/\rho_s) = (-2/\alpha_{\rm N})\left[(r/r_s)^{\alpha_{\rm N}} - 1\right] \tag{4.3}$$

$\alpha_{\rm N}$ determines how fast the profile (4.3) turns away from a power law near the centre. Navarro et al. (2004) found that $\alpha_{\rm N}$ is independent of halo mass and $\alpha_{\rm N} = 0.172 \pm 0.032$ for all their simulations, including galaxies and dwarfs.

Another that also curves away from a power law behaviour in the inner part faster than (4.3) was proposed in Stoehr et. al (2002):

$$\begin{aligned}\rho_{\rm SWTS}(r) = \frac{V_{max}^2}{4\pi G}\, 10^{-2a_{\rm SWTS}\left[\log\left(\frac{r}{r_{max}}\right)\right]^2} \frac{1}{r^2} \times \\ \times \left[1 - 4\ a\ \log\left(\frac{r}{r_{max}}\right)\right]\end{aligned} \tag{4.4}$$

where V_{max} is the peak value of the circular velocity, r_{max} is the radius of the peak and $a_{\rm SWTS}$ determines how fast the profile turns away from an power law near the centre.

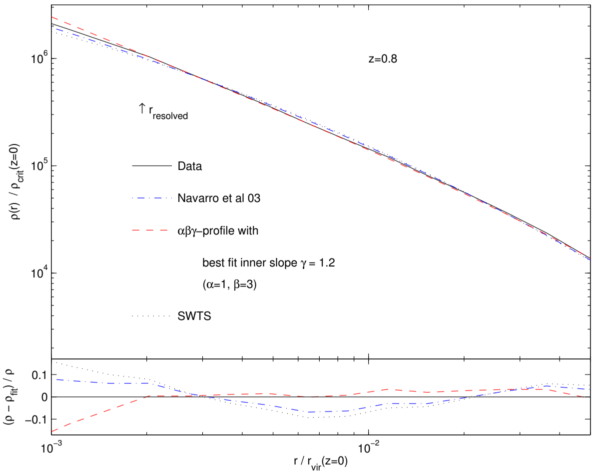

Figure 4.3: Density profile of run DM25 at z=0.8 and fits with three different functions.

Table 4.2: Density profile parameters of run DM25. Δ is the root mean square of $(\rho - \rho_{\mathrm{fit}})/\rho$ for the three fitting functions used.

z	γ_{G}	r_{sG} [kpc]	Δ_{G}	α_{N}	$r_{\mathrm{s\ N}}$ [kpc]	Δ_{N}	a_{SWTS}	$r_{\mathrm{max\ SWTS}}$ [kpc]	Δ_{SWTS}
0.8	1.20	260	0.075	0.157	233	0.076	0.130	565	0.087
0.05	1.20	308	0.065	0.165	242	0.033	0.143	532	0.053

Stoehr (2004) found that cluster profiles are well fitted with this formula using a_{SWTS} values between 0.093 and 0.15.

These three function were fitted to the data from z=0.8 and z=0.05 by minimizing the relative density differences in each of about 20 logarithmically spaced bins in the resolved range (i.e. form r_{resolved} =3.3 kpc to r_{vir} =1750 kpc). The resulting best fit values and root mean squares of the relative density differences are given in Table 4.2.

The average residuals of the three fits are very similar, but they are dominated by the contribution from the outer parts of the cluster (see also Figure 6 in Diemand et al. 2004c). Figures 4.3 and 4.4 show that in the inner part the cuspy profile describes the data better, especially at z=0.8, but also at z=0.05. Both cored profiles *underestimate* the measured density at the resolution limit. These profiles lie *below* the measured density profiles even *inside* of r_{resolved} where one has to expect that the next generation of simulations will be able to resolve even higher densities.

Figures 4.5 and 4.6 show the slopes of the simulated profile in comparison with the slopes of the best fits. Again it is evident that in the inner part the cuspy profile describes the measured density profile better.

4.5 Conclusions

The main conclusions of this work are the following:

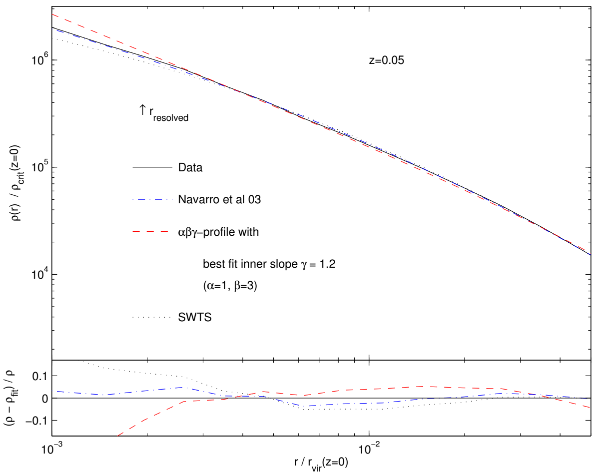

Figure 4.4: Density profile of run DM25 at z=0.05 and fits with three different functions.

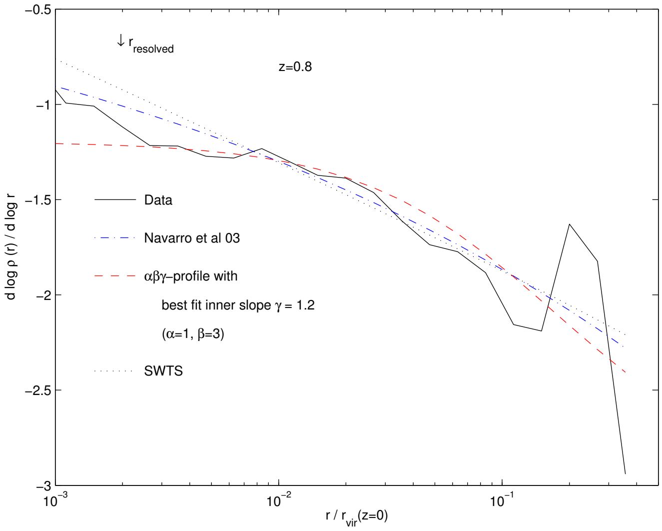

Figure 4.5: Logarithmic slopes of the measured and fitted density profiles from Figure 4.3.

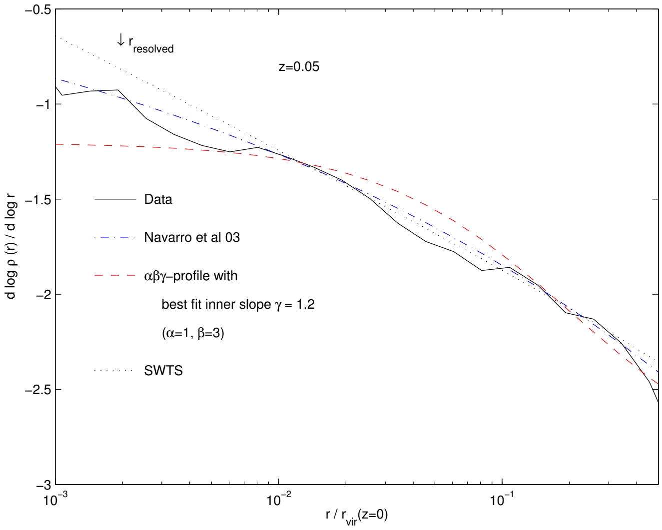

Figure 4.6: Logarithmic slopes of the measured and fitted density profiles from Figure 4.4.

- It is possible to use different mass particles to resolve one halo in cosmological CDM simulations without affecting the resulting density profiles.

- This “multi-mass” technique allows a reduction of the necessary number of particles and the computational cost by at least one order of magnitude without loss of resolution in the crucial central region of the halo.

- The logarithmic slope of the dark matter density profile converges to a roughly constant value in the inner part of cluster halos.

- This probably also holds also for smaller systems (like galaxy and dwarf halos) but there it is even more difficult to numerically resolve the cusps.

- At resolutions around 10 million particles per halo the inner slope appears to contінously approach zero, but this impression is caused by numerical flattening of the profiles due to insufficient mass resolution.

- The cluster studied here has cusp in the inner part, $\rho \propto r^{-\gamma}$ with a slope of about $\gamma = 1.2$. From earlier studies (Diemand et al., 2004c) we expect this inner profile to be close to the average and the scatter is about ± 0.15 in γ.

- Best fit profiles with a core (Stoehr et. al 2002;Navarro et al. 2004) *underestimate* the measured dark matter density at (and even *inside* of) the current resolution limit.

Acknowledgments

Marcel Zemp made many important contributions to this work, and the setup of the initial conditions was motivated and guided by his experience with multi mass spherical halo models (Zemp, in prep.). The simulations were performed on the zBox supercomputer at the University of Zurich. J. D. is supported by the Swiss National Science Foundation.

Chapter 5

Velocity and spatial biases in CDM subhalo distributions [1]

5.1 Abstract

We present a statistical study of substructure within a sample of ΛCDM clusters and galaxies simulated with up to 25 million particles. With thousands of subhalos per object we can accurately measure their spatial clustering and velocity distribution functions and compare these with observational data. The substructure properties of galactic halos closely resembles those of galaxy clusters with a small scatter in the mass and circular velocity functions. The velocity distribution function is non-Maxwellian and flat topped with a negative kurtosis of about -0.7. Within the virial radius the velocity bias $b = \sigma_{\rm sub}/\sigma_{\rm DM} \sim 1.12 \pm 0.04$, increasing to $b > 1.3$ within the halo centers. Slow subhalos are much less common, due to physical disruption by gravitational tides early in the merging history. This leads to a spatially anti-biased subhalo distribution that is well fitted by a cored isothermal. Observations of cluster galaxies do not show such biases which we interpret as a limitation of pure dark matter simulations - we estimate that we are missing half of the halo population which has been destroyed by physical overmerging. High resolution hydrodynamical simulations are required to study these issues further. If CDM is correct then the cluster galaxies must survive the tidal field, perhaps due to baryonic inflow during elliptical galaxy formation. Spirals can never exist near the cluster centers and the elliptical galaxies there will have little remaining dark matter. This implies that the morphology-density relation is set *before* the cluster forms, rather than a subsequent transformation of disks to S0's by virtue of the cluster environment.

5.2 Introduction

Early simulation work that attempted to follow the merging hierarchy produced a final dark matter structure that was nearly entirely smooth (White 1976; White et al. 1987; Carlberg 1994; Summers, Davis & Evrard 1995; Tormen, Bouchet & White 1997). The reason for this behaviour was debated in the literature as being due to physical or numerical overmerging (White & Rees 1978; Carlberg 1994; van Kampen 1995; Moore, Katz & Lake 1996). The development of fast algorithms to accurately integrate the orbits of

---

[1] This chapter is published in: MNRAS, 2004, 352, 535. (Diemand et al., 2004b).

millions of particles overcame this problem. The first halos simulated with sufficient resolution contained of the order a thousand substructure halos with properties that resembled galaxies within clusters (Moore et al., 1998). These simulations took many months using parallel gravity codes running on hundreds of processors.

Ongoing research in this area has given many interesting results and we list some of the main conclusions here (Ghigna et al. 1998; Okamoto & Habe 1999; Klypin et al. 1999a; Klypin et al. 1999b, Moore et al. 1999a; Ghigna et al. 2000; Springel et al. 2001b; De Lucia et al. 2004): (i) Subhalos make up a fraction of between 5 and 10% of the mass of virialised halos. (ii) Halos on all mass scales have similar substructure populations. (iii) The mass and circular velocity function of subhalos are power laws with slopes -1 and -3. (iv) Velocity bias between the subhalos and smooth dark matter background may be significant. (v) The radial number density profile of subhalos is shallower than the dark matter background. (vi) Subhalos are significantly rounder than field halos (vii) The orbits of subhalos are close to isotropic with apo:peri approximately 4:1. (viii) Subhalos suffer mass loss from tidal stripping which modifies their outer density profiles. (ix) The tidal radii of subhalos decreases with cluster-centric position. (x) Most of the surviving population of subhalos entered the parent halo late.

Several of these statements remain controversial and further work is necessary to clarify certain issues. In this paper we re-address conclusions (i)-(v) and attempt to answer some of the remaining questions, including: What is the scatter in the mass and circular velocity distributions? Is there a positive or negative velocity bias and if so what is its origin? Ghigna et al. (2000); Colin, Klypin, & Kravtsov (2000) claim a positive velocity bias whilst Springel et al. (2001b) report a negative velocity bias. Have we converged in the properties of subhalos, including their radial distribution and mass functions? The inner regions ($r < 0.2\ r_{virial}$) of clusters and galaxy dark matter simulations are nearly smooth but is numerical overmerging still occurring in these very high density regions? Does the spatial distribution of galaxies in clusters resemble that of the subhalos in simulations? On galaxy scales the observed distribution of satellites is more concentrated than the simulations. Theory can be reconciled with the observations if it is assumed that the visible satellites are a biased subset of the total population (Taylor, Silk, & Babul 2003; Kravtsov, Gnedin & Klypin 2004). On cluster scales we do not expect to find “dark galaxy halos” therefore it is interesting to compare the observed distribution of galaxies with the distribution of substructure.

In this paper we analyse a sample of six high resolution simulations of clusters containing between 5 and 25 million particles integrated with high force accuracy. We compare the mass functions with a sample of galactic mass halos with slightly lower resolution. These new simulations are presented in Section 5.3 and the general properties of the subhalos are given in Section 5.4.

5.3 Numerical experiments

Table 5.1 gives an overview of the simulations we present in this paper. With up to 25×10^6 particles inside the virial radius of one cluster they are among the highest resolution ΛCDM simulations performed so far. They represent a major investment of computing time, the largest run was completed in about 5 10^5 CPU hours on the zBox supercomputer [1].

---

[1] http://www-theorie.physik.unizh.ch/~stadel/zBox/

Table 5.1: Parameters of resimulated clusters. The last four columns give properties of all subhalos with at least 32 bound particles, their number, bound mass fraction, the radius of the innermost subhalo and the velocity bias $b = \sigma_{\mathrm{sub}}/\sigma_{\mathrm{DM}}$. In clusters $A9$ and $C9$ these structures are the cores of massive clusters that are about to merge with the main cluster at $z = 0$.

Run	ϵ_0 [kpc]	N_{virial} 10^6	M_{virial} $10^{15}[\mathrm{M}_\odot]$	r_{virial} [kpc]	$v_{\mathrm{v,max}}$ $[\mathrm{km\ s}^1]$	$r_{\mathrm{vc,max}}$ [kpc]	n_{halo}	$\frac{\Sigma m_{\mathrm{halo}}}{M_{\mathrm{virial}}}$	$r_{\mathrm{sub,min}}$ [kpc]	b
$A9$	2.4	25	1.3×10^{15}	2850	1428	1853	5114	0.07	126*	1.10
$B9$	4.8	11	5.9×10^{14}	2166	1120	1321	1940	0.12	162	1.12
$C9$	2.4	10	5.0×10^{14}	2055	1090	904	1576	0.11	77*	1.15
$D3h$	1.8	0.2	2.8×10^{14}	1704	944	834	36	0.03	260	1.11
$D6h$	1.8	1.8	3.1×10^{14}	1743	975	784	307	0.04	136	1.11
$D6$	3.6	1.8	3.1×10^{14}	1749	981	840	322	0.05	227	1.13
$D9$	2.4	6.0	3.1×10^{14}	1752	983	876	929	0.06	126	1.11
$D9lt$	2.4	6.0	3.1×10^{14}	1752	984	841	912	0.05	183	1.11
$D12$	1.8	14	3.1×10^{14}	1743	958	645	1847	0.06	136	1.11
$E9$	2.4	5.0	2.6×10^{14}	1647	891	889	829	0.06	172	1.11
$F9$	2.4	4.6	2.4×10^{14}	1598	897	655	721	0.06	176	1.08
$F9cm$	2.4	4.6	2.4×10^{14}	1598	898	655	661	0.06	127	1.08
$F9ft$	2.4	4.6	2.4×10^{14}	1601	905	464	706	0.06	161	1.07
$G0$	0.27	1.7	1.01×10^{12}	260	160	52.2	144	0.03	16	1.05
$G1$	0.27	1.9	1.12×10^{12}	268	162	51.3	189	0.04	20	1.03
$G2$	0.27	3.8	2.21×10^{12}	337	190	94.5	462	0.04	21	1.10
$G3$	0.27	2.6	1.54×10^{12}	299	180	45.1	314	0.03	28	1.12

Figure 5.1: Density map for run $D12$ out to the virial radius. This cluster is prolate with a 3:1 major:minor axis ratio. Higher resolution color pictures and a mpeg movie of the formation of cluster $C9$ can be downloaded from http://www-theorie.physik.unizh.ch/∼diemand/clusters/

5.3.1 N-body code and numerical parameters

The simulations were carried out using PKDGRAV written by Joachim Stadel and Thomas Quinn (Stadel, 2001). Individual time steps are chosen for each particle proportional to the square root of the softening length over the acceleration, $\Delta t_i = \eta\sqrt{\epsilon/a_i}$. We use $\eta = 0.2$ for most runs, only in run $D9lt$ we used larger timesteps $\eta = 0.3$. The node-opening angle is set to $\theta = 0.55$ initially and after $z = 2$ to $\theta = 0.7$ to speedup the runs. The code uses a spline softening length ϵ, forces are completely Newtonian at 2ϵ. In table 5.1 ϵ_0 is the softening length at $z = 0$, ϵ_{max} is the maximal softening in comoving coordinates. In most runs the softening is constant in physical coordinates from $z = 9$ to present and constant in comoving coordinates before, i.e. $\epsilon_{\mathrm{max}} = 10\epsilon_0$. In runs $C9$ and $F9cm$ the softening is constant in comoving coordinates for the entire run, in run $F9ft$ the softening has a constant physical length for the entire run.

5.3.2 Initial conditions and cosmological parameters

We use a ΛCDM cosmological model with parameters from the first year WMAP results: $\Omega_\Lambda = 0.732$, $\Omega_m = 0.268$, $\sigma_8 = 0.9$, (Spergel et al., 2003). The initial conditions are generated with the GRAFIC2 package (Bertschinger, 2001). Six clusters were selected from a parent simulation and resimulated with much higher mass and force resolution, details about the selection and the refinement are given in Diemand et al. (2004c). We label the six cluster (ordered by their mass) with letters A to F and with a number that gives the refinement factor in length relative to the 300^3 in $(300\ \mathrm{Mpc})^3$ parent simulation, e.g. 'D12' is the fourth most massive cluster in our sample, and the mass resolution corresponds to $(12 \times 300)^3$ particles in a 300 Mpc cube simulation.

We also present results from four medium resolution galaxy mass halos which we label G0, G1, G2 and G3. These halos contain 2-4 million particles within their virial radii. The parent simulation is a 90 Mpc cube resolved with 300^3 particles initially. The four galaxies all lie within a volume of about 1000 cubic Mpc (at $z = 0$) which was refined by a factor of 12 in length to reach the resolution given in Table 5.1.

5.3.3 Substructure identification

Within the virial radius of the high resolution CDM simulations we can resolve thousands of substructure halos, i.e. self-bound over-dense clusters of particles (See Figure 1). They span a wide range in mass, from the resolution limit of a few tens of particles up to few percent of the cluster mass, i.e. from $10^8\mathrm{M}_\odot$ to $10^{13}\mathrm{M}_\odot$. Some of the subhalos even contain their own substructure. Therefore robust identification of subhalos a very difficult task, there is no general, parameter free method that is able to extract the entire hierarchy of halos.

We identify subhalos with SKID (Stadel, 2001) and with a new parallel adaptive Friends of Friends ('FoF', see Davis et al. (1985)) group finder ('AdFoF'). SKID calculates local densities using an SPH kernel, then particles are moved along the density gradient until they oscillate around a point (i.e. move less than some length l). Then they are linked together using FoF with this l as a linking length. AdFoF first calculates the background density of the cluster ρ_{BG} using spherical bins. The linking lengths for the particles are set to $b = (\Delta\rho_{\mathrm{BG}}/m_p)^{-1/3}$, m_p is the particle mass, $\Delta = 5$ is the density contrast, the only free parameter of this method. Two nearby particles can now have different linking lengths, they are considered as friends if one of them considers the other one his friend, i.e. the maximum of the two linking lengths is used. Both the SKID and the AdFoF groups are checked for self-boundness and unbound particles are removed with the same iterative procedure.

We compared SKID results (using $l = 1.5\epsilon_0$, $l = 4\epsilon_0$ and $l = 10\epsilon_0$) with the AdFof results and we also visually compared the identified groups with the density map of the cluster: SKID with $l = 4\epsilon_0$ adequately identifies the smallest subhalos and the centers of the largest subhalos. For the latter the calculated bound mass is underestimated. Using $l = 10\epsilon_0$ can be cure this, but then some of the small subhalos are missed. The AdFoF has the advantage that in principle it links together all particles in regions with a density contrast of Δ against the background density. With $\Delta = 5$ AdFof finds the same groups as SKID, but the current version using the spherically averaged density for the background also finds some spurious groups since the background isodensity surfaces have triaxial shape in a CDM cluster. For example, particles on the long axis of a prolate halo can be linked together, since their density is higher than the spherical average. The subhalo catalogues we analyse in this paper are generated in two steps: First we use SKID with $l = 4\epsilon_0$, this gives a complete catalogue of all the subhalo centers and also the correct subhalo properties for the smaller objects. Then we run AdFoF with $\Delta = 5$ and combine the resulting substructure catalogue with the SKID output to obtain the correct subhalo properties also for the larger objects: if AdFoF found a subhalo at the same position as SKID, the properties from the catalogue where this halo has a larger bound mass are used. The mass fraction bound to subhalos with $\mathrm{N} \geq 32$ (the cluster centre is not considered a subhalo) is given in Table 5.1. Using the AdFoF or the SKID $l = 4\epsilon_0$ catalogue alone gives about 20 percent smaller values. Using SKID with $l = 1.5\epsilon_0$ underestimates the masses of the biggest subhalos which dominate the bound mass fraction, and the results are as much as a factor of two below the quoted values.

To check for systematic errors in the substructure catalogue constructed in this way, we confirmed that the substructure mass function and the number density profile of one cluster ($D9$) remains the same when we construct the substructure catalogue in two alternative ways: The first alternative catalogue was constructed by combining three SKID outputs with $l = 1.5, 4$ and $10\epsilon_0$ as in Ghigna et al. (2000), the second alternative was the combination of two SKID outputs with $l = 1.5$ and $4\epsilon_0$ and a one $\Delta = 5$ AdFoF output. We found that the $l = 1.5\epsilon_0$ SKID does not find additional structure, the $l = 4\epsilon_0$ contains all the small subhalos down to the minimum number of 10. By comparing the final halo catalogue of cluster D12 to regions of the density map of this cluster (Figure 5.1) we checked that no subhalos were missed and that no non-existent halos were included.

5.4 Cluster substructure

We identified subhalos within the virial radii of our six clusters at redshift zero, the algorithms used are described in section 5.3.3. At the highest resolution we found over 5000 subhalos (≥ 32 particles) inside the virial radius of the most massive cluster.

5.4.1 Spatial antibias and convergence tests

In this section we study the convergence of substructure properties, including density profiles, cumulative mass functions and relative number density profiles (Figure 5.2). First we check if these properties change with varying force and time resolution, i.e we compare *D*6 and *D*6*h*; *D*9 and *D9lt*; *F*9, *F9cm* and *F*9*ft*. The only slight difference we found is in the relative number density profile: the better force resolution in *D*6*h* leads to a few more surviving substructures near the center (4 subhalos within 10 percent of the virial radius), run *D*6 has no subhalos within the same radius. Therefore the original numerical overmerging problem (Moore, Katz & Lake, 1996) due to insufficient force resolution is not the limiting factor anymore, except near the center of the halos ($r < 0.1 r_{\rm virial}$).

The amount of substructure that our simulations can resolve is mostly limited by mass resolution. Subhalos have very high phase space densities, i.e. relatively short relaxation times. Numerical two body relaxation due to finite mass resolution heats up their cores and makes them less dense (Diemand et al., 2004a). The difference in central density is about a factor of two between subhalos resolved with 500 and 4000 particles (see panel (a) of Figure 5.2 and also Kazantzidis et al. (2004b) where subhalo profiles from clusters *D*6, *D*9 and *D*12 and their evolution are presented). Subhalos with even less particles show this effect more strongly and have much shallower density profiles. These are less resistant against tidal stripping and total disruption (Moore et al., 1996).

Figure 5.2 shows substructure properties of the same cluster, *D*, simulated at different mass resolutions with $N_{\rm virial}$ = 205k, 1.7M, 6M and 14M. Panels (c) and (d) of Figure 5.2 show the cumulative mass function including all subhalos with more than 10 particles. Resolution clearly affects the numbers of subhalos at the limiting mass of 10 particle masses (m_p), however the amount of surviving substructure converges at a mass of about 100 m_p for the D6h run. In analogy with the convergence in density profiles (see Diemand et al. 2004c and references therein) we do not expect that this number is valid for a large range of mass resolutions and it is possible that the high resolution mass functions are only complete above a mass of a few hundred particle masses, especially in the inner region. We usually include all subhalos with at least 32 bound particles for the analysis presented in this paper, and we will always show how the results depend on this minimal number of particles (in most cases the influence is small).

Panel (b) of Figure 5.2 shows the number density of subhalos in spherical bins relative to the number density within the virial radius $< n_{virial} >= N_{sub}/V_{\rm virial}$. The first bin is centered on the innermost subhalo (the cluster center is not considered as a subhalo), so the first data point also gives the radius $r_{\rm min}$ of the subhalo closest to the center. The size of each bin is set to $r_{\rm min}$, so the first bin starts at $r_{\rm min}/2$ and ends at $1.5 r_{\rm min}$. Tidal disruption is most effective near the cluster center which leads to an antibias in the density profile of substructure relative to the smooth background. This implies that if galaxies are associated with the subhalos, they do not trace the matter distribution of a cluster. Is this antibias real or just an effect of finite resolution? Runs *D*6*h*, *D*9 and *D*12 have very similar relative number density profiles. If one only considers groups above the 10 particle limit of *D*6*h* (i. e. above 80 m_p in run *D*12), run *D*12 resolves about twice as many halos as *D*6*h* (920 against 582, at the vertical line in Panel c) and it is interesting to see where these halos lie. They are not significantly more centrally concentrated, they have a very similar radial distribution as the halos that survived in run *D*6*h*. Even the subhalo distribution of all subhalos in *D*3*h* (N$\geq$ 10) is very similar to the one of the subhalos in *D*12 in the same mass range (N $\geq$ 640) which are resolved with 64 times more particles. If the convergence scale depends only mildly on N, for example $r_{\rm converged} \propto N^{-1/3}$ as in the case of the density profiles (see Diemand et al. 2004c and references therein), the wide range of resolutions presented here gives for the first time a robust confirmation of convergence in the radial distribution of subhalos. So the antibias in number density does not depend on the numerical resolution, but the higher resolution runs allow to measure the number density profiles closer to the center.

The relative number density of subhalos can be approximated by an isothermal profile with a core shown by the thin solid line in panel (b) of Figure 5.2

$$n(r) = 2n_{\rm H}\left(1 + (r/r_{\rm H})^2\right)^{-1} , \tag{5.1}$$

where $n_{\rm H}$ is the relative number density at a subhalos scale radius $r_{\rm H}$. The average core radius of the distribution of cluster subhalos is $r_{\rm H} \simeq 0.37\ r_{\rm virial} \simeq 2/3\ r_{\rm vc,max}$, where $r_{\rm vc,max}$ is the radius where the circular velocity has its maximum, see Table (5.1).

5.4.2 Substructure abundance

Figure 5.3 shows the cumulative substructure mass functions and inner mass functions of the six clusters which are all well approximated by a simple power law m^{-1}. Here we include subhalos with a minimum of 32 particles, we found in the last section that the subhalo catalogues are complete only above a mass corresponding to about 100 particles. The apparent flattening of the slope towards this mass is due to finite resolution and does not indicate a shallower power law at lower masses. This can also be seen from the fact that around $m = 10^{-5} M_{\rm virial}$ the larger halos and run $D12$ (i.e. those with better relative mass resolution) have steeper slopes. If hierarchical merging should produce subhalo mass functions that do not depend on the mass of the parent halo (as shown in Moore et al. (1999a), see also Section 5.4.5 of this paper) the natural outcome is an m^{-1} power law: If one simply adds two equal halos the amount of substructure above any fixed absolute mass doubles, the remnant has now twice the mass and it only has the same amount of substructure at a fixed relative mass if the mass function of the progenitors was m^{-1}. The mass function of isolated field halos is also close to a power law of slope m^{-1} (e.g. Jenkins et al. 2001; Reed et al. 2003a). Thus tidal stripping acts to lose mass in such a way that the overall mass function slope does not change. The conspiracy is such that stripped halos move down the M versus $v_{\rm c,max}$ plane such that they follow the line for field halos (Ghigna et al., 1998).

The cumulative substructure velocity functions (see Figure 5.3, Panel (c)) gives the number of subhalos with maximum circular velocities above a given value. The virial theorem $v_{\rm c,max}^2 \propto M_{\rm halo}/R \propto M_{\rm halo}/M_{\rm halo}^{1/3}$ leads to a simple scaling $M_{\rm halo} \propto v_{\rm c,max}^3$ for field halos. This relation is also a good approximation for subhalos, even if they lost most of their mass due to tidal stripping (Ghigna et al. 1998; Kravtsov et al. 2004). Since the cumulative mass function goes like m^{-1}, we expect the cumulative mass functions to follow a $v_{\rm c,max}^{-3}$ power law. This is true in a wide range of velocities. Towards the resolution limit the velocity functions also become shallower, but this is due to the same numerical effect as in the case of the mass functions. The scatter in the substructure abundance is large at the high mass end (a factor three) where the mass functions depend on a small number of massive objects. At intermediate and small subhalo masses ($< 10^{-4} M_{vir}$) the scatter is within a factor of 1.7.

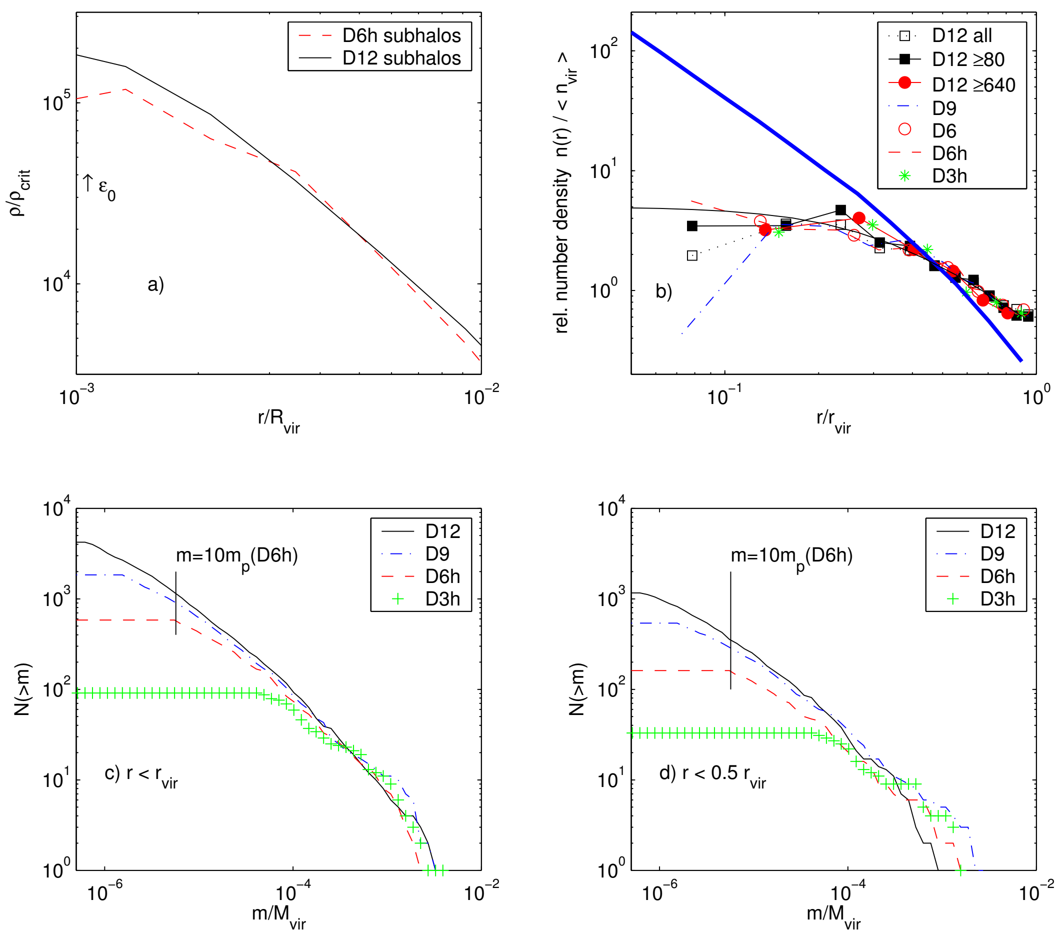

Figure 5.2: Substructure properties at different mass resolutions: (a) Average density profiles of 5 subhalos with masses close to $2.9 \times 10^{-4} M_{\mathrm{virial}}$ resolved with about 4,000 particles in run D12 and 500 in run D6h. (b) Relative number density of subhalos with different mass and force resolution, fitted by an isothermal profile with a core (5.1) The thick line is the density profile of the DM particles. (c) Cumulative mass functions of substructure within r_{virial} including halos down to 10 m_p. (d) Inner cumulative mass functions, same as (c) but only including halos within 0.5 r_{virial}.

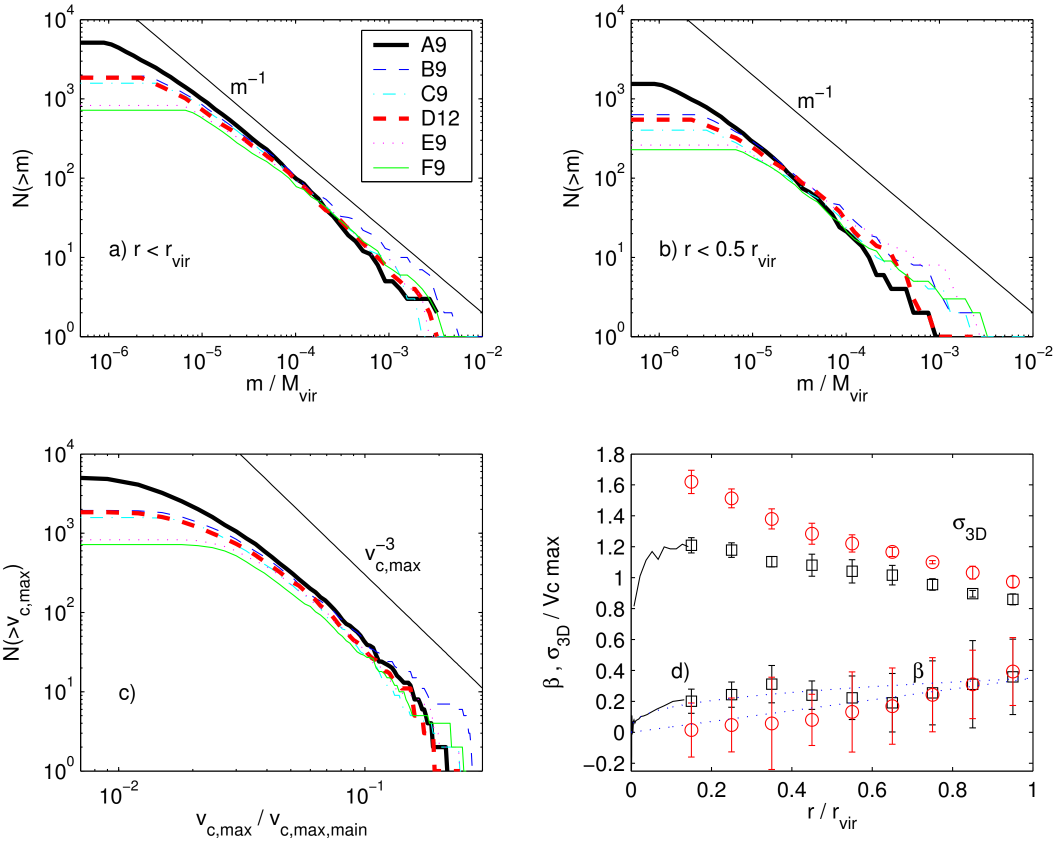

Figure 5.3: Substructure properties of the six clusters. Only halos with at least 32 bound particles are considered. (a) Cumulative mass functions of substructure within r_{virial}. (b) Inner cumulative mass functions, including halos within 0.5 r_{virial}. (c) Cumulative number of subhalos as a function of their circular velocity. (d) 3D velocity dispersion of sub halos (circles) and dark matter background (squares) as a function of radius. Averages over all 6 cluster profiles, normalised to the maximum circular velocity. Error bars show the scatter between the clusters. Poisson errors due to small number of subhalos per bin are smaller than 0.05 and are not included. The average of the anisotropy parameter $\beta = 1 - 0.5\sigma_t^2/\sigma_r^2$ is also plotted for the subhalos (circles) and the particles (squares). The particles are on slightly more radial orbits than the subhalos. The dotted lines are fitting functions, see text for details.

5.4.3 Subhalo velocity distribution

5.4.3.1 Velocity bias

Figure 5.3, panel (d) shows the 3D velocity dispersion of the smooth particle background and subhalos. We measured the dispersion profile for each individual cluster, then we averaged the values in each bin over all six clusters. The subhalos dispersions are not weighted by mass, each subhalo has equal weight. In a radial range from 0.1 $r_{\rm virial}$ to 0.4 $r_{\rm virial}$ the substructure halos have a higher 3D velocity dispersion than the background: $b = \sigma_{sub}/\sigma_{DM}$ is $b = 1.25 \pm 0.08$. The velocity bias of all subhalos within the virial radius $b = \sigma_{sub}/\sigma_{DM}$ is $b = 1.11 \pm 0.04$. The plotted and quoted errors are the scatter in our sample of six clusters and they are much larger than the Poisson noise in the estimated values of σ_{sub}.

A negative velocity bias was first considered by Carlberg & Couchman (1989) as a possible way of reconciling low cluster masses with a high matter density universe. Hints for positive bias ($b > 1$) were found by Ghigna et al. (1998) and also Colin, Klypin, & Kravtsov (2000) who combined 12 clusters containing 33 - 246 resolved subhalos to obtain a sufficiently large subhalo sample. The first simulation with sufficient resolution (about 5 million particles within the virial radius) to construct a reliable subhalo velocity dispersion profile from one object was analysed in Ghigna et al. (2000). They found $b = 1.2 - 1.3$ in their innermost bin, which goes from 0 to 0.25 $r_{\rm virial}$, and a small (< 1.10) positive bias for the entire cluster.

The bias is independent of subhalo mass, for example including only halos above $5 \times 10^{-5} M_{\rm virial}$ (979 subhalos or about 8 percent of the subhalos with $N \geq 32$) also gives $b = 1.11 \pm 0.04$. And for halos above $10^{-4} M_{\rm virial}$ (only 474 halos or 4 percent) $b = 1.10 \pm 0.05$. The velocity bias does not depend on resolution: In the radial range from 0.1 $r_{\rm virial}$ to 0.4 $r_{\rm virial}$ the values lie within $b = 1.16$ and $b = 1.25$ for all simulations of cluster D and there is no clear trend with resolution.

5.4.3.2 Anisotropy of subhalo velocities

In the radial and tangential velocity dispersions the bias is very similar as in the three dimensional dispersion. This can also be seen from the anisotropy parameter $\beta = 1 - 0.5\sigma_t^2/\sigma_r^2$, (Panel (d) in Figure 5.3): The anisotropy is very similar for subhalos and background particles, only in the inner region the subhalo velocities are slightly more isotropic than those of the particle background. From $r = 0$ to $r_{\rm virial}$ the anisotropy β grows roughly linear with radius: $\beta \simeq 0.35r$. For the average particle anisotropy $\beta \simeq 0.35r^{1/3}$ seems to fit the data better.

5.4.3.3 Subhalo dynamics

Here we investigate if the spatial and velocity distribution can be a steady-state solution of the collisionless Boltzmann equation (CBE) or if a supply of infalling structures is needed to maintain the state of the system observed at $z = 0$. We neglect the small anisotropy and assume spherical symmetry, then the integral of the second moment of the CBE, the Jeans Equation (Binney & Tremaine, 1987), reads

$$\rho_{\rm sub}(r)\sigma^2_{\rm r,sub}(r) = \int_r^c \rho_{\rm sub}(r)\frac{GM(r)}{r^2}dr \tag{5.2}$$

where c gives the size of the system, $\rho_{\rm sub}$ and $\sigma_{\rm r,sub}$ are the density and the one- dimensional dispersion of the subhalos and $M(r)$ is the cumulative *total* mass. A similar equation for the dark matter background is obtained by using density and dispersion of the dark matter instead.

The six clusters can be approximated as NFW profiles (Navarro et al., 1996) with a mean concentration of about $c_{\rm NFW} = 7$ (see Diemand et al. 2004c). Using this average dark matter density profile the $\sigma^2_{\rm r,DM}(r)$ from Equation (5.2) fit the measured values (Figure 5.3) very well. For the radial density profile of the subhalos we use Equation (5.1), with $r_{\rm H} = 2/3\ r_{\rm vc,max}$, the mean of $r_{\rm vc,max}$ is about 0.57 $r_{\rm virial}$. The expected bias is

$$b_{\rm th} = \frac{\sigma_{\rm r,sub}(r)}{\sigma_{\rm r,DM}(r)} = \left[\frac{\rho_{\rm DM}(r)}{\rho_{\rm sub}(r)} \frac{\int_r^c \rho_{\rm sub}(r) \frac{GM(r)}{r^2} dr}{\int_r^c \rho_{\rm DM}(r) \frac{GM(r)}{r^2} dr} \right]^{1/2} . \tag{5.3}$$

We use a cut off at $c = 2\ r_{\rm virial}$, at this radius the slopes of $\rho_{\rm sub}$ and $\rho_{\rm DM}$ become similar and the bias should vanish. Figure 5.4 shows the predicted and measured velocity bias and simple power law fit to the measured average velocity bias: $b_{\rm fit} = 1.12 \times (r/r_{\rm virial})^{-0.1}$. $b_{\rm th}$ is very close to the measured velocity bias, just in the inner region $b_{\rm th}$ is too large. This means that the subhalo-background system is close to a steady-state equilibrium configuration.

Therefore we expect the non-equilibrium processes to be subdominant. The net *infall* of subhalos can be quantified from the asymmetry of the radial velocity distribution of subhalos near the virial radius: The distributions are symmetric in the inner and outer part of the clusters and there is no net infall of subhalos at z=0. Another non-equilibrium process is the *disruption* of subhalos. The fraction of subhalos that are disrupted is small (see also Section 5.4.4), about 0.02 Gyr^{-1} for subhalos with N $\geq$ 100. In the inner 40 percent of the halo the fraction is bigger, about 0.13 Gyr^{-1}. This could be the reason why the steady-state solution over-predicts the velocity bias near the center.

5.4.3.4 Higher moments of the velocity distribution

In the last subsection we found that the second moment of the subhalo velocity distribution is consistent with a steady-state solution, where the subhalos have a spatial antibias. Now we consider the next higher moments of the velocity distributions of subhalos and particle background. In the radial range where the velocity bias is large (0.1 $r_{\rm virial}$ to 0.4 $r_{\rm virial}$) the shapes of these velocity distributions are very different (Figure 5.5). There are many less subhalos with small velocities (top panel), also the fraction of subhalos with low velocity components is smaller for the particles (bottom panel). While the particle velocity distribution is close to a Maxwellian, this is not true for the subhalos. The subhalo velocity histogram is flat-topped, it has smaller fourth moment than the Maxwell distribution, i.e. a negative kurtosis $k =< v^4 > / < v^2 >^2 -3 = -0.7$. We also calculated the first two non-trivial, even[2] Gauss-Hermite moments $h4$, $h6$ (Gerhard, 1993). In this radial range (0.1 - 0.4 $r_{\rm virial}$) we get $h_4 = -0.068$ and $h_6 = 0.0013$. The advantage of Gauss-Hermite moments over simple higher order moments is that they are not very sensitive to the wings of the distribution. In galaxy clusters these outer parts of the distribution are hard to determine exactly due to interlopers (van der Marel et al., 2000).

---

[2] The odd moments are zero for symmetric functions.

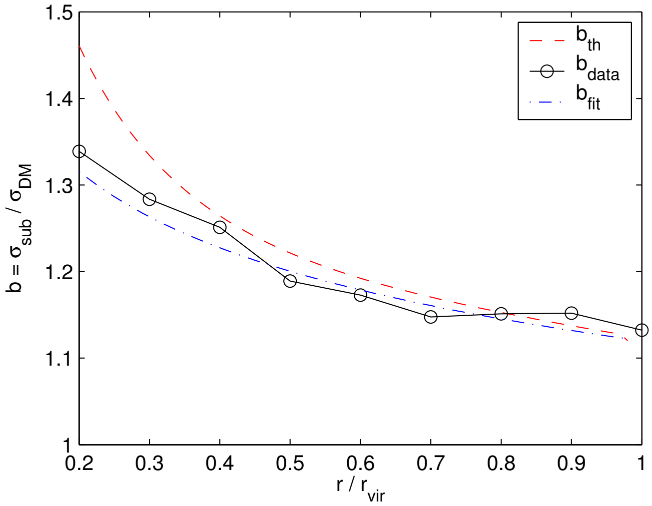

Figure 5.4: Velocity bias profile. Circles give the average bias of the six clusters. The dashed line is the bias calculated from the Jeans equation (5.3) using the different density profiles of subhalos and background particles and assuming that the two are in dynamical equilibrium. The dashed-dotted line gives a simple power law fit $\propto r^{-0.1}$ to the average bias.

In Figure 5.6 we plot the velocity histogram further out (0.5 $r_{\rm virial}$ to $r_{\rm virial}$). Now the second moments of the particle and subhalo velocities are much closer ($b = 1.10$), but the shapes of the velocity distributions of subhalos and particles are still different: $k = -0.60$, $h_4 = -0.031$ and $h_6 = -0.025$. For all subhalos within $r_{\rm virial}$ we find $b = 1.11$, $k = -0.48$, $h4 = -0.034$ and $h_6 = -0.012$.

Both the inner (Figure 5.5) and outer (Figure 5.6) subhalos show an *excess of high-velocity substructures* between $v_{\rm c,max}$ and 1.5 $v_{\rm c,max}$. Many of these high-velocity subhalos are on very radial orbits. When we exclude subhalos with absolute values of the radial velocity component larger than $v_{\rm c,max}$ the excess disappears and the speed distribution follows the Maxwellian distribution of the background particles above $v_{\rm c,max}$. The large fraction of subhalos with very high radial velocities is also evident in the radial velocity distribution (not shown): both in the inner and outer part of the clusters the distribution has a very negative kurtosis of $k = -0.9$. Also note that the radial velocity distributions are symmetric, there is not net infall of subhalos at z=0.

The shape parameters depend weakly on the lower mass threshold, including subhalos above $5 \times 10^{-5} M_{\rm virial}$ instead of 32 m_p yields: $b = 1.11$, $k = -0.44$, $h4 = -0.016$ and $h_6 = -0.022$. There are 979 subhalos above this threshold in our six clusters, which is only $979/12027 = 0.039$ of the $N \geq 32$ subhalo sample, but this is still enough to determine the shape of the velocity distribution. All of these subhalos have bound masses of more than $1.2 \times 10^{10} {\rm M}_{\odot}$.

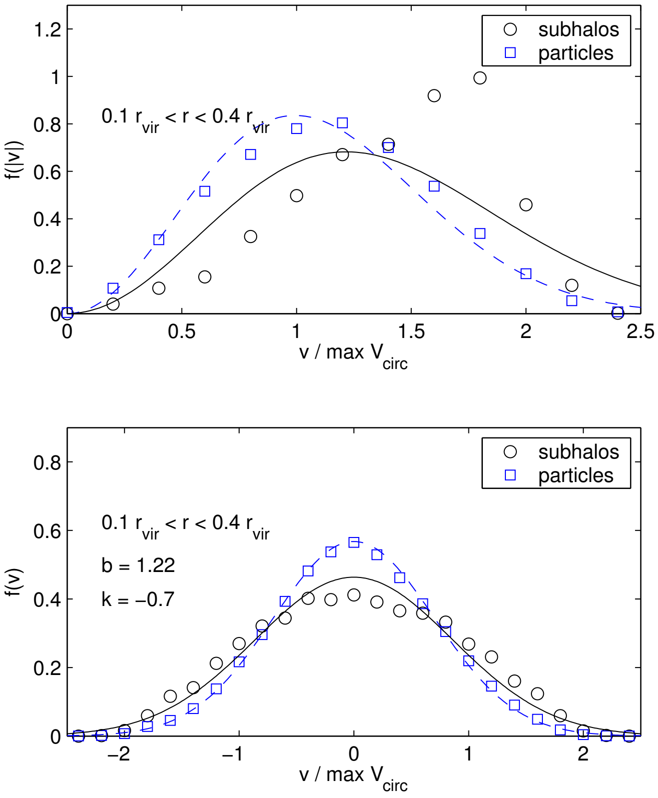

Figure 5.5: Velocity distribution of inner subhalos (circles) and particles (squares). Average of six distributions from different clusters. Subhalos and particles between $r = 0.1 r_{\text{virial}}$ and $0.4 r_{\text{virial}}$ are included. Velocities are normalized to the maximum circular velocity $v_{\text{c,max}}$ of each cluster. Solid and dashed lines are Maxwellian distributions with the correct second moment.

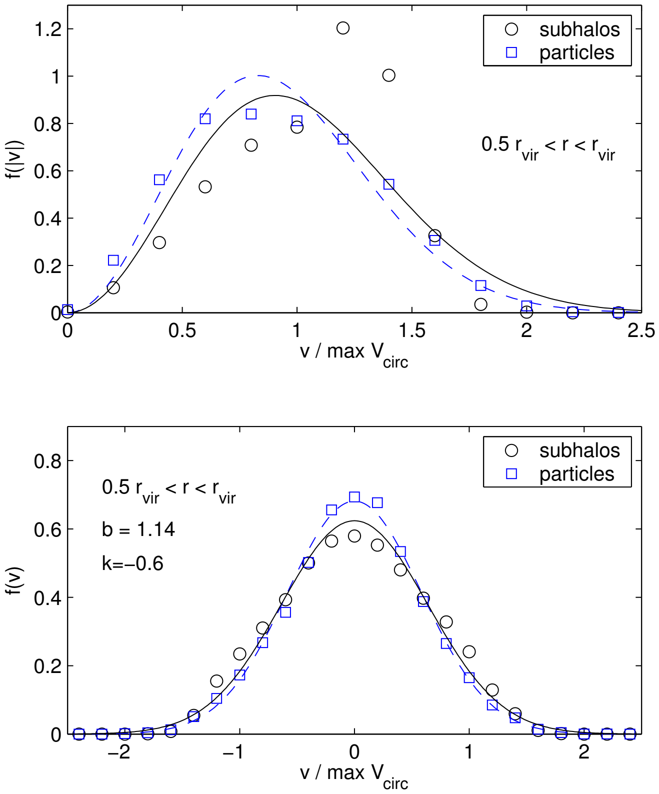

Figure 5.6: Same as Figure 5.5, but including subhalos and particles between $r = 0.5r_{\mathrm{virial}}$ and r_{virial}.

5.4.4 The origin of the subhalo biases

The physical mechanism that generates the differences in the spatial and velocity distributions of particles and subhalos is most likely the tidal destruction of subhalos in dense environments. The efficency of tidal stripping and tidal disruption depends mostly on the orbital energy of the subhalos (Ghigna et al. 1998; Taffoni et al. 2003; Kravtsov et al. 2004). Therefore it offers a natural explanation for the lack of slow subhalos; at a fixed radius the orbital energy is proportional to the square of the velocity and tidal disruption could remove a large fraction of the slow subhalos producing a distribution like the one given in the top panel of Figure 5.5.

The tidal disruption of subhalos must occur very early in the evolution of the cluster. Ghigna et al. (2000) are able to identify the remnants of 60 to 70 percent of all cluster progenitor halos ($N \geq 100$ at z=3) with subhalos at z=0. [3]. From the halos identified at $z = 1$ an even larger fraction survives (more than 80 percent). For run $D6h$ we performed the same test and get very similar numbers. We link progenitor halos with a halo at $z = 0$ if at least four particles of the progenitor are bound to the subhalo at $z = 0$ and find descendents for 83 percent of the progenitor halos identified at z=2.

However a significant fraction of subhalos may have been destroyed prior to this epoch. From the halos with $N \geq 100$ identified in the high resolution region of run $D6h$ at z=7.2 and z=4.3, we can associate only about 60 percent with $z = 0$ subhalos. At this early stage tidal disruption seems to act as a physical selection process which allows only halos with high enough orbital energies to survive as todays subhalos. This causes the spatial antibias and the positive velocity bias of substructure.

Note that it is important to have a larger minimum number of bound particles in the early subhalo sample ($N \geq 100$) than in the final subhalo catalogue ($N \geq 10$) if one wants to quantify disruption: If we would use the same N at both times then we would get a much higher 'disruption rate', but we would mostly measure the amount of subhalos that were tidally stripped below this threshold number of bound particles but not necessarily disrupted. This caveat would have a big influence since about half of the considered subhalos have a bound mass between Nm_p and 2Nm_p.

5.4.5 Comparison with galaxy size halos

The four galaxies in our sample are resolved with 1.7 to 3.8 million particles, so the relative mass resolution is lower than for the clusters. However, there is enough resolved substructure to compare its abundance and the radial distribution to the results from the cluster runs. We make the comparison with cluster $D6h$ which has similar relative mass and force resolution as the galaxies. We also give the results for the same cluster with eight times better mass resolution (run $D12$) to get an impression how the results might change if we also had higher resolution for the galaxy halos. There may be a hint that the galaxies have slightly less substructure than the clusters, but we need to increase the resolution in the galaxy simulations in order to verify this result.

Galaxy G2 had a recent major merger at $z \simeq 0.2$, at $z = 0$ this merger is finished, the core has no more visible signs of dynamical activity. The concentration of this galaxy is lower $c_{\mathrm{vc,max}} = r_{\mathrm{virial}}/r_{\mathrm{vc,max}} \simeq 3.6$, probably due to the later formation in this recent

---

[3] The fraction of subhalos that merge with the central object (i.e., end up within an assumed radius of about 0.015 r_{virial}) are always below 5 percent and can be neglected in this context. But it is an important fraction if one considers the most massive progenitors only (Ghigna et al., 2000).

merger. The other three galaxies had no more major mergers since at least $z \simeq 0.2$ and their $c_{\rm vc,max}$ are between 5 and 6.5.

5.4.5.1 Substructure abundance

Despite the fact that clusters form much later than galaxies in hierarchical structure formation, they have very similar subhalo mass function. Moore et al. (1999a) showed this by comparing two SCDM halos. De Lucia et al. (2004) confirmed this recently for several ΛCDM halos, but at a resolution of less than a million particles inside the virial radius. Figure 5.7 shows the subhalo abundance in the four galaxies and in the cluster D. The velocity functions (Panel a), mass functions (Panel c) and inner mass functions (Panel d) are all quite close to those of the reference cluster run $D6h$.

The substructure abundance is largest in galaxy $G2$, it is as high as in run $D6h$. This halo formed recently in a major merger at $z \simeq 0.2$, which is a typical formation history for cluster size halos rather than for galaxies. The other three galaxies have about 30 percent less substructure than $G2$ and $D6h$. Therefore the amount of substructure depends weakly on the mass of the parent halo, but the difference appears to be comparable to the scatter within parent halos of a fixed mass.

5.4.5.2 Radial distribution

The relative number density profiles (Panel (b) of Figure 5.7) of the galaxy subhalos are more centrally concentrated than those of cluster subhalos (De Lucia et al., 2004). Smaller halos have higher concentrations (Navarro et al., 1996) and are therefore more resistant against tidal disruption. However the subhalo number density also shows a clear antibias with respect to the dark matter density.

The density profile that fits the cluster subhalos distribution (Equation 5.1) is a good approximation also for the galaxy subhalo number density profile. Now the core radius is a smaller fraction of the virial radius ($r_{\rm H} \simeq 0.14\ r_{\rm virial}$) because galaxy subhalos are more centrally concentrated. Note that $r_{\rm H}$ is again about two thirds of the radius where the circular velocity is maximal, this is the same fraction as for the cluster subhalos. Therefore scaled to $r_{\rm vc,max}$ galaxy and cluster subhalos number density profiles are the same.

5.5 Comparison with observations

5.5.1 Substructure abundance

Desai et al. (2004) measured galaxy circular velocity function in 34 low-redshift clusters and found that these functions can be approximated by a power-law $\propto v_{\rm c,max}^{-2.5}$. In CDM cluster simulations they found a logarithmic slope of -3.4 ± 0.8. Our higher resolution simulations show that these slopes are rather on the steep side of the given range, Figure (5.3) shows that the *cumulative* velocity function has a slope of about -3, where we expect the sample to be complete. For the differential circular velocity function this gives a slope of -4, which is not consistent with the observed slope of -2.5. Accounting for the effects of the baryons could reconcile CDM simulations with the observations, see e.g. Springel et al. (2001b) and Desai et al. (2004). Realistic gas-dynamical cluster simulations will eventually resolve this issue.

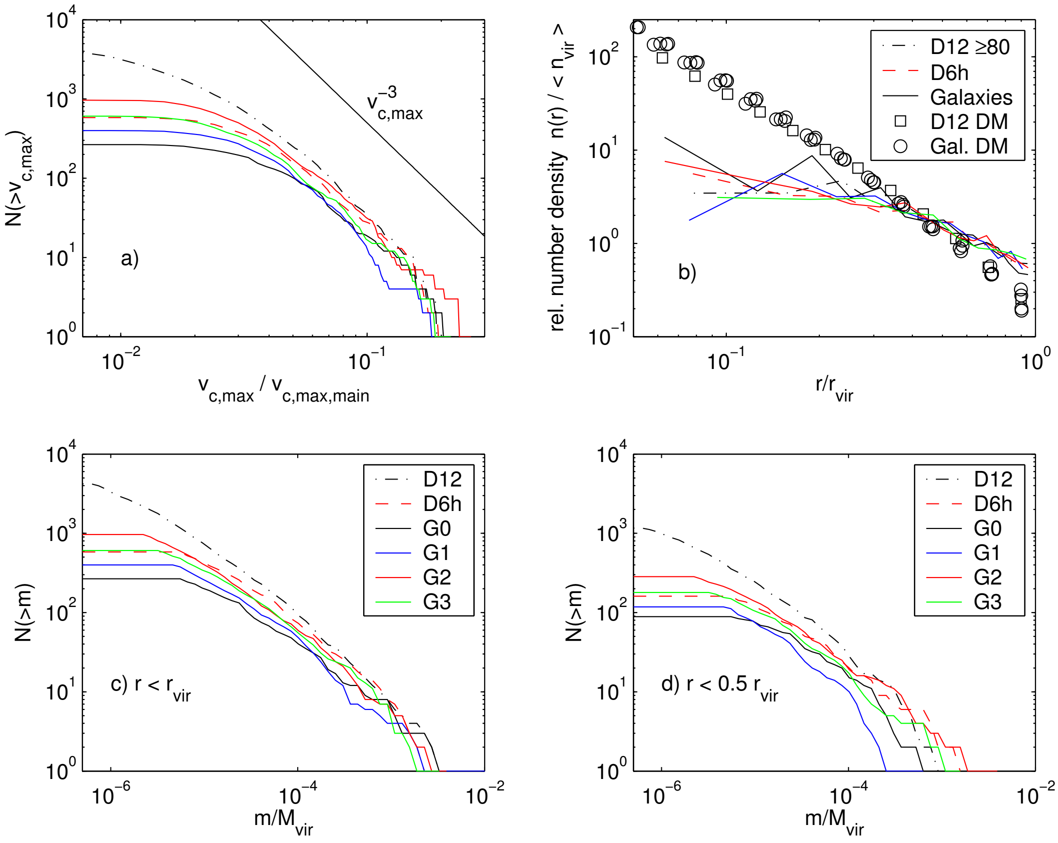

Figure 5.7: Substructure properties of four galaxy halos: Panel a): Cumulative number of subhalos as a function of their circular velocity. Panel b): Relative number density of subhalos and of all DM particles (see Section 5.4.1 for details). Panel c): Cumulative mass functions of substructure within r_{virial}. Panel d): Inner cumulative mass functions, including halos within 0.5 r_{virial}. All halos with at least 10 bound particles are included in these plots. The solid lines show the four galaxies, the dashed line is a cluster halo at similar resolution and the dashed dotted line is the same cluster at eight times higher force resolution for comparison.

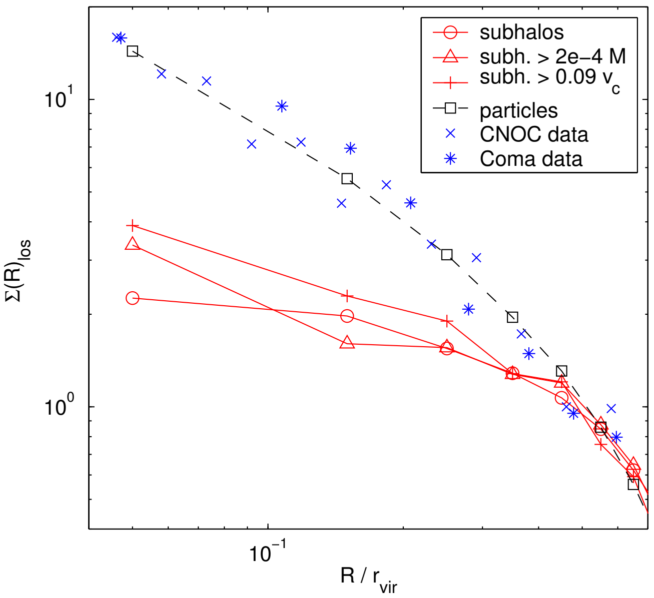

Figure 5.8: Projected relative number surface density profile of subhalos averaged over the six clusters: Circles include all (12'023) subhalos with $N \geq 32$, triangles only halos with $m > 10^{-4} M_{\rm virial}$ and plus signs only halos with $v_{\rm c,max} > 0.09 v_{\rm c,max,main}$. The core of the main halo, the 'cD galaxy', is always included in the first bin. The projected dark matter density is plotted with squares. Crosses are the data from the CNOC survey (Carlberg, Yee & Ellingson, 1997), stars are the Coma cluster data from Lokas & Mamon (2003). We normalise the curves so they match at $r_{\rm virial}$.

The same problem is more severe when the host halo is a galaxy and not a cluster. The steep circular velocity function of CDM halos predicts over 100 subhalos with circular velocities above 5 percent of the parent halo circular velocity, i.e. above 10 km/s for a Milky Way size halo. Our highest resolution cluster $A9$ has over 300 subhalos above this velocity. But the number of Milky Way satellites with $v_{\rm c,max} > 0.05 v_{\rm c,max,parent}$ is only 10 (Moore et al., 1999a). Various solutions to this issue have been proposed in the literature (e.g. Stoehr et. al 2002, Kravtsov et al. 2004).

5.5.2 Spatial distribution

For comparison with observed spatial and velocity distributions of galaxies in clusters we 'observe' the six simulated clusters along three different line of sights (LOS) (the x, y and z axis) and average over these LOS. We then take the sample averages to get mean values and an estimate of the scatter. The results are shown in Figure 5.8 and 5.9.

The number surface density is plotted at the midpoints of equal bins in projected distance from the densest region of the cluster. The innermost bin starts at $R = 0$ and therefore always one additional subhalo, i.e. the core is counted as the cD galaxy of the cluster. The projected number density is flat near the center, just like the 3D number density in Figure 5.2. The total sample contains 12'027 subhalos with at least 32 bound particles from the 6 high resolution clusters. In the Coma cluster a number density profile for a comparable number of galaxies (985) can be measured (Lokas & Mamon, 2003), this profile (plotted with stars in Figure 5.8) is steeper than the subhalo profile and follows rather closely the expected dark matter profile of a CDM cluster. Carlberg, Yee & Ellingson (1997) give the surface density profile of a sample of galaxies combined from 14 clusters observed in the CNOC cluster survey. The sample contains 1150 galaxies, including background and goes out to $2r_{200}$, i.e., per cluster there are about 50 galaxies. Therefore this magnitude limited sample should be comparable to the most massive 300 subhalos in our sample.

We selected the subhalos with $m > 2 \times 10^{-4} M_{virial}$ and get a sample of 238 halos, their surface density profile is plotted with triangles in Figure 5.2. The profile does not change much, just in the innermost bin the values rise, due to the relative importance of the 'cD galaxy'. Selecting subhalos by peak circular velocity $v_{\mathrm{c,max}} > 0.09\ v_{\mathrm{c,max,parent}}$ gives a sample of 291 halos with a similar surface density profile.

The observed number surface density profiles from Carlberg, Yee & Ellingson (1997) and Lokas & Mamon (2003) (and also Beers & Tonry (1986) and Merrifield & Ken (1989)) are significantly steeper than in the CDM clusters. To correct the subhalo number density in the inner four bins upwards to match the observed values one needs to add a number of subhalos similar to the total number within the virial radius of each cluster, but preferentially more subhalos closer to the cluster center. We discuss the implications of this result in the conclusions.

5.5.3 Subhalo velocities

The velocity bias $b \sim 1.12 \pm 0.04$ would lead to dynamical cluster mass estimates that are about 20 percent too high if cluster galaxies reside in CDM subhalos. By comparing with cluster mass estimates from gravitational lensing it could be noted the dynamical estimated are too high, but it is very difficult to obtain estimates with small enough uncertainties with both methods. Such a comparison was performed by Cypriano et al. (2004), finding that dynamical masses are indeed biased by 1.20 ± 0.13 in a sample of 14 clusters, but the effect only comes from the massive clusters ($\sigma_v > 1122$ km/s), which show large mass differences 1.54 ± 0.19, while the smaller clusters show no bias.

Figure 5.9 shows the projected moments of the CDM subhalo velocity distributions and the inner and outer distribution of line of sight velocities averaged. The ploted values are averages over the six cluster halos and over three different projections. The velocity moments for the dark matter background are also plotted for comparison, a similar analysis was presented by Sanchis, Lokas & Mamon (2004).

In contrast to the spatial distribution the *velocity* distribution of CDM subhalos agrees surprisingly well with current observations of cluster galaxies. In the grand total velocity distribution of the CNOC survey a negative $h_4 = -0.015 \pm 0.005$ was found (van der Marel et al., 2000) and $h_6 = -0.028 \pm 0.006$. We get $k = -0.44$, $h4 = -0.016$ and $h_6 = -0.022$ using all subhalos with bound mass larger than $5 \times 10^{-5} M_{\mathrm{virial}}$. There are 1152 subhalos above this threshold in our six clusters. This agreement between simulations and observations may be fortuitous since the spatial distribution of galaxies is different and probably due to destruction of low energy central subhalos. Also, in the Coma cluster the velocity distribution seems to be more flat topped compared to a Gaussian: The kurtosis is negative in most radial bins, the values scatter around $k \simeq -0.5$ (see Figure 3 in Lokas & Mamon (2003)). The uncertainties in the measurement of velocity moment profiles are still quite large and a comparison with the projected moments from Figure 5.9 of the CDM subhalo velocities is not feasible yet.

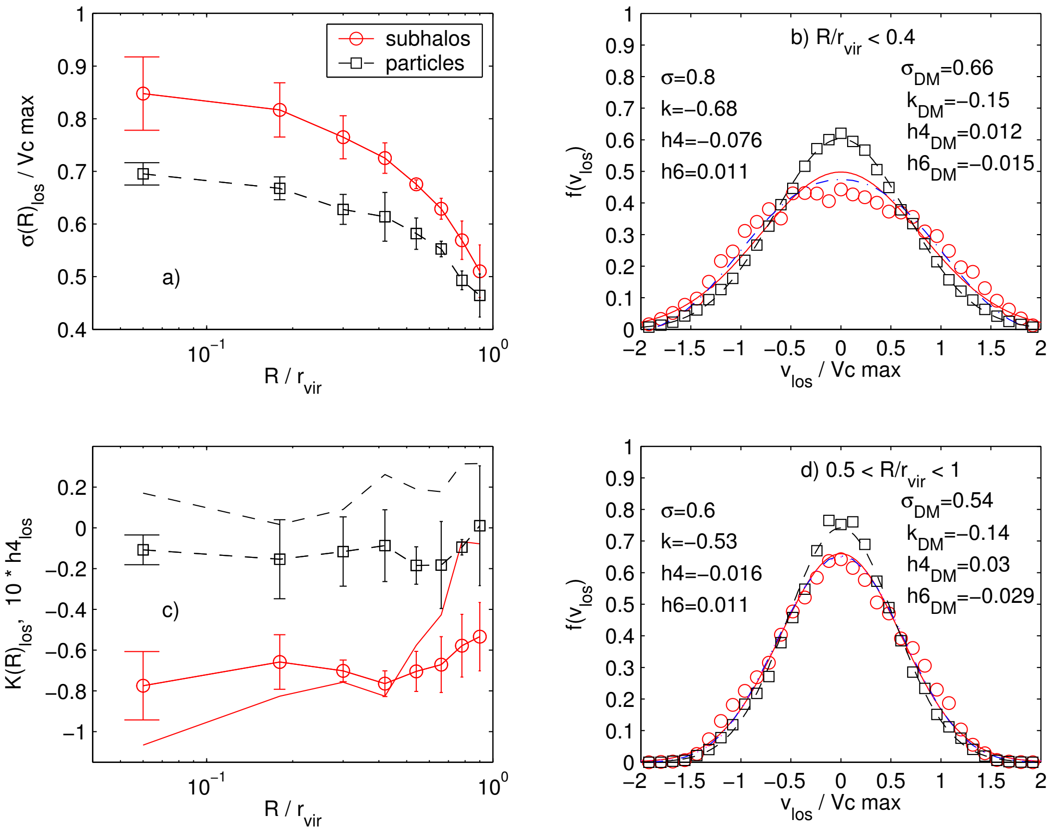

Figure 5.9: Panel a): Average line of sight velocity dispersion of subhalos and particles as a function of projected distance from the center. Panel b) and panel d): Average line of sight velocity distributions of subhalos and particles, for projected radii smaller (b) and larger (d) than 0.4 r_{virial}. Solid and dashed lines are Gaussians with a second moments fitted to the subhalos (solid) and to the particles (dashed). Fourth order Gauss-Hermite approximations to the subhalo velocity distribution functions are given with dashed-dotted lines. Panel c): Average kurtosis (with error bars) and fourth Gauss-Hermite moment (without error bars and multiplied by a factor of ten for clarity) of the line of sight velocity components of subhalos and particles as a function of projected distance from the center. The error bars in panels a) and c) give the scatter within the six clusters.

5.6 Conclusions

We analyse the substructure within six very high resolution cold dark matter simulations of galaxy clusters and four simulations of galaxies. We have addressed several open issues raised in the introduction regarding the results of high resolution simulations of individual halos within the concordance CDM model. Our conclusions can be summarised as follows:

1. The spatial distribution of subhalos in cold dark matter simulations of galaxies and clusters is antibiased with respect to the mass. Although this behavior was found by other groups, we demonstrate that this result is robust and does not change as we increase the resolution. We show that this antibias most likely results from a population of early halos that are tidally destroyed in the dense protocluster environment and within the central regions of the final cluster.

2. The surviving population of subhalos have a positive velocity bias that increases towards the center of the halos. The subhalo velocity distribution functions are non-Gaussian, they are 'flat topped', especially in the inner region: There the kurtosis is $k = -0.7$ and the fourth Gauss-Hermite coefficient $h_4 = -0.068$.

3. The spatial anti-bias and the positive velocity bias of the subhalos are consistent with a steady-state solution of the Jeans equation. Subhalos are a hot, more extended component in equilibrium with the potential generated by the smooth particle background.

4. The mass and circular velocity distributions of subhalos in our highest resolution simulation show the same power law slopes as in lower resolution versions, but are steeper at the low mass end. It is not clear that convergence in the number of subhalos has been reached below a scale of a few hundred particle masses.

5. Cluster and galaxy mass halos simulated at the same resolution have similar substructure abundances. The scatter in the circular velocity and mass functions is a factor of three at the high mass end, but falls to just 1.7 at lower masses.

6. An observational comparison with CNOC cluster data and the Coma cluster shows that the galaxy population traces the smooth dark matter background, but not the predicted halo population. This is most likely due to overmerging in the central region of the simulations and we are probably missing a factor of two in the subhalo population. The baryonic cores of these disrupted subhalos may survive intact if dissipational processes increase their densities sufficiently. Also a greatly truncated dark matter halo may survive in this case.

This latter statement is the most profound conclusion of this work. The spatial distribution of cluster galaxies is significantly different from the distribution of subhalos in dark matter simulations. Either the model is incorrect or we have reached a fundamental limit to this type of pure dark matter simulation. Here we explore the latter possibility and the implications for the morphology density relation.

It is likely that disk galaxies do not significantly modify the overall potential provided by the baryons and dark matter. Whereas a disk-disk merger would funnel gas to the central region, forming an elliptical galaxy with a significantly deeper potential and a effective rotation curve that is at least isothermal, or possibly Keplerian in the center (Romanowsky et al., 2003). Thus we expect that an elliptical galaxy would most likely survive at any position within the cluster, albeit with a greatly truncated dark matter halo. Late type spiral galaxies are unlikely to survive within the central regions of clusters (or their progenitors) and will become physically overmerged to form the cD halo of diffuse light.

If the CDM paradigm is correct then we are missing close to a factor of two of the 'galaxy' population as associated with subhalos, increasing to a factor of five within the inner 10% of the cluster. It is possible that simulations with more than 10^9 particles per system may resolve more central subhalos and calculations this large will be possible in the future. In this case, the velocity bias should decrease as we resolve more halos/galaxies in the central regions. However, from our convergence study we find very few new halos in the central cluster regions as we increase the resolution by a factor of ten. This implies that we have reached a physical limit to DM-only simulations and that any loss of subhalos in current simulations is due to physical overmerging (White & Rees 1978; Moore et al. 1996). In this case progress in this area can only be made by including a realistic treatment of hydrodynamics and star-formation such that realistic disks and elliptical galaxies can be followed within the appropriate cosmological context.

The survival or disruption of a galaxy depends on an intricate balance between the progenitors dark halo structure and the effects of dissipation. Sa-Sb galaxies must lie on the borderline between survival and disruption in the cluster environment. The morphology-density relation may simply reflect the fact that the disks are preferentially destroyed in the central regions of clusters. However if the CDM model is correct one needs to preferentially form ellipticals in high density regions before the cluster forms. The fact that the observed galaxy distribution follows the dark matter distribution implies that no overmerging of galaxies has taken place. It is insufficient to take disks and destroy them in the cluster cores since this would give rise to a cored galaxy distribution.

The fact that 40% of halos identified at z=7 can not be associated with a subhalo at z=0, or have not merged with the central cD, implies that they have merged into the smooth particle background. If these objects can be associated with surviving galaxies, it implies a strong age-radius dependence for galaxies within clusters. At the cluster centres over 80% of the galaxies must have formed prior to z=7.

Acknowledgments

We thank the referee for many insightful comments and suggestions. We are grateful to Ewa Lokas for kindly providing the galaxy number density data for the Coma cluster and to Frank van den Bosch, Chiara Mastropietro, Peder Norberg and Jeremiah Ostriker for useful discussions. We thank the Swiss Center for Scientific Computing in Manno for computing time, we generated the initial conditions there. The simulations were performed on the zBox [4] supercomputer at the University of Zurich. J. D. is supported by the Swiss National Science Foundation.

---

[4] http://www-theorie.physik.unizh.ch/∼stadel/zBox/

Chapter 6

Evolution and orbital history of CDM subhalos [1]

6.1 Abstract

We explore the region of influence of a galaxy cluster using numerical simulations of cold dark matter halos. Many of the observed galaxies in a cluster are expected to be infalling for the first time. Half of the halos at distances of one to two virial radii today have previously orbited through the cluster, most of them have even passed through the inner half of the cluster. Some halos at distances of up to three times the virial radius have also passed trough the cluster core earlier. We do not find a significant correlation of "infall age" versus present day position for substructures and the scatter at a given position is very large. This relation may be significant if we could resolve the physically overmerged galaxies in the central region.

6.2 Introduction

Are the morphologies of galaxies imprinted during an early and rapid formation epoch or are they due to environmental processes that subsequently transform galaxies between morphological classes? The gravitational and hydrodynamical mechanisms that could perform such transformations were proposed in the 1970's, before the key observational evidence for environmental dependencies was provided - the morphology-density relation and the Butcher-Oemler effect. Many recent numerical simulations support these theoretical expectations. However, until we have self-consistent numerical simulations that can follow the structural evolution of galaxies within a large computational volume, we must resort to semi-analytic treatments or to studying the evolution of galaxies within idealised numerical calculations.

In this paper we study the orbits and infall history of substructure halos within a cold dark matter galaxy cluster. When we observe a cluster today we see a single frame of its entire cosmic evolution. What we would like to know is for a given galaxy at a given position, what is its likely orbit? Is it infalling for the first time? What are the environments that may have post-processed the galaxy? If it has already passed pericenter

---

[1] These results were presented at the IAU conference "The outskirts of galaxy clusters", Torino, March 2004 and published in the conference proceedings (Moore et al., 2004).

at what epoch did it enter a cluster-like environment? What was its impact parameter and velocity with respect to the cluster center? Are clusters built up in an “onion shell” scenario such that the observed galaxies trace an age-radius relation? We shall use the largest and highest resolution calculations of cold dark matter galaxy clusters to address some of these questions. With up to 62 million particles in the high resolution region, up to 25 million particles within the virial radius and high force resolution we can resolve the orbital histories of many thousands of substructures and halos in the outskirts of a cluster. Related studies have been carried out recently: Balogh, Navarro, & Morris (2000) followed *particle* orbits in N-body simulations while Mamon et al. (2004) used analytical calculations and the $z = 0$ snapshots of simulations to estimate rebound radii. Very recently (a couple of weeks after this meeting) other groups (Gill, Knebe, & Gibson 2004; Gao at al. 2004a) have published results that were also obtained by following *subhalo* orbits and their results are very similar to those presented here.

6.3 Accretion redshift of cluster subhalos

It is interesting to know how much time todays cluster galaxies spent in dense environments and if the accretion time into a more massive halo is correlated with the current position in the cluster. One could expect that subhalos which fell into the cluster (or one of it progenitors) early have less orbital energy and tend to end up closer to the cluster center. We analyze the redshift of accretion of cluster subhalos in ΛCDM simulations. Note that as accreted structures we count both subhalos of the final cluster and subhalos of the cluster progenitor groups.

We take 20 outputs of run D6h and 10 of run C9, equally spaced in time. The simulations are described in Diemand et al. (2004c) and the properties of their subhalos are presented in Diemand et al. (2004b). Run C9 resolves a $M_{\mathrm{virial}} = 5.0 * 10^{14}\mathrm{M}_{\odot}$ cluster with 10 million particles within r_{virial} and D6h resolves a smaller $M_{\mathrm{virial}} = 3.1 * 10^{14}\mathrm{M}_{\odot}$ cluster with 2 million particles.

The subhalos were identified with SKID (Stadel, 2001) and here we consider only structures with at least 32 bound particles. For each snapshot we construct a halo catalogue with FOF using a comoving linking length of 0.164 Δx_0 and trace back in time all subhalos within the virial radius of todays cluster. In Figure 6.1 the redshift before accretion is plotted, that is the last time a halo is identified as individual field halo. There is a large scatter in the accretion redshifts and no strong correlation with radius.

From the scatter plot and also from the histogram of accretion redshifts in three radial bins (Figure 6.2) one can see that the accretion rate is not a simple function of time but there are epochs of very rapid or of very slow accretion. Both clusters show very little accretion around redshift 0.4, which seems to be a coincidence.

The inner subhalos were accreted slightly earlier on average, in run D6h the mean and standard deviation of expansion factors at accretion is $a = 0.59 \pm 0.14$ for subhalos that end up in the inner 33 percent of the cluster and $a = 0.80 \pm 0.16$ for the outer 33 percent. For run C9 however all three radial bins give a mean of about $a = 0.7$. More halos must be analyzed to see if there really is a correlation of accretion redshift with cluster-centric radius, but we can already say that such a correlation must be weak and have a very large scatter.

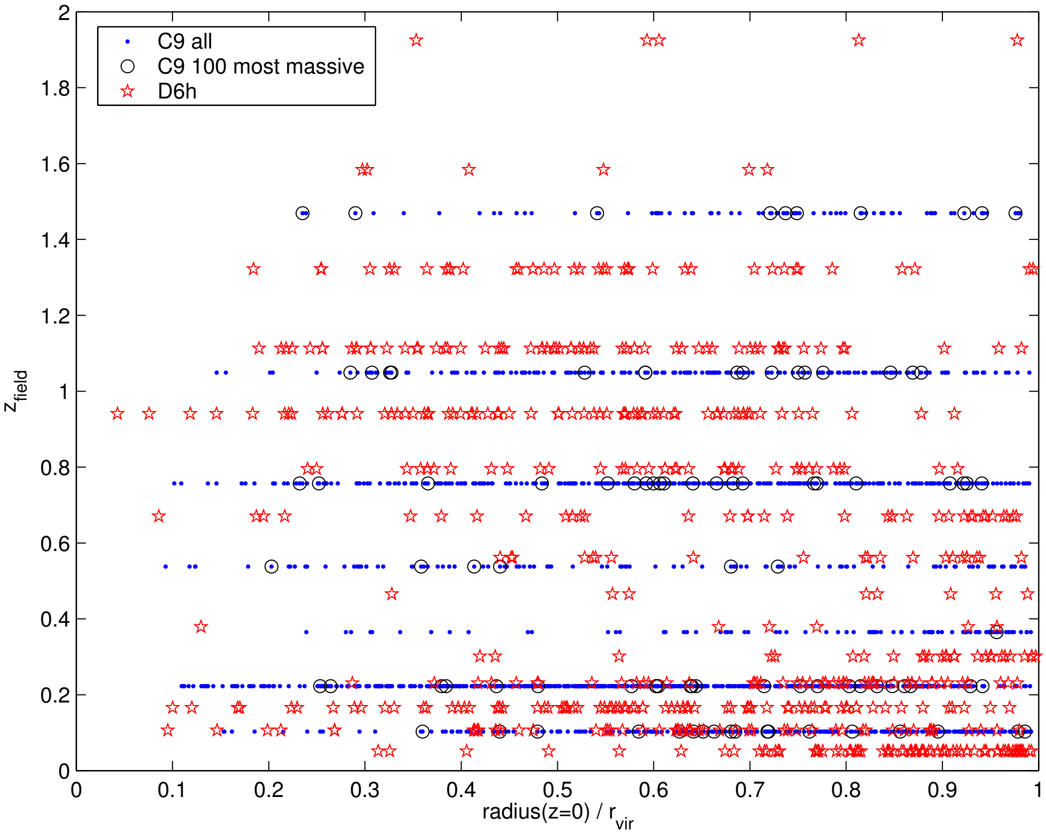

Figure 6.1: Accretion redshift of subhalos in two high resolution ΛCDM cluster simulations (*D6h* and *C*9) versus distance form the cluster center today. We plot the redshift of the snapshot where a halo was identified as an individual field halo for the last time. The trend that central subhalos spent more time within the cluster is weak and the is a large scatter in accretion redshifts at all radii.

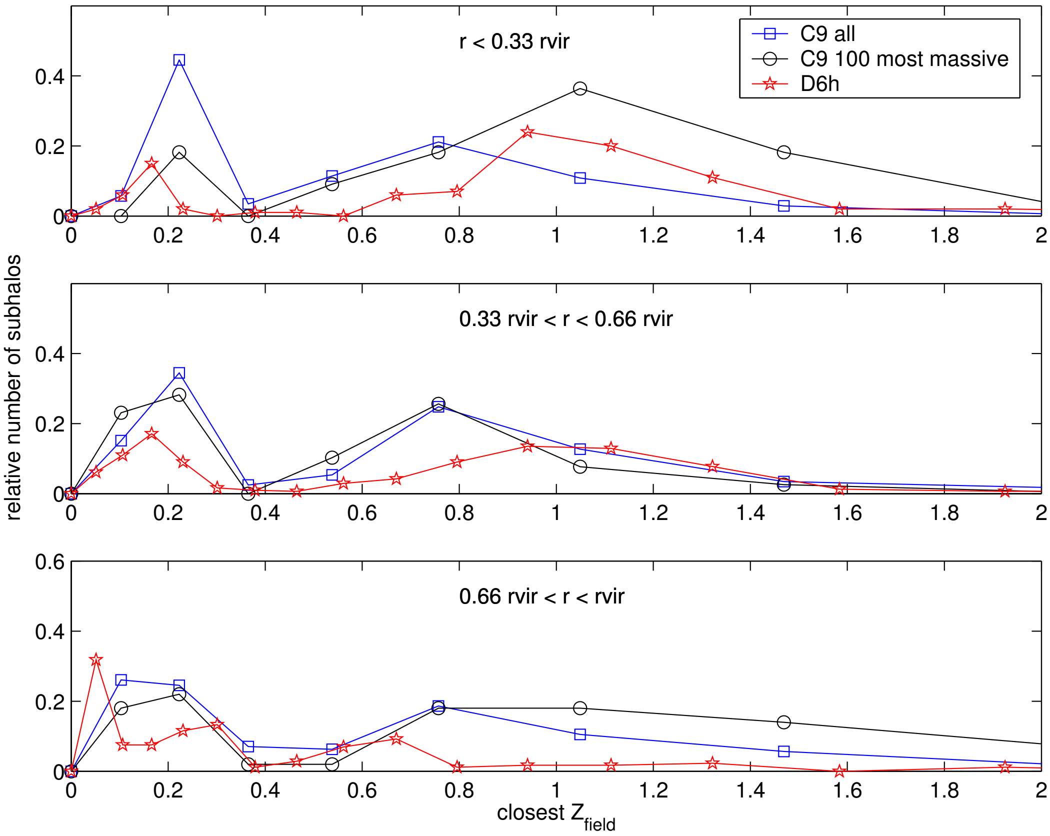

Figure 6.2: Histograms of accretion redshifts of subhalos in two high resolution ΛCDM cluster simulations (*D6h* and *C9*, same data as in Figure 6.1). The top, middle and bottom panels correspond to the inner, intermediate and outer regions of the two clusters.

6.4 Pericenters of halos in the outskirts of clusters

How many galaxies in the outskirts of clusters have passed trough the inner, hot dense part of the cluster and how many are approaching the system for the first time? This question is interesting since some spiral galaxies in the outskirts of the Virgo cluster are observed to be deficient in neutral Hydrogen. First attempts to answer this questions include tracing back *particles* in cosmological Nbody simulations (Balogh, Navarro, & Morris, 2000) and analytical, spherical infall and rebound calculations (Mamon et al., 2004).

We traced back all subhalos and halos around the cluster D6h and measured the distance to the cluster core going back to the formation epoch of the cluster (z$\simeq$0.6). The interval with a time resolution of 0.6 Gyrs.

Figure 6.3 shows the pericenter distance of the (sub)halos versus cluster-centric distance today. The points on the diagonal are halos that have their pericenter at z$\simeq$0, the halos just below the diagonal in the upper right corner of the Figure are orbiting two satellite groups a distances of about 2 $r_{\rm virial}$. In the lower left corner ($< r_{\rm virial}$) we see todays subhalos. For ($r > r_{\rm virial}$) there is a large population of halos that have pericenters well within the cluster. These are halos in the outskirts of the cluster which have passed through the cluster earlier. About half of the halos between $r_{\rm virial}$ and 2 $r_{\rm virial}$ have a pericenter smaller than $r_{\rm virial}$. Most of them (at least 70 percent [1]) have even passed through the inner part of the cluster ($r < 0.5 r_{\rm virial}$). Finally the points in the lower right part of the plot show that in some rare cases halos that passed through the cluster can rebound out to 3 $r_{\rm virial}$, which is a little larger than the maximal distance of 2.5 $r_{\rm virial}$ obtained from analytical, spherical infall and rebound calculations (Mamon et al., 2004).

6.5 Spatial distribution of subhalos

Ghigna et al. (1998) showed that the spatial distribution of subhalos is antibiased with respect to the mass. Diemand et al. (2004b) confirmed that this was not a resolution effect but most likely due to physical overmerging of dark matter halos as they entered the central cluster region. In order to reproduce the observed spatial distribution of galaxies (see Figure 5), dissipation is likely to play a key role (Gao at al., 2004b). It is not expected that dissipation will greatly alter the internal structure of galactic halos hosting disks with type later than Sb. These galaxies will suffer the same fate as the infalling subhalos and become tidally disrupted by the cluster environment. This immediately leads to the morphology-density/radius relation since only ellipticals and Sa/Sb galaxies can survive near the cluster centre. Ellipticals will be especially dense since the multiple merging of gas rich proto-galaxies will undoubtedly lead to strong gas inflow into the central regions. The gas will rapidly be stripped from the central Sa/Sb galaxies, combined with a moderate amount of disk heating from tides these galaxies will rapidly turn into S0's. However it is hard to distinguish this scenario from one which disk formation is suppressed within the proto-cluster environment.

---

[1] Note that in the inner part of the cluster the dynamical times become comparable to the interval between outputs, so the real pericenters will be smaller.

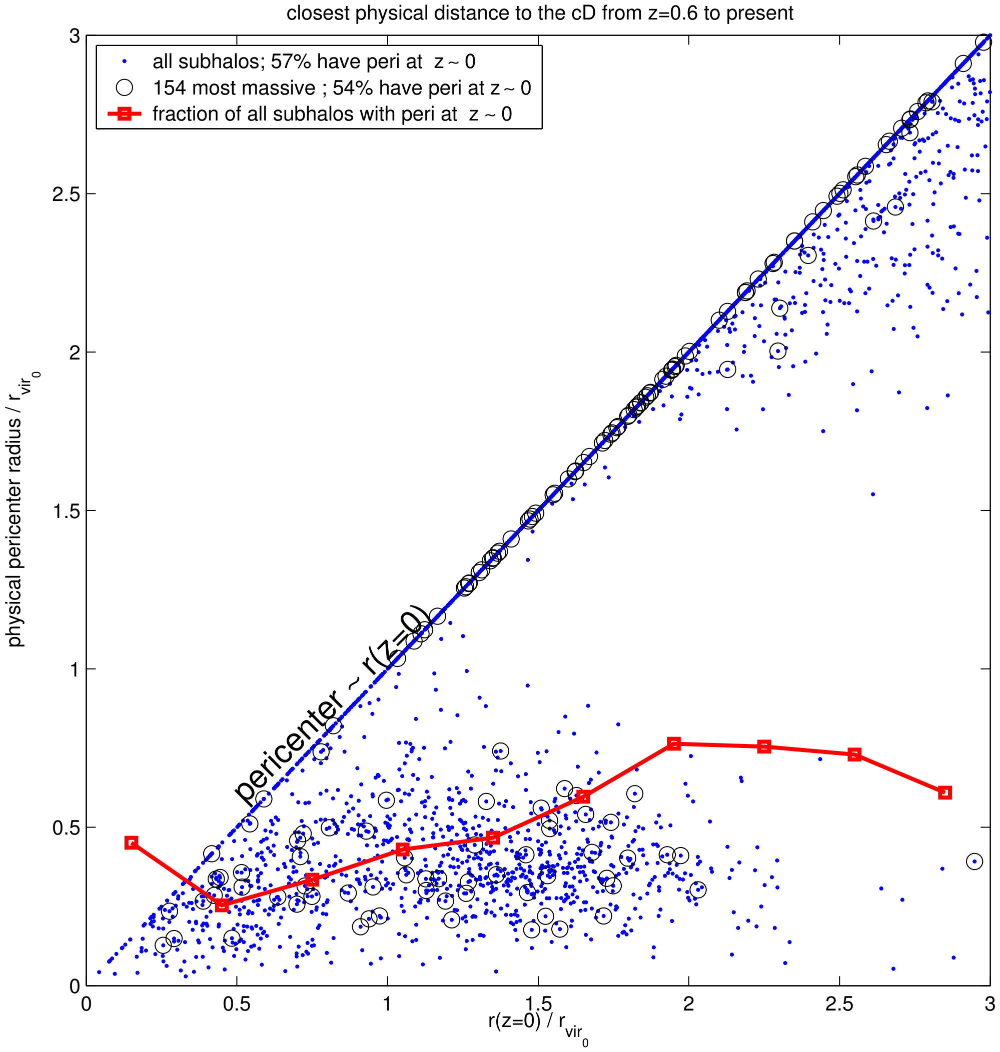

Figure 6.3: Closest physical distance to the cluster center form z=0.6 to present vs. distance form the cluster center today. The red line gives the fraction of (sub)halos that have their pericenter today (within the time resolution of 0.6 Gyrs). The points in the lower right corner show that many halos well outside the cluster today passed deep through it earlier.

6.6 Conclusions

- The average accretion redshift of subhalos does not change significantly with the final time cluster-centric distance, i.e. there is no strong age-radius correlation in ΛCDM *subhalos* (however this does not exclude an age-radius correlation for *cluster galaxies*, sincuhe they do not trace the subhalos in a simple one-to-one correspondence: the subhalo number density profile are much shallower).
- About 50 percent of the galaxies that have a distance between one and two virial radii form the cluster center today have passed trough the cluster earlier.
- Most of them (at least 70 percent) even approached the cluster center to less than half of the virial radius.
- There are some (rare) cases where a halo passes trough the inner part of the cluster and then rebounds out to three virial radii.
- Dissipation must play an important role in enabling galaxies to survive in the central cluster regions. The morphology-density relation may be due to the disruption of disks at the cluster centre.

Chapter 7

The first dark matter halos in a SUSY-CDM model [1]

7.1 Abstract

We simulated the formation of the first, smallest dark matter halos that form in a SUSY-CDM model. The micro-physics of the weakly interacting massive particles (WIMPs) leads to a sharp cut-off in the power spectrum, which depends on the WIMP mass and other SUSY parameters and lies at about $10^{-6}\mathrm{M}_{\odot}$ for a 100 Gev particle. The abundance of these minihalos lies in a range obtained by extrapolation of the well known mass function on galactic scales with a slope of $\alpha = -1$ down to $10^{-6}\mathrm{M}_{\odot}$. The internal properties of the minihalos are not well resolved yet ($N_{\mathrm{virial}} \simeq 1000$) but in the resolved range the resemble rescaled versions of galactic halos. Their very high mean densities could enable them to survive as substructures in the Milky Way halo. In this case there would be a huge local number density of minihalos and the closest minihalos could be detected as point sources in the γ-ray signal from SUSY-CDM annihilations.

7.2 Introduction

Is is now well established that most of the mass of the universe must be a non-baryonic dark matter particle that remains undetected in laboratory experiments (see Chapter 1). The leading candidate for this dark matter is the neutralino, the lightest super-symmetric particle which is predicted to solve several key problems in the standard model of particle physics. This cold dark matter candidate can collide with baryons thus revealing its presence in laboratory detectors, although the cross-section for this interaction is extremely small (see Eidelman et al. 2004 and references therein). The neutralino is its own anti-particle and it can annihilate creating a shower of new particles including high energy gamma-rays. The flux of the pair annihilation goes as the density squared therefore we search at the center of the galactic halo for the strongest signal (e. g. Calcaneo-Roldan & Moore 2000; Stoehr et. al 2003; Koushiappas, Zentner & Walker 2004; Bertone et al. 2004; Prada et al. 2004).

The scale invariant spectrum of fluctuations predicted to emerge from the inflationary big bang matter model is confirmed by the observational data on scales from $1 - 1000$

---

[1] The content of chapter will be published in Nature 2005.

Mpc (see Chapter 1). Large N-body simulations have resolved the large scale structure on these scales (Jenkins et al. 2001; Reed et al. 2003a; Chen et al. 2004) and the internal structure of individual halos (see Chapters 3, 4 and 5) down to scales of about a few kpc.

On very small scales of about one parsec the spectrum of fluctuations is completely smooth due collisions and free streaming. The neutralino is created with a finite velocity which enables it to move away from the smallest overdensities, erasing all signatures of fluctuations on smaller scales (Green et al., 2004).

Here we report new supercomputer calculations that follow the growth and gravitational collapse and virialisation of the first structures in the cold dark matter model. We use a multi-scale technique (e.g. Bertschinger 2001) in order to achieve the desired resolution within two small patches of the universe which are nested within a succession of lower and lower resolution grids of particles.

7.3 Numerical experiments

Table 3.1 gives an overview of the simulations we present in this Chapter, Figure 1.7 shows the dark matter density on different scales in run A. The input power spectra are for the SUSY models with label "A" in Green et al. (2004), in this model the WIMP mass is 100 Gev, the various sfermion masses are assumed to be equal and they are 200 Gev. Due to collisional damping and free streaming there is an exponential cutoff in the power spectrum at a comoving scale of 0.61 parsec. For comparison we also run a simulation without this cutoff (run "*And*"). We use a small box with a comoving size of $L = 3$ kpc containing 100^3 low resolution particles and a refine a region of 0.06^3 kpc by a factor 100^3 in mass to reach a mass resolution of $9.84 \times 10^{-10} \mathrm{M}_{\odot}$. The high resolution region is surrounded by 3 shells of decreasing resolution to reduce the mass differences between neighboring regions. We selected an average density region (runs A and And) and a low density region (run V) for resimulation at high resolution. In the average density runs there are of course more halos, but there is also much more mixing with heavier low resolution particles, since this cube gets quite distorted due to the collapse of fluctuations above the cube size. Therefore we did run these simulations only to redshift 26. The low density region expands faster than the background and does not mix with the surrounding material, we followed the evolution of the minihalo properties up to a redshift of 2, but there are only a few minihalos and one has to bear in mind that they are not a representative sample: Due to the low density environment they form later and are less concentrated. The refined initial conditions were generated with the GRAFICS2 package (Bertschinger, 2001). The simulations have been performed using a new version of PKDGRAV, written by Joachim Stadel and Thomas Quinn (Stadel, 2001).

7.4 CDM minihalo profiles

Our simulations resolve the smallest halos with about 1000 particles, this is by far not enough to measure their inner density profiles. The profiles are affected by numerical flattening mostly due to two body relaxation at about 2 mpc. The limitations due to finite force and time resolution would lie below 0.5 mpc. Figure 7.1 shows the density profiles of three typical halos in run A at redshift $z_f = 26$. Like on cluster and galaxy scales, halos that have just formed have density profile which roughly follow one power

Table 7.1: Parameters of simulation volumes. The input power spectra for the SUSY models are taken form model A in Green et al. (2004), Run *And* has the same spectrum but without the cutoff (no damping). $n_{HR}(N > 144)$ is the number of halos in the high resolution region which contain more than 144 particles.

Run	z_i	z_f	ϵ_0 [mpc]	$\epsilon_{\max}$ [mpc]	m_p $10^{-10}[\mathrm{M}_\odot]$	$\rho_{HR}/\bar{\rho}(z_i)$	$n_{HR}(N > 144)$
A	363	26	3.0	30	9.8	1.017	33 (at z=26)
And	363	26	3.0	30	9.8	1.017	358 (at z=26)
V	363	2.1	3.0	30	9.8	0.753	2 (at z=9)

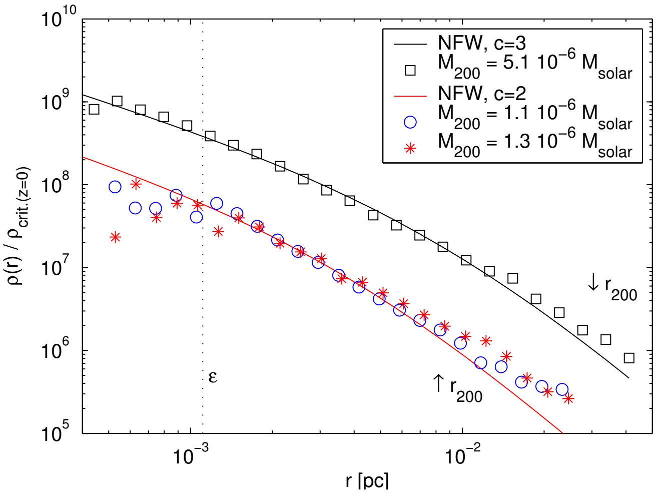

Figure 7.1: Density profiles of three typical minihalos at redshift 26 in physical units with low concentration NFW profiles for comparison.

law $\rho(r) \propto r^{-\gamma}$, with $\gamma \simeq 1 - 2$ (Tasitsiomi et al., 2004). This single power law shape is similar to a very low concentration NFW profile, which we plotted in Figure 7.1 for comparison. Note that the densities at r_{200} are very high, about an order of magnitude above the density at $0.01 r_{\mathrm{virial}}$ in a galactic halo today, which makes the survival of many of these halos as galactic substructure possible (see Section 7.6.1).

Figure 7.2 shows the concentrations c_{vc} of the halos in run *A* at redshift $z_f = 26$. We measured the position of the maximum in circular velocity $r_{\mathrm{vc,max}}$, and calculate the concentration with $c_{vc} = 2r_{200}/r_{\mathrm{vc,max}}$. For halos that follow an NFW profile this concentration is the same as $c_{NWF} = r_{200}/r_s$ defined with the scale radius of the NFW profile.

At this early epoch (z=26) some halos, for example the two small halos in Figure 7.1, have a density profile shallower than r^2 at all radii, i.e. they have no peak in the circular velocity. In these cases we set $r_{\mathrm{vc,max}} = r_{200}$ and get $c_{vc} = 2$. Most halos have concentration between 2 and 4, which are typical for structures that just formed (e.g. Zentner & Bullock 2003; Tasitsiomi et al. 2004). There is no evident mass dependence, which is due to the very similar formation time of all these halos. Above the cutoff scale

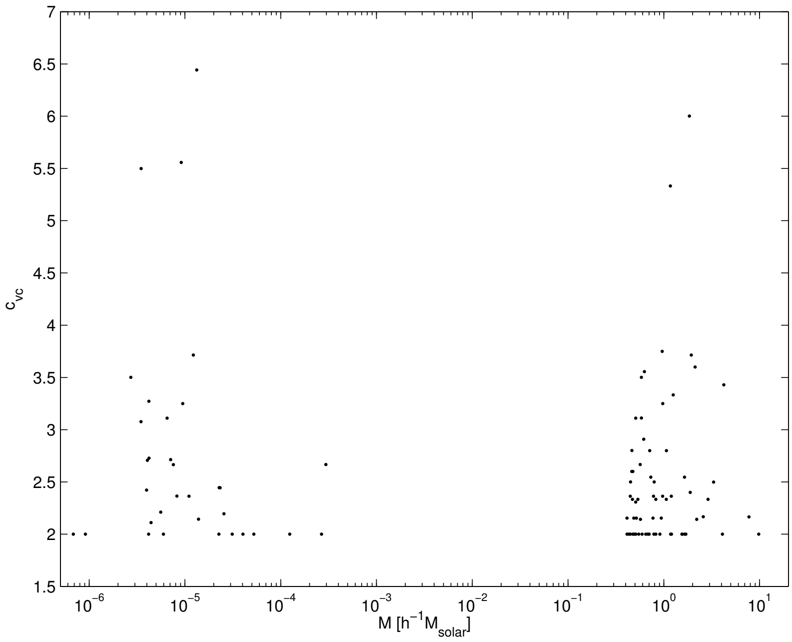

Figure 7.2: Concentration of the halos in run A at redshift $z_f = 26$. Most halos have values from 2 to 4, which are typical for structures that just formed. There is no evident mass dependence.

the power spectrum on these mass scales is close to $P(k) \propto k^{-3}$, which leads to very similar formation times over the whole mass range. The expected scaling of concentration with redshift is $c(z) \propto 1/(z+1)$ (e.g. Zentner & Bullock 2003; Tasitsiomi et al. 2004), this gives z=0 concentrations between about 54 and 108 for most minihalos.

7.5 Mass function

We use the standard friend-of-friends (FOF) algorithm to identify overdense regions. With the usual linking length of 0.2 dx_0 entire filaments in the high resolution region are linked together, therefore we choose a smaller linking length of 0.1 dx_0, which corresponds to an overdensity of 1000. To exclude border effects we discard groups that contain heavier particles from the low resolution regions and also all groups that contain more than 50 percent in mass as low resolution particles within a 3 pc sphere. From the center of mass of each group we make spherical bins that go out four times further than the group size estimated with FOF to find r_{200}, the radius that encloses a mean density of 200 times the matter density at this epoch[1]. The virial mass $M_{\rm virial}$ is defined as the mass enclosed in r_{200}. Groups with $M_{FOF} > M_{\rm virial}$ were also deleted, since they correspond to parts of filaments that have not yet collapsed along the third dimension. This eliminates just a small fraction of the halos, due to the small linking length of 0.1 dx_0 that we used.

From Figure 7.3 it is clear that the halo mass functions are steep ($\propto M^{-1}$) down to the cutoff mass scale of about 10^{-6}M$_\odot$. For comparison we plotted (dashed line) an extrapolation of the galactic scale mass function form Reed et al. (2003a) with a low mass slope of -1. Similar slopes have been found by Chen et al. (2004) who resolved halos

---

[1] Also in the currently favored ΛCDM cosmology which we adopted here there is almost no difference between the matter density and the critical density at z=26.

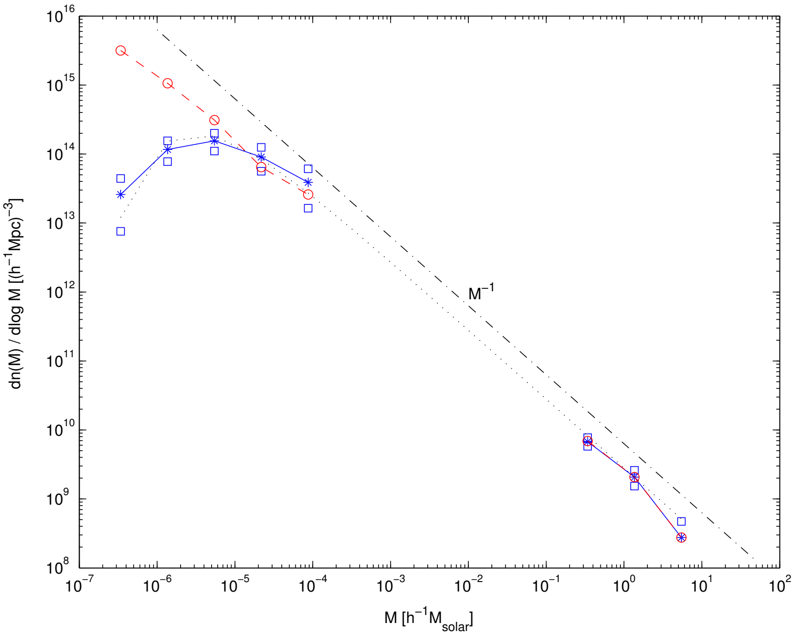

Figure 7.3: Mass functions of runs A (solid line) and And (dashed) in comoving units. Run And (no cutoff in the power spectrum) has a steep mass function down to the resolution limit whereas run A (with a SUSY-CDM power spectrum) has much less halos below a mass of about $5 \times 10^{-6} h^{-1} \mathrm{M}_{\odot} = 3.5 \times 10^{-6} \mathrm{M}_{\odot}$. Our simulations do not probe the mass range form about $3 \times 10^{-4} h^{-1} \mathrm{M}_{\odot}$ to $2 \times 10^{-1} h^{-1} \mathrm{M}_{\odot}$. The dashed-dotted line shows an extrapolation form todays number density of galaxy halos (from Reed et al. 2003a) assuming $dn(M)/d\log M \propto M^{-1}$. The dotted line is the function $dn(M)/d\log M = 2.8 \times 10^{9} (M/h^{-1}\mathrm{M}_{\odot})^{-1} \exp[-(M/M_{\mathrm{cutoff}})^{-2/3}](h^{-1}Mpc)^{-3}$, with a cutoff mass $M_{\mathrm{cutoff}} = 5.7 \times 10^{-6} h^{-1} \mathrm{M}_{\odot}$. The power spectrum cutoff is $P(k) \propto \exp[-(k/k_{fs}]^{2})$, assuming $k \propto M^{-1/3}$ motivates the exponent of $-2/3$ in our fitting function.

down to about $10^{6.5}\mathrm{M}_\odot$. Such a steep mass function means that in each decade in halo mass down to the cutoff scale there is a similar amount of bound mass. Of course bigger simulation volumes for both the low resolution and the high resolution regions would be important to confirm this first result and to probe also later epochs.

7.6 Minihalo detection

The halo masses we discuss here are well below the Jeans mass of the intergalactic gas at all cosmological epochs, therefore the baryons in these halos will not be able to cool and form dense, compact object in the cores. A detection is only possible via gravitational effects (e.g. lensing, disturbance of the planetary orbits in the solar system) or more probable via γ-rays from dark matter particle annihilations.

7.6.1 Number of minihalos in the Wilky-Way

All the detection possibilities we discuss here only work if minihalos can survive in a large number as substructures within galactic halos. Simulations of a galactic halo with enough particles to resolve $M = 10^{-6}\mathrm{M}_\odot$ subhalos would require 10^{20} particles, that is ten orders of magnitude above the possibility of todays supercomputers. However one could simulate the evolution of a few very small halos which were put into a galactic potential "by hand". Similar tests have been performed for dwarf galaxy subhalos and the results agree quite well with the simple tidal approximation: Material that lies within the tidal radius remains bound to the subclump, matter further out gets "tidally stripped". The tidal radius is approximated with the distance form the subhalo center to the inner Lagrange point of the rotating two body system.

For two isothermal spheres the tidal radius is $r_T = \sqrt{1/2}Rv/V$, where R is the distance to the galactic center, V is the (constant) circular speed in the galactic potential, v is the circular velocity in the subhalo and we assumed $v << V$. For the Milk Way we use $V = 220km/s$, the smallest minihalos have $v \simeq 1m/s$ and $r \simeq 0.01pc$. We get $r_T = 3.2 \times 10^{-6}R$. Our distance from the galactic center is about 8 kpc, $r_T = 0.026pc > r$. This suggests that an $10^{-6}\mathrm{M}_\odot$ clump can survive without loosing a large fraction of his mass in the galactic potential at distances of more then about 3 kpc from the galactic center.

Down to dwarf galaxy scales the faint end slopes of field halo and subhalo mass functions agree $dn/d\log M \propto m^{-1}$ (e.g. Reed et al. 2003a, Diemand et al. 2004b). Our simulations indicate that the field halo mass function continues with about the same slope down to the smallest structures. We will now assume that the same holds for the subhalo mass function: For a Milky Way halo $M = 10^{12}\mathrm{M}_\odot$ we get the huge number of $N(> 10^{-6}\mathrm{M}_\odot) \simeq 5 \times 10^{15}$. The number density at our position in the Milky Way halo ($R \simeq 0.04R_{virial}$) is further increased by about a factor of 5, we estimate that the local cumulative number density of subhalos is $n(> 10^{-6}\mathrm{M}_\odot) \simeq 0.4pc^{-3}$.

7.6.2 Gravitational lensing

Compact objects in the mass range considered here could produce a micro-lensing signal in lensed double quasar light curves (Schmidt & Wambsganss, 1998). The source radiation from a quasar must be lensed by a foreground galaxy to produce multiple images. Small clumps in the halo of the lensing galaxy can then produce time varying flux differences between the multiple quasar images. But the suggested mechanism works only for compact objects which are smaller than the Einstein radius. For a point mass this radius is (Schmidt & Wambsganss, 1998)

$$r_E = 3.7 \times 10^{16} \sqrt{\frac{M}{h\mathrm{M}_\odot}}\ \mathrm{cm} \quad . \tag{7.1}$$

For a $10^{-6}\mathrm{M}_\odot$ halo this would be about $r_E \simeq 10{-}7$ pc, which is much smaller than the size of these minihalos (a few mpc). Note that Formula (7.1) is only valid for point masses, using singular isothermal spheres for the lensing minihalos we found even smaller Einstein radii. Also the higher mass halos (around 10 $\mathrm{M}_\odot$) are still not concentrated enough to produce a micro-lensing signal. For sources closer than quasars the Einstein radii become smaller.

To explain the observed anomalous flux ratios in gravitational lenses one would need more massive subhalos then the ones studies here, this effect is an interesting probe for the mass range above at least $10^4\mathrm{M}_\odot$ (e. g.Mao & Schneider 1998; Metcalf & Madau 2001; Dalal & Kochanek 2002; Metcalf et al. 2004).

It seems to be extremely difficult to get an observable lensing signal from the small an relatively diffuse first structures.

7.6.3 Annihilation into gamma-rays

Simple scaling arguments suggest that minihalos have very high relative luminosities in γ-rays. According to Koushiappas, Zentner & Walker (2004) the absolute γ-ray luminosity of a dark matter halo with an NFW density profile (and a tiny constant density core due to annihilation) is proportional to $L \propto \rho_s^2\, r_s^3 \propto M^{0.52}$, where r_s is the scale radius of the NFW profile and $\rho_s = \rho(r_s)$. The relative luminosity that would arrive at a detector from a halo at a distance d is then $L_{\rm rel} \propto Ld^{-2}$. Now we estimate the relative luminosity of the nearest subhalo per decade in mass, assuming that the distance to the nearest substructures scales like their mean separation:

$$\begin{aligned} L_{\rm rel} &\propto \rho_s^2\, r_s^3 d^{-2} \propto M^{0.52}(dn/d\log M^{-1/3})^{-2} \\ &\propto M^{0.52}(M^{1/3})^{-2} \propto M^{-0.15} \quad . \end{aligned} \tag{7.2}$$

According to this estimate the large abundance of the smallest subclumps could compensate their smaller absolute luminosity and make them the brightest subhalos in the annihilation signal. However the $L \propto M^{0.52}$ scaling holds for clump masses above $10^4\mathrm{M}_\odot$, where $c \propto M^{-0.07}$. In the mass range from $10^{-6}\mathrm{M}_\odot$ to $1\mathrm{M}_\odot$ we found no mass dependence of the concentration at z=26, therefore the real luminosity probably depends more strongly on halo mass.

Now we compare the relative luminosity of a minihalo at a distance of one parsec to the signal from the center of Draco:

$$L_{\rm rel,draco} \propto (1.7 \times 10^5 \rho_{\rm crit})^2 (0.3kpc)^3 (50kpc)^{-2} \tag{7.3}$$

$$L_{\rm rel,mini} \propto (7 \times 10^6 \rho_{\rm crit})^2 (0.004pc)^3 (1pc)^{-2} \quad . \tag{7.4}$$

$$L_{\rm rel,mini}/L_{\rm rel,draco} \simeq (41)^2 (1.7 \times 10^{-5})^3 (2 \times 10^{-5})^{-2} \simeq 0.02\ , \tag{7.5}$$

where we used typical minihalo properties at z=26. The same result is obtained by calculating line of sight integrals trough the halo centers averaged over a Gaussian beam of with 0.1 degrees, a typical resolution of todays experiments (Stoehr et. al, 2002). The line of sight integral through the Milky Way center (assuming an NFW profile, neglecting its adiabatic contraction e.g. Prada et al. (2004), a possible supermassive black hole induced spike, enhancement through substructure along the line of sight (Calcaneo-Roldan & Moore 2000; Stoehr et. al 2002)) shows that the galactic center is about three orders of magnitudes brighter than Draco. According to Calcaneo-Roldan & Moore (2000) the smooth background emission from the Milky Way halo (including the enhancement by substructures) is almost as bright as Draco and brighter than a minihalo at a distance of one parsec.

If the $L \propto M^{0.52}$ scaling and the cumulative mass function $N(> m) \propto m^{-1}$ are right down to the minihalo mass range then the closest minihalos could be the brightest substructures in the dark matter annihilation signal. But our simulations suggest that the concentrations are roughly constant from $10^{-6}\mathrm{M}_\odot$ to $1\mathrm{M}_\odot$, which suppresses they relative luminosity of the smallest halos.

If there are subclumps with relative luminosities in the detectable range they would unresolved point sources for the resolution of about 0.1 degrees of present experiments, while the expected signal from the galactic center should also be detectable a few degrees away form the center (Stoehr et. al, 2002). To check if the same is true for a much smaller, but close-by minihalo we compare the angular size of region above a given flux towards the Draco and towards a minihalo. Assuming the same form for the inner density profiles we find that the size on the sky of a minihalo and of Draco are similar for a minihalo at a distance of about 0.1 pc. However adiabatic contraction could steepen the inner profile of Draco and increase the angular size of the detectable signal (Prada et al., 2004).

7.7 Conclusions

We present simulations of the formation of the first and smallest structures that form in the universe according to a SUSY-CDM model and find the following results:

- The density profiles resemble rescaled profiles of galactic halos, with concentrations between 2 and 4 near the time of formation (z=27).
- The abundance of these minihalos lies in a range obtained by extrapolation of the well known mass function on galactic scales with a slope of $\alpha = -1$ down to $10^{-6}\mathrm{M}_\odot$.
- Due to their very high physical density a large number of minihalos could survive as subhalos in the galactic potential. Their expected local number density is about $n \simeq 0.4pc^{-3}$.
- The large number density implies that the closest minihalos could be detected as point sources in the SUSY-CDM annihilation signal.

Acknowledgments

It is a pleasure to thank Philippe Jetzer, Marco Miranda, Andrea Maccio and Gianfranco Bertone for helpful discussions. All computations were performed on the zBox supercomputer at the University of Zurich. J. D. is supported by the Swiss National Science Foundation.

Chapter 8

Final remarks and outlook

Today the nonlinear evolution of the dark matter distribution can be followed very accurately with N-body simulations on supercomputers. The simple interaction law between the simulation particles (Newtonian gravity, going to a softer force at small scales) and the now very well known cosmological initial conditions (mostly thanks to CMB anisotropy measurements) make the dark matter distribution an ideal problem for numerical modelling. There is now a general agreement between the results of different groups (using different codes to generate initial conditions and to evolve them) about the large scale distribution of dark matter halos and also about many of their internal properties: The halo density profiles agree down to about 0.5 percent of the halo size. The subhalo mass function and their distribution in space and velocity agrees also, at least for the bigger subclumps which contain more than 100 particles.

But some uncertainties remain:

- What is the slope of the dark matter density profile at 0.1 percent of the radius? Does the profile continue to rise like in the well resolved regions (cusp) or does it reach a constant density core? We showed that discreteness effects lead to numerical flattening of the profiles and that these effect loose their importance only slowly when the mass resolution is increased. This could explain why the converged scale shrinks slower than $1/\sqrt{N}$ and why it is so difficult to resolve the inner cusp. Only our highest resolution simulation shows a clear inner region with constant logarithmic slope at most output times. This suggest that density profiles probably are cuspy and that over 100 million particles inside the halo are needed to resolve the cusp.

- How big is the fraction of smooth, unclustered dark matter in the field and inside a halo? The mass functions of field and subhalos are steep in the range resolved today ($n(>m) \propto m^{-1}$). This means that each decade in mass contributes a similar fraction to the total bound mass. Does this scaling hold down to the smallest dark matter objects ($m \simeq 10^{-6}\mathrm{M}_\odot$)? For the field we find that the mass function is nearly as steep down to the smallest objects, but it is not clear yet how many of them can survive as substructures in a bigger halo and how much of their mass is really converged into the smooth halo background by tidal stripping and disruption.

- A similar question arises in the inner percent of the halos: In current simulations these regions are completely smooth. Subhalos that pass through this region are disrupted. But maybe small, dense subclumps could survive even there?

One also has to remember that neglecting the baryons is an approximation which breaks down on some scales. The smallest halos are always dark matter dominated everywhere since their mass is much below the Jeans mass of the baryons at all epochs. But the dark matter profiles of galaxies can become steeper as a response to the cooling of gas in the center (adiabatic contraction). This could rise the number of surviving structures, especially in the inner part of galaxy clusters. Maybe the simulated cluster galaxy number density profiles become as steep as the observed ones when the gas dynamics are followed correctly. Gas physics will also decide which halos remain darik and which do form stars and galaxies. Many of the crucial processes are not well understood yet (star formation, energy (and chemical) feedback of stars through radiation and supernovae, radiation from active galactic nuclei). The ionization state of the intergalactic gas seems to be the key issue that decides where and when galaxies can form. It might explain why many dwarf galaxy halos that should exist as subhalos in the dark matter halo of the Milky Way have not captured enough gas to form a visible component. This would resolve the apparent disagreement between the large number of subhalos and the much smaller number of satellite galaxies around the Milky Way.

The natural extension of the N-body method to incorporate also a gas component is SPH (Smoothed Particle Hydrodynamics), where besides gravity for the gas particles also additional interactions with the nearest neighbors are evaluated. Of course it is much more complicated the reach a realistic treatment, since with gas many important processes happen below the resolution scale of the simulation and have to be put in with semi-analytical recipes (e. g. star formation, all sorts of feedback, coexistence of a hot and cold phase, turbulence). And the computational cost is much higher than in pure gravity simulations which makes it difficult to resolve for example a galaxy cluster which contains realistic cluster galaxies. But future gas simulations (with SPH or adaptive grid methods) will be able to make detailed predictions about the distribution of the luminous matter in the universe. Comparisons with observations will then be a real test for the ΛCDM model and for our understanding of galaxy formation.

There are also ways to observe the dark matter distribution which are (almost) independent of the luminous component, these seem to be to most interesting in the near future: Gravitational lensing can measure the mass distribution in clusters and galaxies, and the flux ratios of multiple images are sensitive to substructure. A direct or indirect dark matter detection could be in the reach of the current experiments. Indirect detection signals form various sources would even allow to compare the dark matter densities in different structures in the galactic halo, and maybe even in nearby galaxies.

Bibliography

Abadi, M. G., Moore, B., Bower R. G., 1999, MNRAS, 308, 947

Abazajian K. et al. [SDSS Collaboration], 2003, Astron. J., 126, 2081

Baertschiger T., Joyce M., Sylos Labini F., 2002, ApJ, 581, L63

Balogh, M. L., Navarro, J. F., Morris, S. L., 2000, ApJ, 540, 113

Barnes J. E., 1999, in Barnes J. E., Sanders D. B., eds, Proc. IAU Symp. 186, Galaxy Interactions at Low and High Redshift. Kluwer, Dordrecht, p. 137

Beers T. C. , Tonry J. L., 1986, ApJ, 300, 557

Berlind A. A. et al., 2003, ApJ, 593, 1

Bertin G., 2000, Galactic Dynamics. Cambridge Univ. Press, Cambridge

Bertone G., Hooper D., Silk J., 2004, preprint, arXiv:hep-ph/0404175.

Bertschinger E., 2001, ApJSS, 137, 1

Bode P., Ostriker J. P., 2003, ApJSS, 145, 1

Binney J., 2004, MNRAS, 350, 939

Binney J., Knebe A., 2002, MNRAS, 333, 378

Binney J., Tremaine S., 1987, Galactic Dynamics. Princeton Univ. Press, Princeton

Calcáneo-Roldán C., Moore B., 2000, PhRvD, 62, 123005

Carlberg R. G., Couchman H. M. P., 1989, ApJ, 340, 47

Carlberg, R. G., 1994, ApJ, 433, 468

Carlberg R. G., Yee H. K. C., Ellingson E., 1997, ApJ, 478, 462

Chandrasekhar S., 1942, Principles of Stellar Dynamics. Univ. Chicago Press, Chicago

Chen R. Y., Dong F., Bode P., Ostriker J. P., preprint, arXiv:astro-ph/0403352.

Colin P., Klypin A. A., Kravtsov A. V., 2000, ApJ, 539, 561

Colless M. et al., preprint, arXiv:astro-ph/0306581

Cypriano E. S., Sodré L. J., Kneib J., Campusano L. E., 2004, ApJ in press, arXiv:astro-ph/0310009

Dalal N., Kochanek C. S., 2002, ApJ, 572, 25

Davis M., Efstathiou G., Frenk C. S., White S.D.M., 1985, ApJ, 292, 371

de Blok W. J. G., Bosma A., 2002, A&A, 385, 816

de Blok W. J. G., McGaugh S. S., Bosma A., Rubin V. C., 2001, ApJ, 552, L23

de Blok W. J. G., McGaugh S. S., Rubin V. C., 2001, AJ, 122, 2396

De Lucia G., Kauffmann G., Springel V., White S. D. M., Lanzoni B., Stoehr F., Tormen G., Yoshida N., 2004, MNRAS, 348, 333

Desai V., Dalcanton J. J., Mayer L., Reed D., Quinn T., Governato F., 2004, MNRAS.351, 265

Diemand J., Moore B., Stadel J., Kazantzidis S., 2004a, MNRAS, 348, 977

Diemand J., Moore B., Stadel J., 2004b, MNRAS, 352, 535, astro-ph/0402160

Diemand J., Moore B., Stadel J., 2004c, MNRAS, in press, astro-ph/0402267

Dubinski J., Carlberg R. G., 1991, ApJ, 378, 496

Eke V. R., Cole S., Frenk C. S., 1996, MNRAS, 282, 263

Eidelman S., et al. [Particle Data Group], 2004, Phys. Lett. B592, 1

Feldmeier J., Ciardullo R., Jacoby G., Durrell P., preprint, arXiv:astro-ph/0407274.

Flix J., Martinez M., Prada F., 2004, preprint, astro-ph/0401511.

Freedman W. L. et al.,2001 ,ApJ, 553, 47

Frenk, C. S., A. E. Evrard, S. D. M. White, and F. J. Summers 1996, ApJ, 472, 460

Fukushige T., Makino J., 1997, ApJ, 477, L9

Fukushige T., Makino J., 2001, ApJ, 557, 533

Fukushige T., Kawai A. and Makino J., 2004, ApJ,. 606, 625

Gao L., White S.D.M., Jenkins A., Stoehr F., Springel V., 2004a, preprint, astro-ph/0404589.

Gao L., De Lucia G., White S.D.M., Jenkins A., 2004b, MNRAS in press, astro-ph/0405010.

Gentile G., Salucci P., Klein U., Vergani D., Kalberla P.,2004, MNRAS in press, arXiv:astro-ph/0403154.

Gerhard O. E., 1993, MNRAS, 265, 213

Ghigna S., Moore B., Governato F., Lake G., Quinn T., Stadel J.,1998, MNRAS, 300, 146

Ghigna S., Moore B., Governato F., Lake G., Quinn T., Stadel J., 2000, ApJ, 544, 616

Gill S.P.D., Knebe A., Gibson B.K.,2004, preprint, astro-ph/0404427.

Green A,.M., Hofmann S., Schwarz D. J., 2004, preprint, arXiv:astro-ph/0309621.

Hawkins E. et al.,2003, MNRAS, 346, 78

Hayashi E., Navarro J. F., Taylor J. E., Stadel J., Quinn T., 2003a, ApJ, 584, 541

Hayashi E., Navarro J. F. , Power C., Jenkins A., Frenk C.S., White S. D. M., Springel V., Stadel J., Quinn T., 2003b, preprint, astro-ph/0310576.

Hernquist L., 1990, ApJ, 356, 359

Huang S., Dubinski J., Carlberg R. G., 1993, ApJ, 404, 73

Hubble, E., Humason, M. L., 1931, ApJ, 74, 43

Jenkins A., Frenk C. S., White S. D. M., Colberg J. M., Cole S., Evrard A. E., Couchman H. M. P., Yoshida N., 2001, MNRAS, 321, 372

Jing Y., Suto Y., 2000, ApJ, 529, L69

Jing Y., Suto Y., 2002, ApJ, 574, 538

Kazantzidis S., Magorrian J., Moore B., 2004a, ApJ, 601, 37

Kazantzidis S., Mayer L., Mastropietro C., Diemand J., Stadel J., Moore B., 2004b, ApJ, 608, 663

Koushiappas S. M., Zentner A. R., Walker T. P., 2004, Phys. Rev. D, 69, 043501

Klypin A., Gottlöber S., Kravtsov A. V., Khokhlov A. M., 1999, ApJ, 516, 530

Klypin A., Kravtsov A. V., Valenzuela O., Prada F., 1999, ApJ, 522, 82

Klypin A., Kravtsov A. V., Bullock J. S., Primack J. R., 2001, ApJ, 554, 903

Knebe A., Green A., Binney J., 2001, MNRAS, 325, 845

Knebe, A., Kravtsov A. V., Gottlöber S., and Klypin A.A., 2000, MNRAS, 317, 630

Kolb, E.W., Turner, M.S., 1990. The Early Universe, Addison-Wesley, Redwood City

Kravtsov A. V. , Gnedin O. Y., Klypin A. A., 2004, ApJ, 609, 482

Kravtsov A. V., Klypin A. A., Khokhlov A. M., 1997, ApJ, 111, 73

Lewis I.J. et al., 2002, MNRAS, 333, 279

Liddle, A.R., Lyth, D.H., 2000. Cosmological Inflation and Large-Scale Structure, Cambridge University Press

Lokas E. L., Mamon G. A., 2003, MNRAS, 343, 401

Magliocchetti M., Porciani C., 2003, MNRAS, 346, 186

Mamon G. A., Sanchis T., Salvador-Solé E., Solanes J. M., 2004, A&A, 414, 445.

Mao S., Schneider P., 1998, MNRAS, 295, 587

McGaugh S. S., Rubin V. C., de Blok W. J. G., 2001, AJ, 122, 2381

Merrifield M. R. , Kent S. M., 1989, AJ, 98, 351

Metcalf R. B., Moustakas L. A., Bunker A. J., Parry I., ApJ, 607, 43

Metcalf R. B., Madau P., 2001, ApJ, 563, 9

Moore B., Diemand J., Stadel J., 2004 in IAU Conf. Proc. 195, 'Outskirts of galaxy clusters', in press, arXiv:astro-ph/0406615.

Moore B. 2001, In Martel H., Wheeler J., eds, AIP Conf. Proc. 586, The Dark Matter Crisis, Am. Inst. Phys., New York, 73

Moore B., Ghigna S., Governato F., Lake G., Quinn T., Stadel J., Tozzi P., 1999a, ApJ, 524, L19

Moore B., Quinn T., Governato F., Stadel J., Lake G., 1999b, MNRAS, 310, 1147

Moore B., Governato F., Quinn T., Stadel J., Lake G., 1998, ApJ, 499, L5

Moore B., Katz N., Lake G., 1996, ApJ, 457, 455

Moore B., 1994, V.370, Nat, 370, 629

Navarro J. F., Hayashi E., Power C., Jenkins A., Frenk C. S., White S. M. D., Springel V., Stadel J., Quinn T. R., 2004, MNRAS, 349, 1039

Navarro J. F., Frenk C. S., White S. D. M., 1996, ApJ, 462, 563

Okamoto T., Habe A., 1999, ApJ, 516, 591

Peacock, J. A., 1999, Cosmological Physics. Cambridge Univ. Press, Cambridge

Peacock J. A., 2003, Phil. Trans. Roy. Soc. Lond. A, 361, 2479

Peebles P. J. E., 1970, AJ, 75, 13

Perlmutter S. et al. [Supernova Cosmology Project Collaboration], 1999, ApJ, 517, 565

Power C., Navarro J. F., Jennkins A., Frenk C. S., White S. D. M., 2003, MNRAS, 338, 14

Prada F.,Klypin A., Flix J., Martinez M., Simonneau E., 2004, preprint, arXiv:astro-ph/0401512.

Quinlan G. D., 1996, New Astronomy, vol. 1, no. 3, 255

Reed D., Gardner J., Quinn T., Stadel J., Fardal M., Lake G., Governato F., 2003a, MNRAS, 346, 565

Reed D., Governato F., Verde L., Gardner J., Quinn T., Stadel J., Merritt D., Lake G., 2003b, preprint, arXiv:astro-ph/0312544.

Riess A. G. et al.[Supernova Search Team Collaboration], 1998, Astron. J., 116, 1009

Riess A. G. et al. [Supernova Search Team Collaboration], 2001, ApJ, 560, 49

Romanowsky A. J., Douglas N. G., Arnaboldi M., Kuijken K., Merrifield M. R., Napolitano N. R., Capaccioli M., Freeman K. C., 2003, Sci, 301, 1696

Sanchis T., Lokas E. L., Mamon G. A., 2004, MNRAS, 347, 1198

Sand D. J., Treu T., Smith G. P., Ellis R. S., 2004, ApJ, 604, 88

Schmidt R., Wambsganss J., 1998, A&A, 335, 379S

Spitzer L., 1987, Dynamical Evolution of Globular Clusters. Princeton Series in Astrophysics, Princeton

Spergel D. N. et al., 2003, ApJSS, 148, 175

Springel V., Yoshida N., White S. D. M., 2001a, New Astronomy, 6, 79

Springel V., White S. D. M., Tormen G., Kauffmann G., 2001b, MNRAS, 328, 726

Stadel J., 2001, PhD thesis, U. Washington

Stoehr F., White S. D., Tormen G., Springel V., 2002, MNRAS, 335, L84

Stoehr F., White S. D., Springel V., Tormen G., Yoshida N., 2003, MNRAS, 345, 1313

Stoehr F., 2004, preprint, arXiv:astro-ph/0403077.

Summers, F. J., M. Davis, A. E. Evrard 1995, ApJ, 454, 1

Swaters R. A., Madore B. F., van den Bosch F. C., Balcells M., 2003, ApJ, 583, 732

Syer D., White S. D. M., 1998, MNRAS, 293, 337

Taffoni G., Mayer L., Colpi M., Governato F., 2003, MNRAS, 341, 434

Tasitsiomi A., Kravtsov A. V., Gottlober S., Klypin A. A., 2004, ApJ, 607, 125

Taylor J. E., Silk J., Babul A., 2003, IAUS, 220, astro-ph/0312086

Theis C., 1998, A&A, 330, 1180

Tormen G., Bouchet F. R., White S. D. M., 1997, MNRAS, 286, 865

van den Bosch F. C., Yang X. H., Mo H. J., Norberg P., preprint, arXiv:astro-ph/0406246

van der Marel R. P., Magorrian J., Carlberg R. G., Yee H. K. C., Ellingson E., 2000, AJ, 119, 2038 van Kampen E.,1995, MNRAS, 273, 295

Wambsganss J., Bode P., Ostriker J. P., 2004, ApJ, 606, L93

Warren M. S., Quinn P. J., Salmon J. K., Zurek W. H., 1992, ApJ, 399, 405

Weekes T. C. et al., 2002, Astropart. Phys., 17, 221

Weinberg M. D., 1998, MNRAS, 297, 101

White, S. D. M., 1976, MNRAS, 177, 717

White, S. D. M., Rees M. J., 1978, MNRAS, 183, 341

White, S. D. M., M. Davis, G. Efstathiou, and C. S. Frenk, 1987, Nature, 330, 45

Yang X., Mo H. J., van den Bosch F. C., 2003, MNRAS, 339, 1057

Yoshida N., Sokasian A., Hernquist L., & Springel V., 2003a, ApJ, 591, L1

Yoshida N., Sokasian A., Hernquist L., Springel V., 2003b, ApJ, 598, 73

Zentner A. R. , Bullock J. S., 2003, ApJ, 598, 49

Zhao, H. 1996, MNRAS, 278, 488

Zwicky F., 1937, ApJ, 86, 217

Acknowledgments

Many people have supported this work. First of all I want to thank Ben Moore for triggering my interest in this fascinating branch of cosmology, for giving me the opportunity to write this thesis, for many ideas, continuous guidance, encouragement and support, and for building up very active and fun research group here in Zurich in the last three years. Joachim Stadel contributed many great ideas to this work. He also wrote most of the programs we used and was always able to help my when I was struggling with my own programming attempts. I also enjoyed very much working together and exchanging ideas with Chiara Mastropietro, Steen Hansen, Philippe Jetzer, Stelios Kazantzidis, Tobias Kaufmann, Andrea Maccio, Lucio Mayer Marco Miranda, Rocco Piffaretti and Marcel Zemp and with Frank van den Bosch, Victor Debattista, Peder Norberg and Cristiano Porciani from the ETH Astronomy group. Other people have also contributed to some of the projects presented in this work, their input is acknowledged at the end of the corresponding chapters.

I also would like to thank all the people at the Institute of Theoretical Physics and our colleagues at ETH at the Institute of Astronomy for many nice and valuable discussions, coffee breaks, pizza lunches, seminars, astro-ph sessions, football matches and skiing days!

This thesis used a great deal of computing power that our zBox supercomputer offers and it is hard to imagine doing this work without having almost exclusive and unlimited access to such a powerful machine. Therefore I am grateful to everybody who helped to make it possible to have a modern supercomputer devoted to cosmology here at the Institute, especially to Joachim and Ben for designing, building and getting the zBox running within a few months. We also had the possibility to use a comparable, new IBM supercomputer at the Swiss National Supercomputing Centre, which was especially useful at the beginning of this thesis before the installation of the zBox.

I thank the University of Zurich and the Swiss National Fund for financial support, and I would like to thank especially Prof. Diethard Klatte and the Institute for Operations Research where I worked during the first two years of my thesis.

Finally: Zintia, Ursula and Alfons, Nani, Chistine, Susanne and Simone, and all my friends!

CURRICULUM VITAE

Personal data

Name : Diemand
First name : Jürg
Date of birth : 28/7/1976
Place of origin: Uster ZH
Nationality : Swiss

Education

10/2001-09/2004: PhD in Physics, Dr. sc. nat., University of Zurich, Switzerland
PhD thesis: Cosmological N-Body Simulations
of cold dark matter halos
Thesis supervisor: Prof. Ben Moore

10/1996-06/2001: M.S. in Physics, Dipl. Phys., Unversity of Zurich, Switzerland
Master subjects: Theoretical physics, cosmology, general relativity
Minor subjects: Mathematics, computer science
ERASMUS exchange: Universidad de Cantabria,
Santander, Spain, 10/1999-04/2000
Diploma thesis: Dynamical instabilities of brane world models
Thesis supervisor: Prof. Daniel Wyler

09/1989-01/1996: Matura type B, Kantonsschule ZO, Wetzikon ZH, Switzerland

Teaching experience

10/2003-09/2004: Teaching assistant for theoretical physics at the Institute for Theoretical Physics at the University of Zurich for physics majors: Thermodynamics, General Relativity.

10/2001-09/2003: Teaching assistant for analysis and linear algebra at the Institute for Operations Research at the University of Zurich for undergraduate students: coordination and conception of exercises and examinations.

Languages

German: Native language
Spanish: fluent
English: fluent
French: good

RESEARCH STATUS

Publications:

1.) J. Diemand, B. Moore, J. Stadel, S. Katzantsidis
Two body relaxation in CDM simulations
MNRAS 348 (2004) 977 (*astro-ph/0304549*)

2.) B. Moore S. Kazantzidis, J. Diemand, J. Stadel
The origin and tidal evolution of cuspy triaxial haloes
MNRAS (2004) in press (*astro-ph/0310660*)

3.) S. Kazantzidis, L. Mayer, C. Mastropietro, J. Diemand, J. Stadel, B. Moore
Density Profiles of Cold Dark Matter Substructure: Implications for the Missing Satellites Problem
Astrophys.J. 608 (2004) 663 (*astro-ph/03121949*)

4.) J. Diemand, B. Moore, J. Stadel
Velocity and spatial biases in CDM subhalo distributions
MNRAS 352 (2004) 535 (*astro-ph/0402160*)

5.) J. Diemand, B. Moore, J. Stadel
Convergence and scatter of cluster density profiles
MNRAS (2004) in press (*astro-ph/0402267*)

Conference proceedings:

1.) J. Diemand
Resolving the Inner Structure of CDM Clusters
in: *Astrophysics Conference : 'Star and Structure Formation - From First Light to the Milky Way.', ETH Zurich, August 2003.*
http://www.exp-astro.phys.ethz.ch/ETH_Astro_2003/Talks/diemand_t.pdf

2.) J. Diemand, B. Moore, J. Stadel
Density Profiles and Substructure of CDM Halos
in: *XXXIXth Moriond Cosmology Workshop: 'Exploring the Universe - Contents and Structures of the Universe.', La Thuile, Italy, March 2004.*
http://moriond.in2p3.fr/J04/trans/diemand.pdf
http://moriond.in2p3.fr/J04/proceedings/diemand.ps.gz

3.) B. Moore, J. Diemand, J. Stadel
On the age-radius relation and orbital history of cluster galaxies
in: *IAU Colloquium 195: 'Outskirts of galaxy clusters: intense life in the suburbs', Torino, Italy, March 12-16, 2004.*
http://www.iauc195.to.infn.it

Attended schools:

1.) Graduate school in contemporary relativity and gravitational physics, V:
'Joint Evolution of Black Holes and Galaxies', Como, Italy, May 5-10, 2003

Diploma thesis guidance:

1.) Peter Trueb, ETH Zurich, 2004
2.) Daniel Mayr, University of Zurich, 2004